NASA/CR 97- 206042

/11 [illegible] /C
OCIT

FINAL REPORT

FOR

NASA NAG 3-1474

Grant Title: Electromagnetic Scattering from Realistic Targets

Institution:
Electromagnetics Laboratory
Department of Electrical and Computer Engineering
University of Illinois at Urbana-Champaign
Urbana, IL 61801-2991

Period Covered: April 1995 — May 1997

Co-Principal Investigators:

S. W. Lee, Professor of ECE
Tel: 217-333-1200 Fax: 217-333-5962

J. Jin, Associate Professor of ECE
Tel: 217-244-0756 Fax: 217-333-5962

1. Summary

In April 1995, the University of Illinois received a NASA Grant NAG3-1474 entitled "Electromagnetic Scattering from Realistic Targets" for a one-year period and the grant was extended for another year with no cost. The co-principal investigators are Professors Shung-Wu Lee and Jianming Jin, and the NASA technical monitor is Dr. Afroz Zaman. This project has been completed. Results are reported in the following technical reports:

1. J. M. Jin, J. A. Berrie, R. Kipp, and S. W. Lee, "Calculation of radiation patterns of microstrip antennas on cylindrical bodies of arbitrary cross section," May 1996.

2. A. D. Greenwood, S. S. Ni, J. M. Jin, and S. W. Lee, "Hybrid FEM/SBR method to compute the radiation pattern from a microstrip patch antenna in a complex geometry," October 1996.

3. G. Fan and J. M. Jin, "Scattering from a cylindrically conformal slotted-waveguide array antenna," December 1996.

4. G. Fan and J. M. Jin, "Scattering from a large planar slotted waveguide array antenna," August 1997.

5. E. Branch, "A numerical comparison of measured SAR images with XPATCH computed SAR images," UIUC EM Lab. Scientific Report No. 95-2, September 1995.

6. S. Ni, J. M. Jin, and S. W. Lee, "Hybridization of the finite-element method and the shooting-and-bouncing-ray method for scattering and radiation from large and complex targets," UIUC EM Lab. Scientific Report No. 95-3, October 1995.

The first four reports are included here as appendices. The last two reports have been submitted to NASA before and, hence, are not included here.

The general goal of the project is to develop computational tools for calculating radar signature of realistic targets. During the period of this grant, we developed a hybrid technique that combines the shooting-and-bouncing-ray (SBR) method and the finite-element method (FEM) for the radiation characterization of microstrip patch antennas in a complex geometry. The technical details are given in Appendices 1 and 2. In addition, we developed a hybridization procedure to combine the moment method (MoM) solution and the SBR method to treat the scattering of waveguide slot arrays on an aircraft. The technical details are described in Appendices 3 and 4.

2. Publications Resulting from This Research

Journal articles (published or accepted):

1. J. M. Jin, J. A. Berrie, R. Kipp, and S. W. Lee, "Calculation of radiation patterns of microstrip antennas on cylindrical bodies of arbitrary cross section," *IEEE Trans. Antennas Propagat.,* vol. AP-45, no. 1, pp. 126-132, Jan. 1997.

2. A. D. Greenwood, S. S. Ni, J. M. Jin, and S. W. Lee, "Hybrid FEM/SBR method to compute the radiation pattern from a microstrip patch antenna in a complex geometry," *Microwave Opt. Tech. Lett.*, vol. 13, no. 2, pp. 84-87, Oct. 1996.

3. G. Fan and J. M. Jin, "Scattering from a cylindrically conformal slotted-waveguide array antenna," *IEEE Trans. Antennas Propagat.,* vol. AP-45, no. 7, pp. 1150-1159, July 1997.

4. A. D. Greenwood and J. M. Jin, "Hybrid MoM/SBR method to compute scattering from a slot array in a complex geometry," *Applied Computational Electromagnetics Society Journal*, accepted for publication, 1997.

5. G. Fan and J. M. Jin, "Scattering from a large planar slotted waveguide array antenna," *Electromagnetics*, accepted for publication, 1997.

Conference papers:

1. G. Fan and J. M. Jin, "Scattering from a cylindrically conformal slotted-waveguide array antenna," The 1996 IEEE Antennas and Propagation Society International Symposium, Baltimore, MD, 1996, pp. 1394-1397.

2. A. D. Greenwood, S. Ni, and J. M. Jin, "Computation of the radiation pattern of a microstrip patch antenna in a complex geometry," The 1996 IEEE Antennas and Propagation Society International Symposium, Baltimore, MD, 1996, pp. 256-259.

3. A. D. Greenwood and J. M. Jin, "Hybrid MoM/SBR method to compute scattering from a slot array antenna in a complex geometry," The 13th Annual Review of Progress in Applied Computational Electromag-netics, Monterey, CA, 1997.

APPENDIX 1

Calculation of Radiation Patterns of Microstrip Antennas on Cylindrical Bodies of Arbitrary Cross Section

Jian-Ming Jin, Jeffery A. Berrie, Robert Kipp and Shung-Wu Lee

ABSTRACT

A simplified approach based on reciprocity is presented to calculate the radiation patterns of microstrip patch antennas or arrays on a cylindrical body having an arbitrary cross section. In this approach, the microstrip patch antennas are characterized using the finite element method, and their radiation patterns are then calculated using a two-dimensional method of moments in conjunction with the reciprocity theorem. The validity of the calculation is demonstrated by comparison with measured data for a microstrip patch antenna on a circular cylinder attached to a plate. Other numerical examples are also presented to show the capability of the method, as well as various effects of the host cylinder on radiation patterns.

This work was supported by the Office of Naval Research under the grant N00014-95-1-0848, NASA under the grant NAG3-1474, and the Air Force Rome Laboratory under contract F-30602-93-C-0036.

J. M. Jin and S. W. Lee are with the Electromagnetics Laboratory, Department of Electrical and Computer Engineering, University of Illinois at Urbana-Champaign, Urbana, IL 61801-2991.

J. A. Berrie is with Mission Research Corporation, 3975 Research Boulevard, Dayton, OH 45430.

R. Kipp is with DEMACO, 100 Trade Center Drive, Champaign, IL 61820.

I. Introduction

Microstrip patch antennas [1]-[3] are attractive for aircraft and spacecraft applications because they are conformal to the surface of the host object. However, their analysis is often performed by assuming that the antennas are placed on an infinite ground plane with an infinite dielectric substrate [4]-[6] or on a finite substrate housed in a cavity recessed in the ground plane [7]. Although such an analysis can be extended to the antennas on a coated circular cylinder [8]-[10] or in a cavity recessed in a conducting circular cylinder [11], it cannot be applied to those on a cylinder with an arbitrary cross section because the Green's function for such a structure is not available. While the shape of a host cylinder has little effect on the input impedance and current distribution of a microstrip antenna since the latter is a highly resonant structure, it can alter the radiation patterns substantially. The objective of this paper is to develop a simple method to calculate the radiation patterns of microstrip patch antennas on substrates residing in cavities recessed in cylindrical bodies of arbitrary cross section possibly with dielectric coatings.

In the proposed method, the equivalence principle is first employed to divide the problem into two equivalent problems. The first problem is to characterize microstrip patch antennas housed in a cavity whose aperture is closed with a perfect conductor, which is accomplished using the finite element method [7]. The second problem is to compute the field radiated by the equivalent magnetic current over the cavity's aperture in the presence of the host cylinder, and to accomplish this task, an approach based on the reciprocity theorem is developed in conjunction with a two-dimensional method of moments for scattering computation. The validity of the proposed method is demonstrated by comparison with measured data for a microstrip patch antenna on a circular cylinder attached to a plate and for a waveguide-fed trihedral. Other numerical examples are also presented to show the capability of the method and the effects of patch rotation, material coating, and finiteness of a ground plane on the radiation patterns.

II. Formulation

Consider the problem illustrated in Fig. 1 where several microstrip patch antennas are placed on a conducting cylinder of arbitrary cross section. These microstrip patch antennas are housed in one or several shallow cavities and the conducting cylinder may be coated with dielectrics. Since a microstrip patch antenna is a highly resonant structure, its current distribution and input impedance at resonance are mainly determined by internal structures such as the shape of the patch, the thickness and dielectric constant of the substrate and superstrate. Provided that a patch antenna is placed on a locally flat surface or surface with a small curvature, the shape of the host cylinder (external structure) has little effect on its current distribution and input impedance, as demonstrated in [11]. Therefore, the patch antenna can be characterized approximately by assuming that it is placed on an infinitely large ground plane. Applying the equivalence principle, we can close the aperture of the cavity housing the patch antennas with a sheet of perfect conductor and introduce a magnetic current density over the aperture defined as

$$\vec{M} = \vec{E} \times \hat{n} \tag{1}$$

where $\hat{n}$ denotes the outward unit vector normal to the aperture. As shown in [7], this magnetic current can be determined using the finite element method with vector elements by seeking the stationary point of the functional

$$\begin{aligned} F(\vec{E}) = & \frac{1}{2}\iiint_V \left[\frac{1}{\mu_r}(\nabla \times \vec{E}) \cdot (\nabla \times \vec{E}) - k_0^2 \varepsilon_r \vec{E} \cdot \vec{E} \right] dV \\ & + \iiint_V \left[jk_0 Z_0 \vec{J}^{\mathrm{int}} \cdot \vec{E} - \frac{1}{\mu_r} \vec{M}^{\mathrm{int}} \cdot (\nabla \times \vec{E}) \right] dV \\ & - k_0^2 \iint_S \vec{M}(\vec{r}) \cdot \left[\iint_S \bar{G}_0(\vec{r}, \vec{r}\,') \cdot \vec{M}(\vec{r}\,') dS' \right] dS \end{aligned} \tag{2}$$

where V denotes the volume of the cavity and S denotes the aperture of the cavity. Also, $\bar{G}_0(\vec{r}, \vec{r}\,')$ denotes the free-space dyadic Green's function, and $\vec{J}^{\mathrm{int}}$ and $\vec{M}^{\mathrm{int}}$ represent the internal sources or antenna excitation. The procedure of the finite element solution and modeling of a current probe and impedance load are described in [7] and [12], and the modeling of waveguide feeds is described in [13].

Once the equivalent magnetic current $\vec{M}$ over the aperture of the cavity is calculated, the radiation patterns can be obtained by computing the field radiated by $\vec{M}$ in the presence of the conducting cylinder with the cavity filled with perfect conductor. Since the cross section of the cylinder is arbitrary and the cylinder may be coated with dielectrics, no pertinent Green's function can be derived and the radiated field cannot be expressed by an integral formulation. To alleviate this difficulty, we propose to employ the reciprocity theorem to calculate the radiated field. According to the reciprocity theorem [14], we have

$$\iiint \vec{E}^a \cdot \vec{J}^b dV = -\iiint \vec{H}^b \cdot \vec{M}^a dV \tag{3}$$

where $\vec{E}^a$ is the field produced by $\vec{M}^a$ and, likewise, $\vec{H}^b$ is the field produced by $\vec{J}^b$. Letting $\vec{M}^a$ be the equivalent magnetic current $\vec{M}$ over the aperture of the cavity and $\vec{J}^b$ be the electric dipole of moment Il located at (r,θ,ϕ) and oriented in the $\hat{u}$-direction, the radiated field is then given by

$$\vec{E}(r,\theta,\phi) \cdot \hat{u} = -\frac{1}{Il} \iint_S \vec{H}^b \cdot \vec{M} \, dS \tag{4}$$

Often, the radiation patterns in the plane perpendicular to the cylinder (that is, the plane of $\theta = \pi/2$) are of particular interest. In this case, we obtain

$$E_z(r,\phi) = \frac{jk_0 Z_0 e^{-jk_0 r}}{4\pi r} \iint_S H_\tau^b M_\tau \, dS \tag{5}$$

$$E_\phi(r,\phi) = -\frac{jk_0 e^{-jk_0 r}}{4\pi r} \iint_S H_z^b M_z \, dS \tag{6}$$

where H_τ^b (or H_z^b) is the magnetic field induced on the surface of the cylinder (again, with the cavity filled with a perfect conductor) by an incident plane wave whose electric (or magnetic) field is in the $\hat{z}$-direction and has a unit amplitude, and M_τ (or M_z) is the component of $\vec{M}$ in the direction perpendicular (or parallel) to the cylinder.

It is then clear that to calculate the radiated field, we have to find H_τ^b and/or H_z^b first. This can be accomplished simply by solving the problem of plane wave scattering by the cylinder using the method of moments. There are several different formulations available for this problem. The most efficient one is to employ the volume-surface integral equation [15] given by

$$k_0^2 \iint_\Omega \left[\varepsilon_r(\vec{r}\,') - \frac{1}{\mu_r(\vec{r}\,')} \right] E_z(\vec{r}\,') G_0(\vec{r},\vec{r}\,') dS' + \iint_\Omega E_z(\vec{r}\,') \nabla' \left[\frac{1}{\mu_r(\vec{r}\,')} \right] \cdot \nabla' G_0(\vec{r},\vec{r}\,') dS'$$
$$+ \int_{\Gamma_d} \left[\frac{1}{\mu_r(\vec{r}\,'_+)} - \frac{1}{\mu_r(\vec{r}\,'_-)} \right] E_z(\vec{r}\,') \frac{\partial G_0(\vec{r},\vec{r}\,')}{\partial n'_d} dl' - jk_0 Z_0 \int_{\Gamma_c} G_0(\vec{r},\vec{r}\,') H_\tau(\vec{r}\,') dl' \tag{7}$$
$$+ E_z^{\text{inc}}(\vec{r}) = \begin{cases} [1/\mu_r(\vec{r})] E_z(\vec{r}) & \text{for } \vec{r} \text{ in dielectric} \\ 0 & \text{for } \vec{r} \text{ in conductor} \\ E_z(\vec{r}) & \text{for } \vec{r} \text{ elsewhere} \end{cases}$$

for E_z-polarization, and

$$k_0^2 \iint_\Omega \left[\mu_r(\vec{r}\,') - \frac{1}{\varepsilon_r(\vec{r}\,')} \right] H_z(\vec{r}\,') G_0(\vec{r},\vec{r}\,') dS' + \iint_\Omega H_z(\vec{r}\,') \nabla' \left[\frac{1}{\varepsilon_r(\vec{r}\,')} \right] \cdot \nabla' G_0(\vec{r},\vec{r}\,') dS'$$
$$+ \int_{\Gamma_d} \left[\frac{1}{\varepsilon_r(\vec{r}\,'_+)} - \frac{1}{\varepsilon_r(\vec{r}\,'_-)} \right] H_z(\vec{r}\,') \frac{\partial G_0(\vec{r},\vec{r}\,')}{\partial n'_d} dl' + \int_{\Gamma_c} \frac{1}{\varepsilon_r(\vec{r}\,')} H_z(\vec{r}\,') \frac{\partial G_0(\vec{r},\vec{r}\,')}{\partial n'_c} dl' \tag{8}$$
$$+ H_z^{\text{inc}}(\vec{r}) = \begin{cases} [1/\varepsilon_r(\vec{r})] H_z(\vec{r}) & \text{for } \vec{r} \text{ in dielectric} \\ 0 & \text{for } \vec{r} \text{ in conductor} \\ H_z(\vec{r}) & \text{for } \vec{r} \text{ elsewhere} \end{cases}$$

for H_z-polarization, where Ω denotes the cross section of the dielectric coating, Γ_d denotes the interface between two different dielectric materials, and Γ_c denotes the conducting surface. Also, $\hat{n}_d$ denotes the unit vector normal to Γ_d and pointing from the "$-$" side to the "$+$" side, and G_0 represents the well-known two-dimensional free-space Green's function. For cylinders without coatings, (7) and (8) reduce to the well-known equations

$$E_z^{\text{inc}}(\vec{r}) - jk_0 Z_0 \int_{\Gamma_c} G_0(\vec{r},\vec{r}\,') H_\tau^b(\vec{r}\,') dl' = \begin{cases} 0 & \text{for } \vec{r} \text{ in conductor} \\ E_z(\vec{r}) & \text{for } \vec{r} \text{ everywhere else} \end{cases} \tag{9}$$

for E_z-polarization, and

$$H_z^{\text{inc}}(\vec{r}) + \int_{\Gamma_c} H_z^b(\vec{r}\,') \frac{\partial G_0(\vec{r},\vec{r}\,')}{\partial n'_c} dl' = \begin{cases} 0 & \text{for } \vec{r} \text{ in conductor} \\ H_z(\vec{r}) & \text{for } \vec{r} \text{ everywhere else} \end{cases} \tag{10}$$

for H_z-polarization. The detailed procedure to solve (7) and (8) using the method of moments is described in [16].

To summarize the proposed method, we first compute the equivalent magnetic current over the cavity's aperture by applying the finite element method to (2). Then, we compute the surface magnetic field induced on the region of the cavity's aperture by applying the method of moments to (7) and (8), or (9) and (10) when there is no coating. Finally, we calculate the radiated field using (5) and (6).

III. Numerical Results

In this section we present some numerical results to demonstrate the validity and capability of the formulation described above. Without loss of generality, the same microstrip patch antenna, depicted in Fig. 2, is used in all examples to follow. This antenna consists of a rectangular conducting patch fed with a probe and housed in a larger dielectric filled rectangular cavity. The first resonance mode at $f = 3.3$ GHz radiates a field whose *E*-plane is perpendicular to the shorter side of the patch and whose *H*-plane is perpendicular to the longer side of the patch.

The first set of results is computed for the microstrip patch antenna on a finite circular cylinder sitting on a conducting plate, illustrated in Fig. 3. The radiation patterns are calculated for two different positions of the antenna whose longer side is parallel to the axis of the cylinder. These patterns are shown in Fig. 4 and compared with measured data provided by Mission Research Corporation, Dayton, OH. As can be seen, the agreement is surprisingly good within the first 30-dB range, demonstrating the validity of the method. The disagreement in the deep shadow region is due to the field diffracted by the sides of the plate perpendicular to the cylinder and also by the ends of the cylinder, which are ignored in our simplified approximate calculation. The corresponding results when the antenna is rotated 90 degrees are shown in Fig. 5. Note that in this case, the predicted sidelobes are significantly higher that those in Fig. 4 because of stronger surface waves propagating around the cylinder.

The proposed method can, of course, handle multiple patch antennas or arrays, such as the one sketched in Fig. 6. The patches and dielectric substrate have the same parameters as the one in Fig. 2. The edge-to-edge distance between two adjacent patches is 1.5 cm and the array is centered at $\phi = 225°$. Figure 7 shows its radiation patterns with and without the plate. The cavity size for the case of Fig. 7(a) is 12 cm in the ϕ-direction and 6 cm in the z-direction, and for the case of Fig. 7(b) is 15 cm in the ϕ-direction and 5 cm in the z-direction. The asymmetric pattern in Fig. 7(b) for the case without the plate is due to the asymmetric placement of the feed.

To demonstrate the capability of the method as well as to show the effect of dielectric coating, we consider a single patch antenna on a circular cylinder having a diameter of 30.48 cm. The antenna is the same as depicted in Fig. 2 and the cylinder is coated with a layer of material having a thickness of 0.546 cm, relative permittivity $\varepsilon_r = 2.2$ and relative permeability $\mu_r = 1.2$ for the lossless case, and $\varepsilon_r = 2.2 - j1.0$ and $\mu_r = 1.2 - j0.5$ for the lossy case. The results are presented in Fig. 8 for the cylinder without coating, with a lossless coating, and with a lossy coating. As can be seen, when the longer side of the patch is parallel to the axis of the cylinder, it does not excite a surface wave propagating around the cylinder. Therefore, the coating does not have a significant effect on the radiation pattern because it is not thick enough to support a surface wave. However, when the shorter side of the patch is parallel to the axis of the cylinder, it excites a surface wave around the cylinder, which is further enhanced by the presence of a lossless coating, raising the level of radiation in the shadow region. When the coating is lossy, the surface wave is attenuated, resulting in a lower level of radiation in the shadow region.

To show the effect of a finite ground plane, we consider the microstrip patch antenna of Fig. 2 placed at the center of a flat conducting plate whose width is w and thickness is 0.5 cm. The radiation pattern in the plane perpendicular to the plate is shown in Fig. 9(a) when the longer side of the patch is parallel to the axis of the plate and in Fig. 9(b) when the shorter side of the patch is parallel to the axis of the plate. The proposed technique provides a simple way to study the finite ground plane effect on microstrip antenna radiation patterns [17].

Finally, we consider a waveguide-fed trihedral, depicted in Fig. 10, to show the applicability of the proposed method to any cavity-backed conformal antennas. The waveguide is 0.9 inch wide and 0.4 inch thick and is at the center of one of the planes. The radiation patterns at $f = 9.0$ GHz in both the E- and H-planes are given in Fig. 11 along with the measured data. Good agreement is observed over a wide range of angles. The disagreement in the shadow region and in the region close to 90° in Fig. 11(a) is mainly due to the third plane, which is ignored in our simplified approximate calculation. Since the waveguide radiator is not a highly resonant structure, we note that the external structures close to the waveguide can have nonnegligible effect on the field distribution at the waveguide opening. As a result, the proposed method can be less accurate than in the case of highly resonant microstrip patch antennas.

IV. Conclusion

In this paper, we described a method to calculate the radiation patterns of cavity-backed microstrip patch antennas on a cylindrical body of arbitrary cross section that may be coated with dielectrics. In this method, we first employed the finite element method to characterize the microstrip patch antennas and then applied the reciprocity theorem, in conjunction with a two-dimensional method of moments, to calculate the radiated fields. Several numerical examples were presented and compared with measured data to demonstrate the validity of the method. Numerical results were also given to show the effects of patch orientation, dielectric coating, and finiteness of a ground plane on the radiation patterns. The presented method can be used to investigate the effects of external structures (such as the shape and coating) on the radiation patterns of microstrip antennas and to provide reference data for validating more general methods for calculating the radiation patterns of microstrip antennas on general three-dimensional bodies.

References

[1] K. R. Carver and J. W. Mink, "Microstrip antenna technology," *IEEE Trans. Antennas Propagat.*, vol. AP-29, pp. 2-24, Jan. 1981.

[2] W. F. Richards, "Microstrip Antennas," in *Antenna Handbook*. Y. T. Lo and S. W. Lee, Eds. New York: Van Nostrand Reinhold, 1988.

[3] J. R. James and P. S. Hall, *Handbook for Microstrip Antennas*. London: Peter Peregrinus, 1989.

[4] D. M. Pozar, "Input impedance and mutual coupling of rectangular microstrip antennas," *IEEE Trans. Antennas Propagat.*, vol. AP-30, pp. 1191-1196, Nov. 1982.

[5] J. R. Mosig and F. E. Gardiol, "General integral equation formulation for microstrip antennas and scatterers," *Proc. Inst. Elec. Eng.*, vol. 132, part H, pp. 424-432, Dec. 1985.

[6] P. B. Katehi and N. G. Alexopoulos, "Real axis integration of Sommerfeld integrals with applications to printed circuit antennas," *J. Math. Phys.*, vol. 14, pp. 527-533, 1983.

[7] J. M. Jin and J. L. Volakis, ``A hybrid finite element method for scattering and radiation by microstrip patch antennas and arrays residing in a cavity," *IEEE Trans. Antennas Propagat.*, vol. AP-39, pp. 1598-1604, Nov. 1991.

[8] C. M. Krowne, "Cylindrical-rectangular microstrip antenna," *IEEE Trans. Antennas Propagat.*, vol. AP-31, pp. 194-199, 1983.

[9] J. Ashkenazy, S. Shtrikman, and D. Treves, "Electric surface current model for the analysis of microstrip antennas on cylindrical bodies," *IEEE Trans. Antennas Propagat.*, vol. AP-33, pp. 295-300, Mar. 1985.

[10] E. V. Sohtell, "Microstrip antennas on a cylindrical surface," in *Handbook of Microstrip Antennas.* J. R. James and P. S. Hall, Eds. London: Peter Peregrinus, 1989.

[11] L. C. Kempel, "Radiation and scattering from cylindrically conformal printed antennas," Ph.D. dissertation, Univ. of Michigan, Ann Arbor, 1994.

[12] J. M. Jin, *The Finite Element Method in Electromagnetics.* New York: Wiley, 1993.

[13] J. M. Jin and S. W. Lee, "Hybrid finite element analysis of scattering and radiation by a class of waveguide-fed structures," *Microwave Opt. Tech. Lett.*, vol. 7, no. 17, pp. 798-803, 1994.

[14] R. F. Harrington, *Time-Harmonic Electromagnetic Fields.* New York: McGraw-Hill, 1961.

[15] J. M. Jin, V. V. Liepa, and C. T. Tai, ``A volume-surface integral equation for electromagnetic scattering by inhomogeneous cylinders," *J. Electromagn. Waves Appl.*, vol. 2, no. 5/6, pp. 573-588, 1988.

[16] J. M. Jin and V. V. Liepa, ``Simple moment method program for computing scattering from complex cylindrical obstacles," *Proc. Inst. Elec. Eng.*, vol. 136, part H, pp. 321-329, Aug. 1989.

[17] J. Huang, "The finite ground plane effect on the microstrip antenna radiation patterns," *IEEE Trans. Antennas Propagat.*, vol. AP-31, pp. 649-653, July 1983.

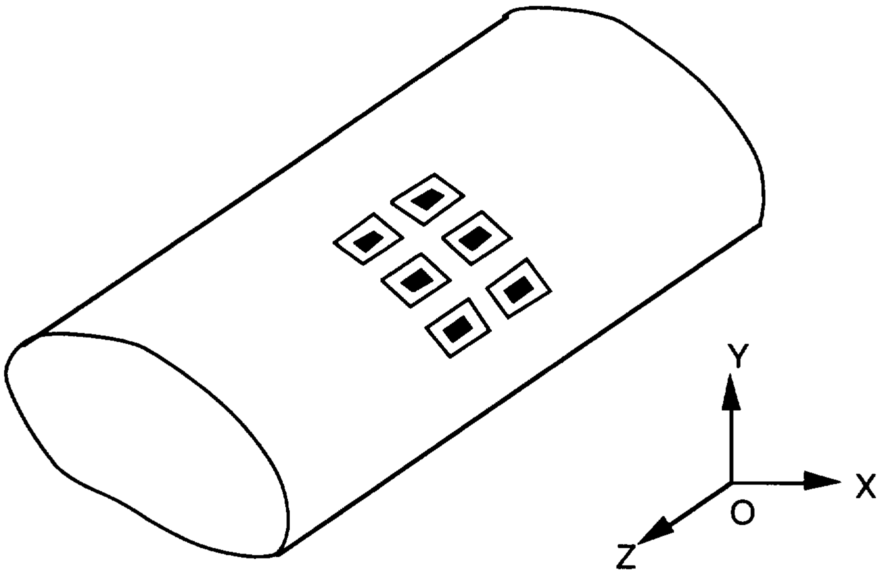

Figure 1. Cavity-backed microstrip patch antennas on the surface of a cylindrical body with an arbitrary cross section.

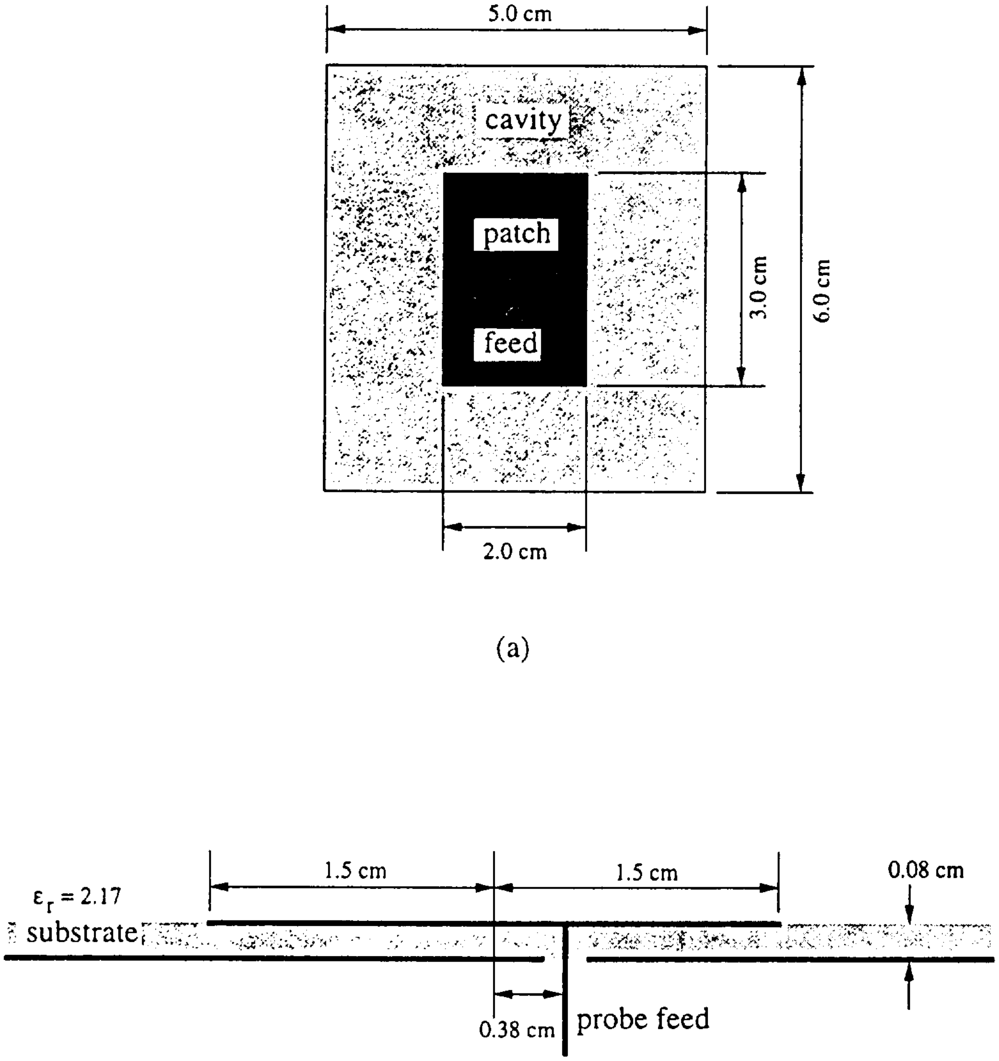

(a)

(b)

Figure 2. Configuration of a cavity-backed microstrip patch antenna. (a) Top view. (b) Side view.

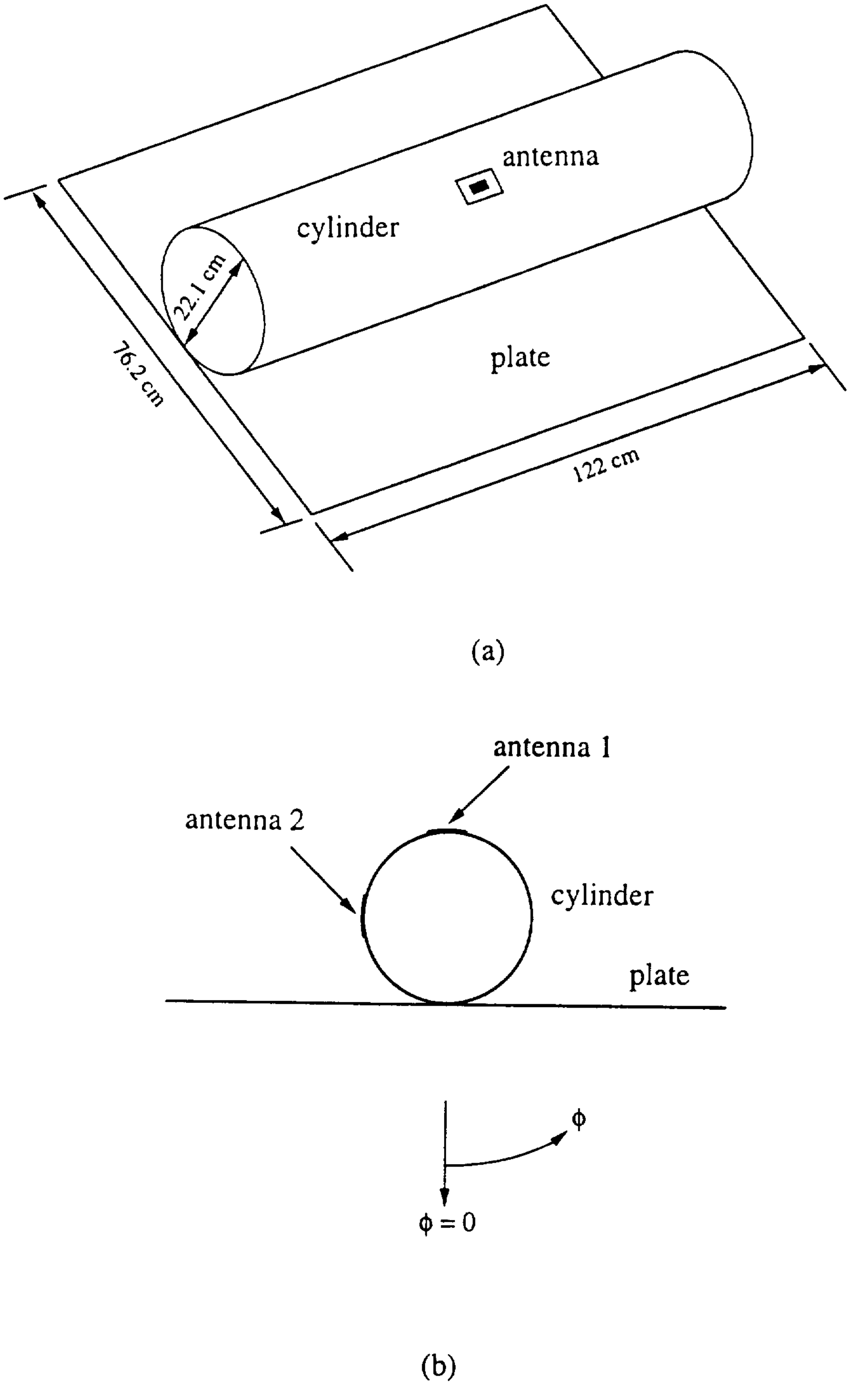

Figure 3. A microstrip patch antenna on a circular cylinder attached to a plate. (a) Three-dimensional view. (b) Cross-sectional view.

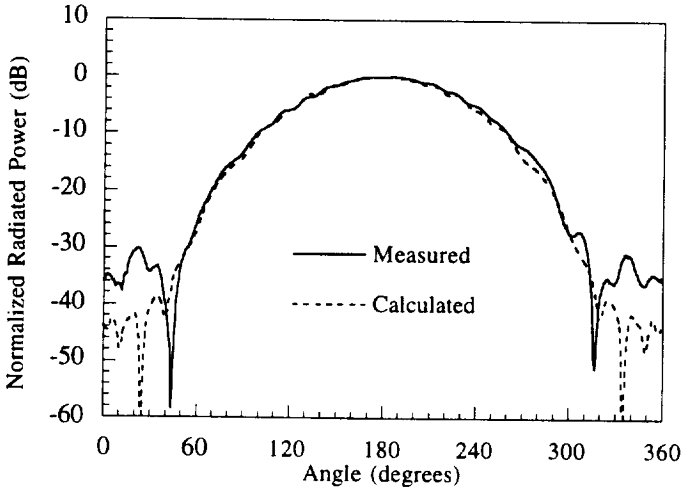

(a)

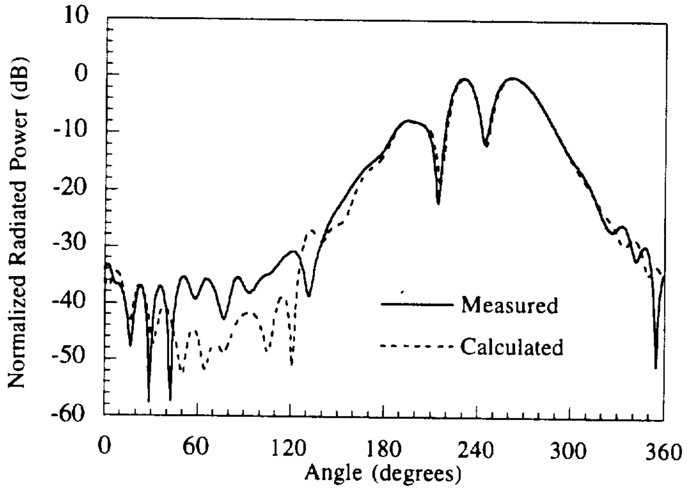

(b)

Figure 4. Radiation patterns of a microstrip patch antenna on a circular cylinder attached to a plate, with the longer side of the patch parallel to the axis of the cylinder. (a) For antenna 1. (b) For antenna 2.

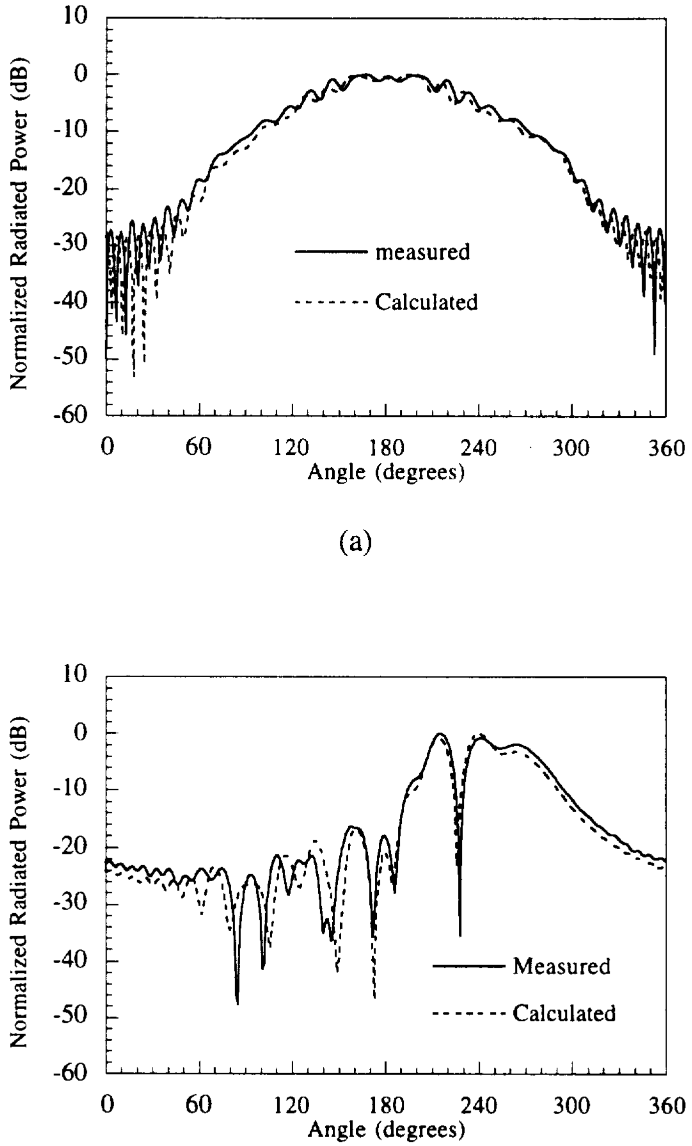

(a)

(b)

Figure 5. Radiation patterns of a microstrip patch antenna on a circular cylinder attached to a plate, with the shorter side of the patch parallel to the axis of the cylinder. (a) For antenna 1. (b) For antenna 2.

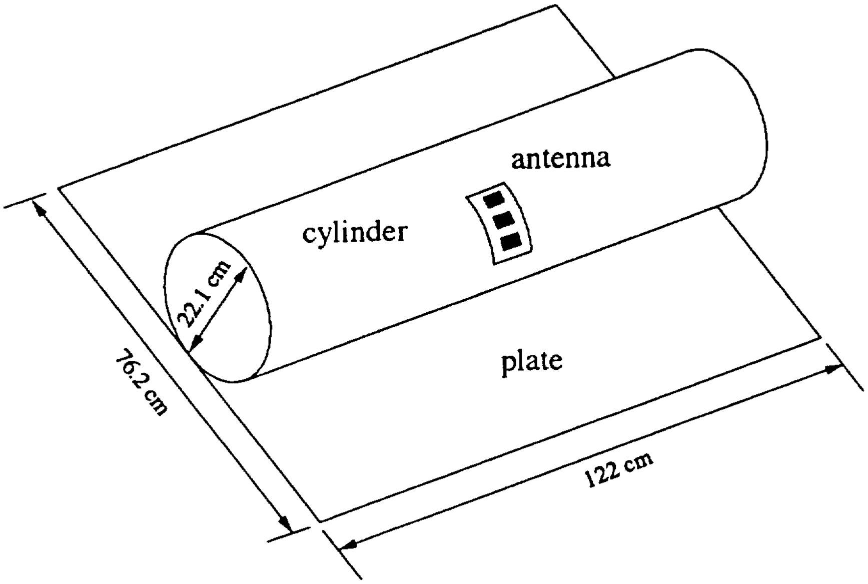

Figure 6. Three microstrip patch antennas on a circular cylinder attached to a plate.

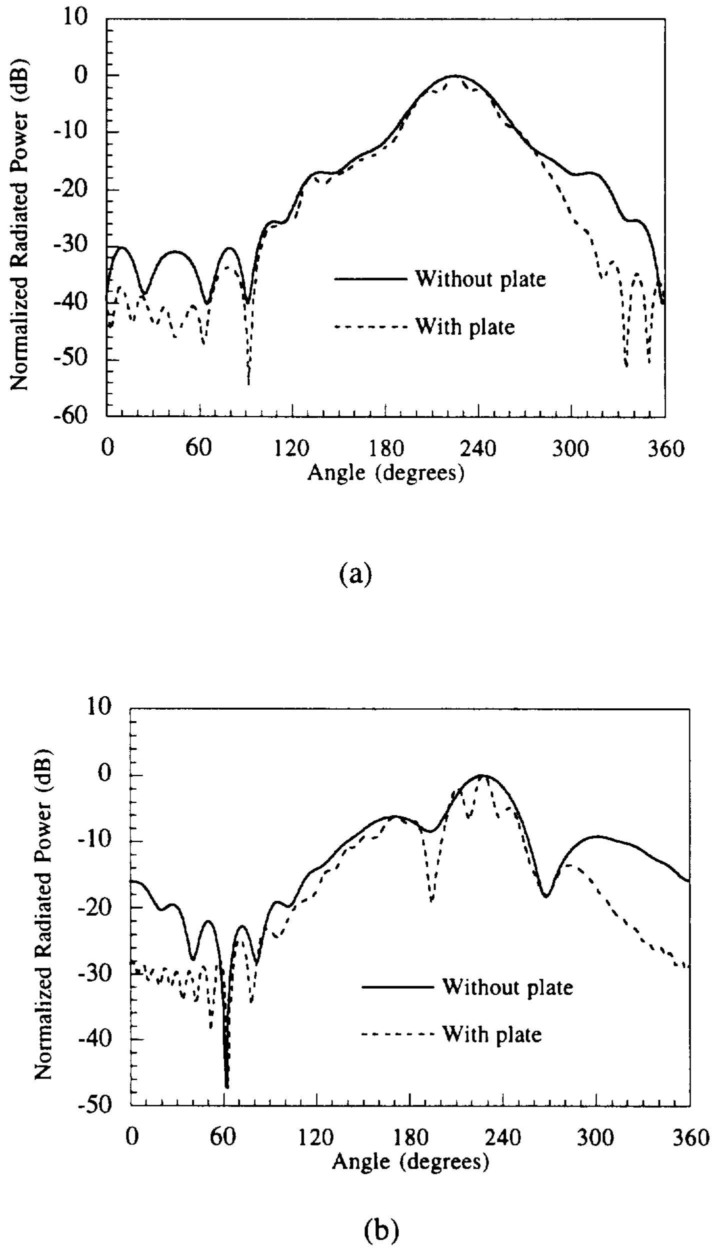

Figure 7. Radiation patterns of three microstrip patch antennas depicted in Fig. 6. (a) With the longer side of the patches parallel to the axis of the cylinder. (b) With the shorter side of the patches parallel to the axis of the cylinder.

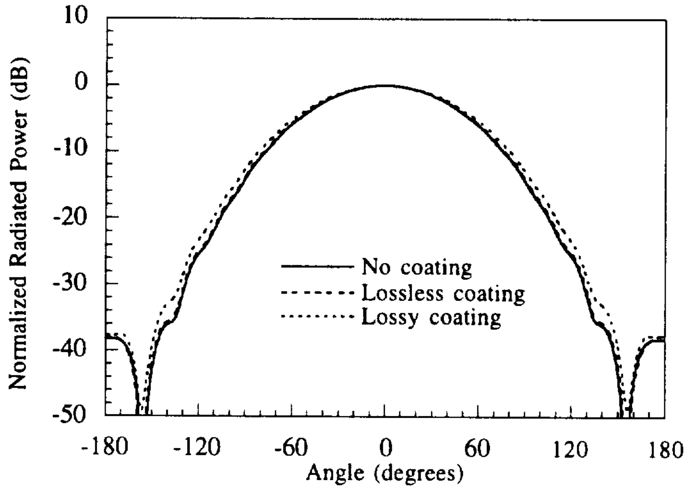

(a)

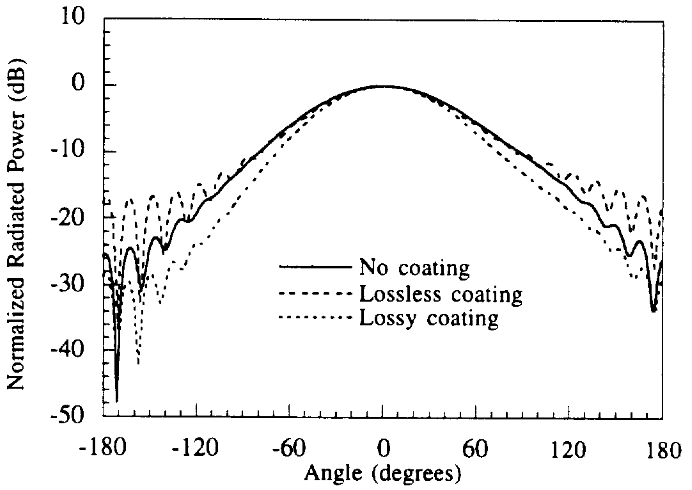

(b)

Figure 8. Radiation patterns of a microstrip patch antenna on a dielectric coated circular cylinder. (a) With the longer side of the patch parallel to the axis of the cylinder. (b) With the shorter side of the patch parallel to the axis of the cylinder.

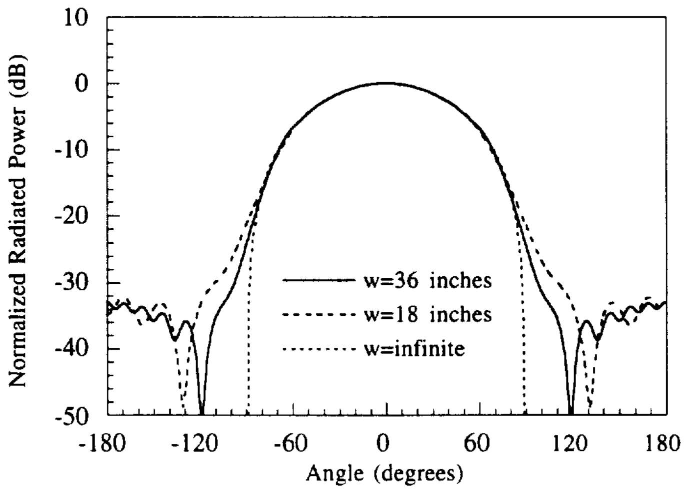

(a)

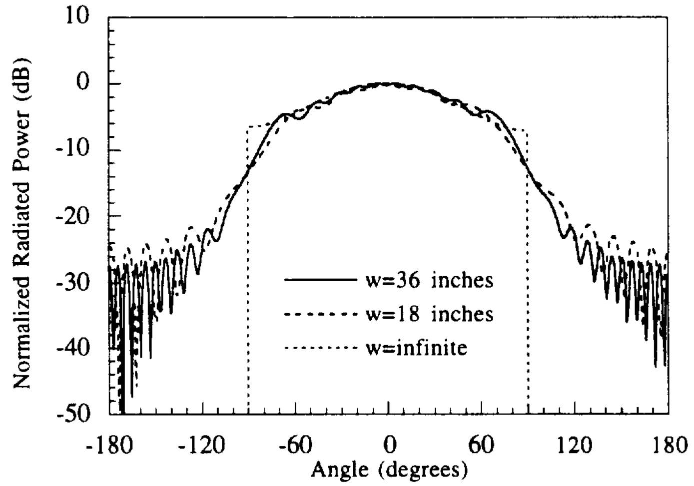

(b)

Figure 9. Radiation patterns of a microstrip patch antenna on a flat conducting plate having width w. (a) With the longer side of the patch parallel to the axis of the plate. (b) With the shorter side of the patch parallel to the axis of the plate.

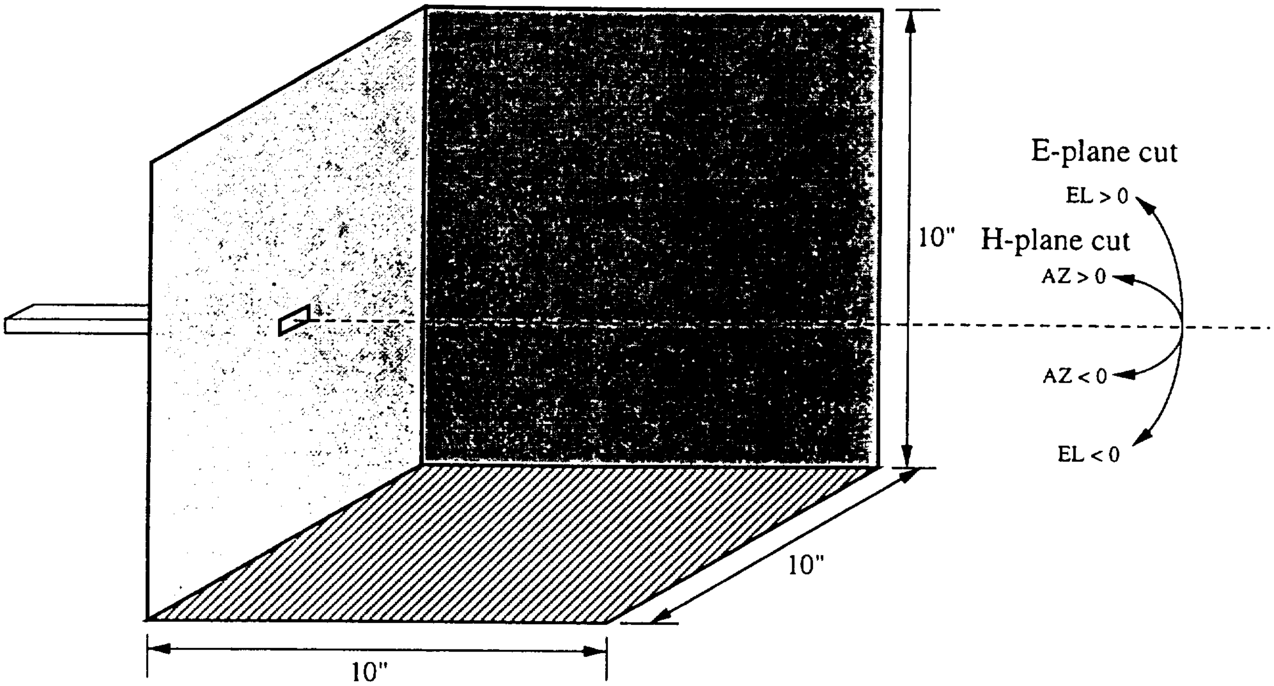

Figure 10. Configuration of a waveguide-fed trihedral. The waveguide is 0.9 inch wide and 0.4 inch thick and located at the center of one of the planes.

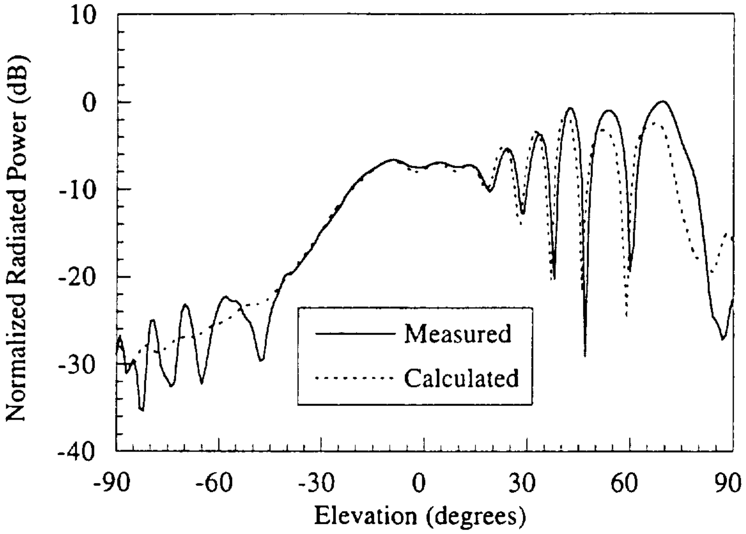

(a)

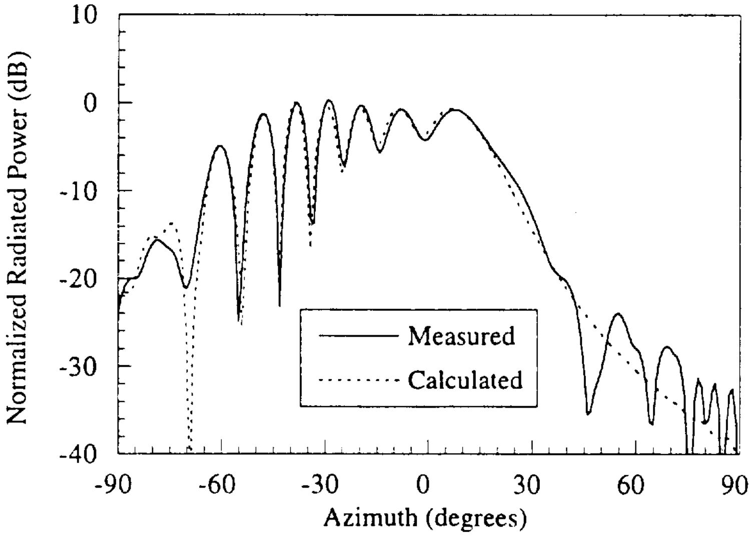

(b)

Figure 11. The radiation patterns of a waveguide-fed trihedral at $f = 9.0$ GHz. (a) In *E*-plane cut. (b) In *H*-plane cut.

APPENDIX 2

Hybrid FEM/SBR Method to Compute the Radiation Pattern from a Microstrip Patch Antenna in a Complex Geometry

A. D. Greenwood, S. S. Ni, J. M. Jin, and S. W. Lee
Center for Computational Electromagnetics
Department of Electrical and Computer Engineering
University of Illinois at Urbana-Champaign
Urbana, Illinois 61801-2991

Key terms: Finite element method, shooting and bouncing ray method, microstrip patch antenna, radiation.

Abstract

A previously introduced technique to compute the radiation of a microstrip patch antenna on a cylindrical body of arbitrary cross-section is extended to include patch antennas mounted on complex, three-dimensional bodies. The technique involves using the finite element method (FEM) to characterize the patch antenna, and then computing the radiation pattern using the reciprocity theorem and the shooting and bouncing ray (SBR) method with edge diffraction. The validity of the calculation and the need for an extension to three dimensions is shown by comparison with measured data for a waveguide-fed trihedral. Other calculations show the effects of the external geometry on the radiation pattern of a microstrip patch antenna.

1 Introduction

Recently, a technique for calculating the radiation pattern of a microstrip patch antenna on a cylindrical body was developed [1]. The technique is a hybrid method using the finite element method (FEM) and the two-dimensional (2-D) method of moments (MoM). The FEM is used to analyze the patch antenna with its aperture closed by a perfect conductor, resulting in an equivalent magnetic current density, **M**. The 2-D

MoM is then used to find the radiation due to **M** in the presence of the cylindrical body. While this technique is simple and works well, its application is limited to patch antennas on 2-D bodies such as cylinders. Although the technique can be extended to 3-D bodies by employing a 3-D MoM, the computational cost is prohibitive. Thus, an alternate method of extension is needed.

In this paper, a technique is presented which replaces the 2-D MoM with the high frequency shooting and bouncing ray (SBR) method combined with edge diffraction. A microstrip patch antenna is now considered on a 3-D complex body. As in the original technique, the FEM is first used to analyze the antenna with its aperture closed by perfect conductor, yielding an equivalent magnetic current density, **M**, over the aperture. The SBR method combined with edge diffraction is then used to find the radiation due to **M** in the presence of the 3-D complex body. The proposed method can also be regarded as the extension of the hybrid FEM/SBR scattering method [2] to radiation problems.

This paper first discusses the theoretical development of the method. It then presents some numerical results, showing the utility of the method. Finally, it compares results generated by the extended technique to measured results for a waveguide-fed trihedral, showing the validity of the method and the need for a 3-D extension.

2 Theoretical Development

Consider a microstrip patch antenna mounted on a 3-D complex structure. Since a microstrip patch antenna is a highly resonant structure, its current distribution and input impedance at resonance are determined mainly by its internal structures such as the shape of the patch and the thicknesses and the dielectric constants of the substrate and the superstrate. Provided that the patch antenna is placed on a locally flat surface, the shape of the host 3-D body has little effect on its current distribution and input impedance. Therefore, the patch antenna can be characterized approximately by assuming that it is placed on an infinitely large ground plane and using the FEM as described in [3]. The FEM analysis provides the solution to the equivalent magnetic current density, **M**, over the aperture of the patch antenna.

Once the equivalent magnetic current density has been calculated, the radiation pattern is obtained by computing the field radiated by **M** in the presence of the host 3-D body. An accurate method to compute the radiated field is to use the 3-D MoM. However, the computational cost is prohibitive, especially for a large 3-D body. A more efficient approach is to use a high-frequency approximation such as the SBR method [4, 5].

There are two approaches to using the SBR method to compute the radiated field. One approach is to first compute the radiated field over a small hemisphere covering the patch antenna. This field is then converted into many rays, which shoot along the radial directions. Each ray is traced as it bounces around the 3-D body, and and the bounces are governed by geometrical optics (GO). At the last hit point, or at each and every hit point, a physical optics type integration is performed to determine the ray contribution to the radiated field. The final result is the summation of the contributions from all the rays. This approach, called the forward calculation, has the advantage of simultaneously computing the radiated field in all directions. However, to obtain accurate results, the field on the hemisphere surrounding the patch antenna must be divided into many rays, and in tracing each ray, its divergence factor must be calculated and tracked.

The second approach is to employ the reciprocity theorem. In this approach, called the backward calculation, an infinitesimal dipole is placed at the observation point, and the SBR method is applied to the dipole radiation. Because the dipole is located far from the structure containing the patch antenna, it produces a plane wave incident upon that structure. The SBR method computes the fields radiated by the dipole using GO and accounting for the phase shifts and the polarization properties of the fields. Because the incident field is due to a plane wave, the ray divergence factor is set to unity. Denoting the field radiated by the patch antenna as $\mathbf{E}_{\mathrm{MSPA}}$, the field radiated by the dipole as $\mathbf{H}_{\mathrm{D}}$, and the current density on the dipole as $\mathbf{J}$, the fields $\mathbf{E}_{\mathrm{MSPA}}$ and

$\mathbf{H}_{\mathrm{D}}$ are then related by the reciprocity theorem,

$$\iiint_V \mathbf{E}_{\mathrm{MSPA}} \cdot \mathbf{J} dV = - \iint_S \mathbf{H}_{\mathrm{D}} \cdot \mathbf{M} dS$$

where V denotes the volume of the dipole and S denotes the aperture of the patch antenna. The integral on the left hand side of the equation evaluates to the component of $\mathbf{E}_{\mathrm{MSPA}}$ in the direction of $\mathbf{J}$ times the strength of the dipole, Il. The quantity $\mathbf{H}_{\mathrm{D}}$ on the right hand side of the equation is also proportional to Il, which is then canceled from the expression. Two orthogonal components of $\mathbf{E}_{\mathrm{MSPA}}$ are found by considering both horizontal and vertical polarizations for the incident plane wave in the SBR calculations, corresponding to different physical orientations of the dipole antenna.

When using the SBR method to find $\mathbf{H}_{\mathrm{D}}$ on the surface of the patch antenna, there may be some directions for which the incident wave is blocked. The SBR calculation will then give $\mathbf{H}_{\mathrm{D}}=0$, an erroneous result. To find an accurate value for $\mathbf{H}_{\mathrm{D}}$, edge diffraction must be included with the SBR calculation.

The geometry for the diffraction computation is shown in Figure 1. An arbitrary edge is subdivided into short segments, and the diffracted electric field from a short edge segment is computed using the "incremental length diffraction coefficients" (ILDC) introduced by Mitzner [6, 7]. The diffracted field from the entire edge is then computed from the sum of the contributions of the segments, and the diffracted magnetic field is found from the electric field using Maxwell's equations. Given a short edge segment of length ℓ, the diffracted field at a distance s from the segment is given in terms of ILDC by [6, 7]

$$\begin{bmatrix} E_\theta^d(P) \\ E_\phi^d(P) \end{bmatrix} = -\frac{1}{s} \begin{bmatrix} d_{\theta\theta} & d_{\theta\phi} \\ d_{\phi\theta} & d_{\phi\phi} \end{bmatrix} \begin{bmatrix} E_\theta^i(Q) \\ E_\phi^i(Q) \end{bmatrix} e^{-jks} \tag{1}$$

in which d_{uv} is given by

$$d_{uv} = \frac{\ell}{4\pi}\, e^{jk\ell(\hat{s}-\hat{s}')\cdot\hat{t}} \left[(\hat{u}\cdot\hat{t})(\hat{t}\cdot\hat{v})\, D_s + \hat{u}\cdot(\hat{t}\times\hat{s})(\hat{t}\times\hat{s}')\cdot\hat{v}\, D_h\right] \text{ sinc}\left[\frac{k(\hat{s}-\hat{s}')\cdot\hat{t}}{2}\right] \tag{2}$$

where $\text{sinc}(x) \equiv \sin x/x$, and D_s and D_h are diffraction coefficients. The coefficients D_s and D_h are defined in terms of the Keller-Ufimtsev diffraction coefficients as

$$D_s = 2e^{j\pi/4}\sqrt{\frac{2\pi k}{\sin\beta_0'\sin\beta_0}}\, D_s^{\text{dif}} \tag{3a}$$

$$D_h = 2e^{j\pi/4}\sqrt{\frac{2\pi k}{\sin\beta_0'\sin\beta_0}}\, D_h^{\text{dif}}. \tag{3b}$$

Denoting the interior wedge angle as $\alpha = (2-n)\pi$, D_s^{dif} and D_h^{dif} are given by [8, 9]

$$D_s^{\text{dif}} = -\frac{e^{-j\pi/4}}{2n\sqrt{2\pi k\sin\beta_0'\sin\beta_0}}\,(D_1 - D_2) \tag{4a}$$

$$D_h^{\text{dif}} = -\frac{e^{-j\pi/4}}{2n\sqrt{2\pi k\sin\beta_0'\sin\beta_0}}\,(D_1 + D_2) \tag{4b}$$

where

$$D_1 = \cot\left[\frac{\pi+(\psi-\psi')}{2n}\right] F[kLg^+(\psi-\psi')] + \cot\left[\frac{\pi-(\psi-\psi')}{2n}\right] F[kLg^-(\psi-\psi')] \tag{5a}$$

$$D_2 = \cot\left[\frac{\pi+(\psi+\psi')}{2n}\right] F[kLg^+(\psi+\psi')] + \cot\left[\frac{\pi-(\psi+\psi')}{2n}\right] F[kLg^-(\psi+\psi')]. \tag{5b}$$

In the above, the function $F[\cdot]$ involves a Fresnel integral and is defined by

$$F[x] = 2j\sqrt{x}e^{jx}\int_{\sqrt{x}}^{\infty} e^{-jt^2}\,dt, \tag{6}$$

and the other parameters are given by

$$L = s\sin\beta_0'\sin\beta_0 \text{ and } g^{\pm}(X) = 1 + \cos(X - 2n\pi N^{\pm}) \tag{7}$$

where $N^{\pm}$ are the integers which most closely satisfy

$$2n\pi N^{+} - X = +\pi \text{ and } 2n\pi N^{-} - X = -\pi. \tag{8}$$

It should be noted that the expressions above compute only the first order edge diffracted field. Thus, the incident field used in the calculations is that resulting from direct illumination of the edge. Multiply bounced rays are not included in the edge diffraction computation, nor are fields diffracted by one edge and then subsequently diffracted by a second edge. In most cases, a first order edge diffraction computation is adequate for determining the dominant effects on the radiation pattern of a microstrip patch antenna.

3 Numerical Results

To illustrate the usefulness of the proposed method, numerical results are generated for a patch antenna in two different geometries. The patch antenna under consideration for these tests is shown in Figure 2. The antenna resonates at 3.3 GHz, and, according to the proposed method, it is characterized by an equivalent magnetic current density found using the FEM.

The first example involves placing the patch antenna on a finite, circular ground plane. In Figure 3, the resulting computations of the H-plane and E-plane radiation patterns are compared to the patterns generated by the same antenna on an infinite ground plane. As can be seen, significant features of the antenna pattern are missed by assuming an infinite ground plane to make calculations. Edge diffraction is primarily responsible for the differences between the finite ground plane examples and the infinite ground plane results.

For the second example, the patch antenna is placed on a stair-step geometry shown in Figures 4a and b. In Figures 4c and d, the computed radiation patterns (H-plane and E-plane) are compared to those found by assuming an infinite ground plane to make the calculations. Like the finite, circular ground plane case, significant features are missed by assuming an infinite ground plane, and edge diffraction is primarily responsible for these features.

To show the validity of the method, numerical computations are compared to measured data for a waveguide-fed trihedral. The geometry for this comparison is shown in Figure 5a where the waveguide is 0.9 inch wide by 0.4 inch thick, and the operating frequency is 9.0 GHz. Under these conditions, an incident TE_{10} wave propagates in the waveguide, and the aperture is characterized by an equivalent magnetic current density, similar to the characterization of a patch antenna by an equivalent current density. The calculated radiation patterns (H-plane and E-plane) are compared to the measured patterns in Figures 5b and c. The calculated results agree with the measured results very well.

Although it is a 3-D problem, this waveguide-fed trihedral configuration was considered previously using the 2-D MoM [1]. The MoM result agrees well with the measured result for the H-plane pattern when the azimuth angle is between $-90°$ and $40°$, and it agrees well for the E-plane pattern when the elevation angle is between $-40°$ and $90°$. However, it misses the oscillations in the radiated power outside of these regions. The oscillations that are missed in the 2-D MoM computation are correctly predicted by the SBR/edge diffraction computation and are caused by edge diffraction in the third dimension. Thus, this problem not only validates the method, but underscores the need to extend the original 2-D technique to consider 3-D problems.

4 Conclusion

The technique for computing the radiation pattern from a microstrip patch antenna on a cylindrical body [1] was extended to compute the radiation from a patch antenna in a 3-D complex geometry. The method first involved using the FEM to analyze the antenna. The result was an equivalent magnetic current density on the aperture of the antenna. Then, the SBR method was used to calculate the radiated field, and for this a plane wave was launched toward the antenna by an infinitesimal dipole. The SBR method was used to find the resulting magnetic field on the aperture of the patch antenna, and the radiated field was calculated using the reciprocity theorem. To insure accuracy, the field diffracted by edges was computed using ILDC and added to the SBR result. Numerical results showed that the structures surrounding the patch antenna have dominant effects on the radiation pattern, and assuming an infinite ground plane to make calculations misses these effects. Comparison of numerical results generated by the method to measured data showed good agreement. Finally, comparison of numerical results from the method presented here to those from the original 2-D MoM technique showed that pattern features missed by the 2-D technique are correctly predicted by this technique.

References

[1] J. M. Jin, J. A. Berrie, R. Kipp, and S. W. Lee, "Calculation of Radiation Patterns of Microstrip Antennas on Cylindrical Bodies of Arbitrary Cross Section," submitted to *IEEE Trans. Antennas Propagat.*, July 1995.

[2] J. M. Jin, S. S. Ni, and S. W. Lee, "Hybridization of SBR and FEM for Scattering by Large Bodies with Cracks and Cavities," *IEEE Trans. Antennas Propagat.*, Vol. 43, Oct. 1995, pp. 1130–1139.

[3] J. M. Jin, *The Finite Element Method in Electromagnetics.* New York: Wiley, 1993, ch. 9.

[4] S. W. Lee, D. J. Andersh, D. D. Reeves, S. K. Jeng, H. Ling, Y. Chu, D. P. Sullivan, and C. L. Yu, "User Manual for Xpatch." DEMACO, Inc., Champaign, IL, 1993.

[5] D. Andersh, M. Hazlett, S. W. Lee, D. D. Reeves, D. P. Sullivan, and Y. Chu, "XPATCH: A High-Frequency Electromagnetic-Scattering Prediction Code and Environment for Complex Three-Dimensional Objects," *IEEE Antennas Propagat. Mag.*, Vol. 36, Feb. 1994, pp. 65–69.

[6] S. W. Lee and S. K. Jeng, "NcPTD - 1.2: A High Frequency Near-Field RCS Computation Code Based on the Physical Theory of Diffraction," Tech. Rep. DI-SC-90-012, DEMACO, Inc., Champaign, IL, June 1991.

[7] K. M. Mitzner, "Incremental Length Diffraction Coefficients," Tech. Rep. AFAL-TR-73-296, Aircraft Division, Northrop Corp., Apr. 1974.

[8] C. A. Balanis, *Advanced Engineering Electromagnetics.* New York: Wiley, 1989, ch. 13.

[9] S. K. Jeng and S. W. Lee, "Two New Diffraction Coefficients for Physical Theory of Diffraction," Electromagnetics Lab. Sci. Rep. 94-2, Univ. IL., Jan. 1994.

Figure 1: Geometry of edge diffraction. Note that ψ' and ψ are measured from an illuminated face of the wedge, so $0 < \psi' < \pi$ and $0 < \psi < n\pi$ where $\alpha = (2 - n)\pi$.

Figure 2: Microstrip patch antenna considered in computational tests.

Figure 3: Radiation pattern of a microstrip patch antenna on a finite, circular ground plane.

Figure 4: Radiation pattern of a microstrip patch antenna on a stair-step geometry.

Figure 5: Comparison of calculated data with measured data for the radiation pattern of a waveguide-fed trihedral at 9.0 GHz.

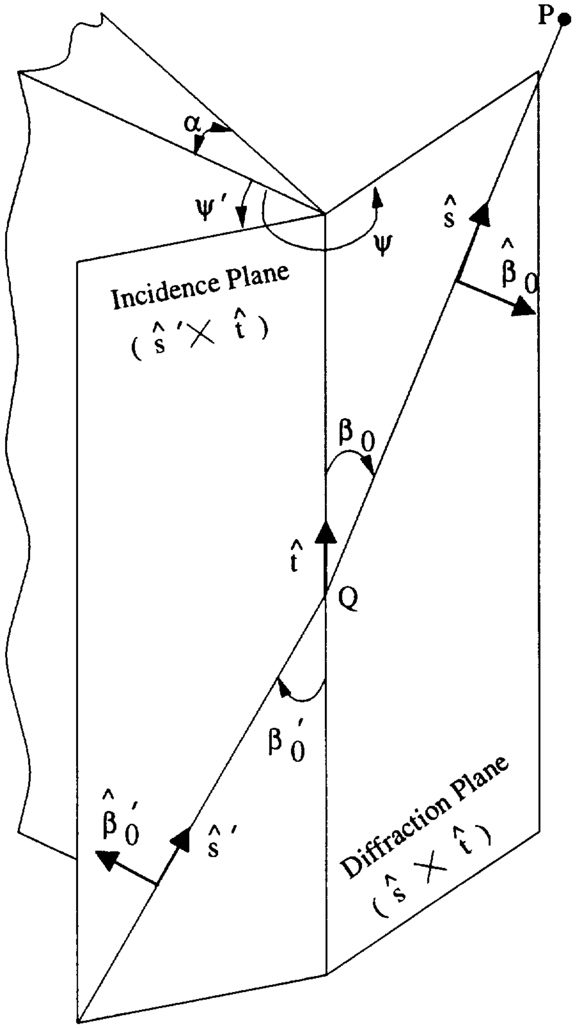
P
α
ψ′
ψ
$\hat{s}$
$\hat{\beta}_0$
Incidence Plane
$(\hat{s}' \times \hat{t})$
β_0
$\hat{t}$
Q
β_0'
$\hat{\beta}_0'$
$\hat{s}'$
Diffraction Plane
$(\hat{s} \times \hat{t})$

Figure 1:

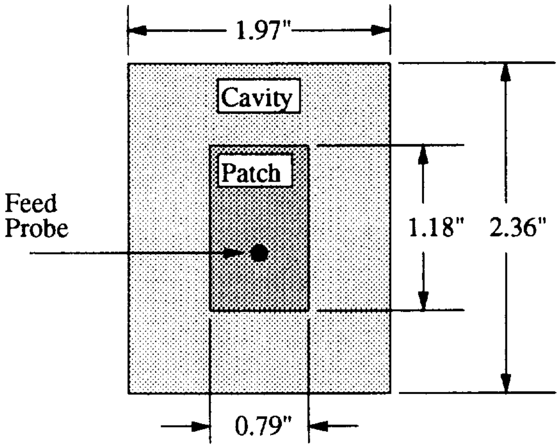

(a) Top view

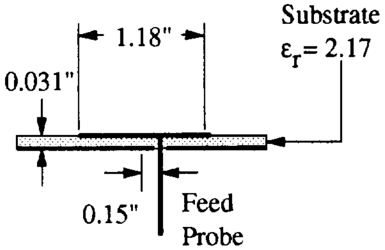

(b) Side view

Figure 2:

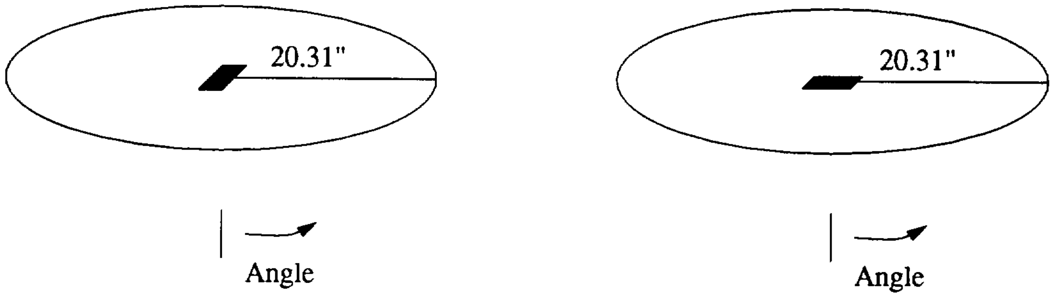

(a) H-plane Geometry

(b) E-plane Geometry

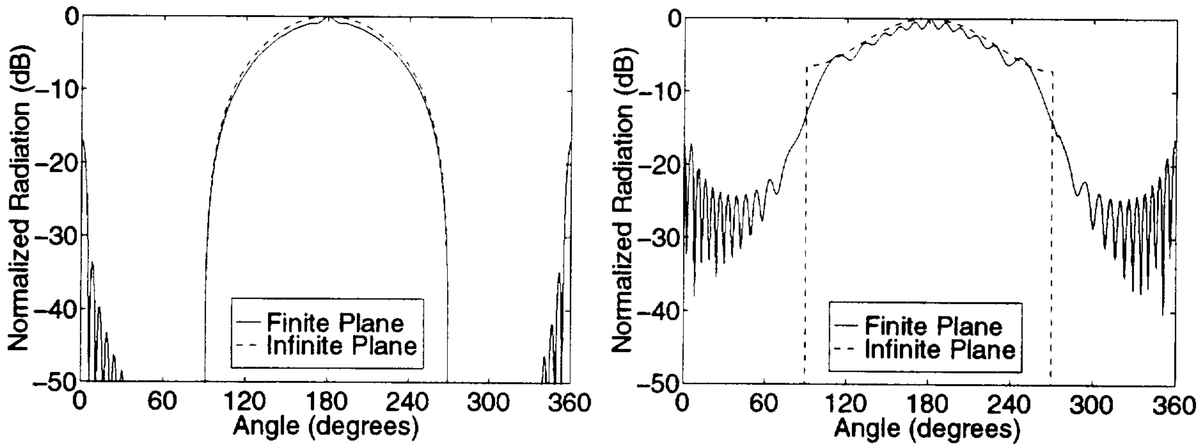

(c) H-plane pattern

(d) E-plane pattern

Figure 3:

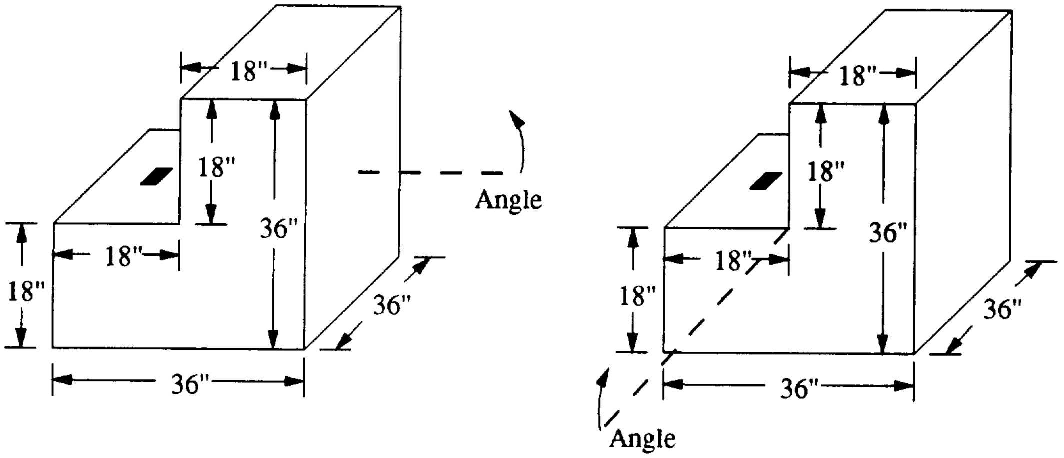

(a) H-plane Geometry

(b) E-plane Geometry

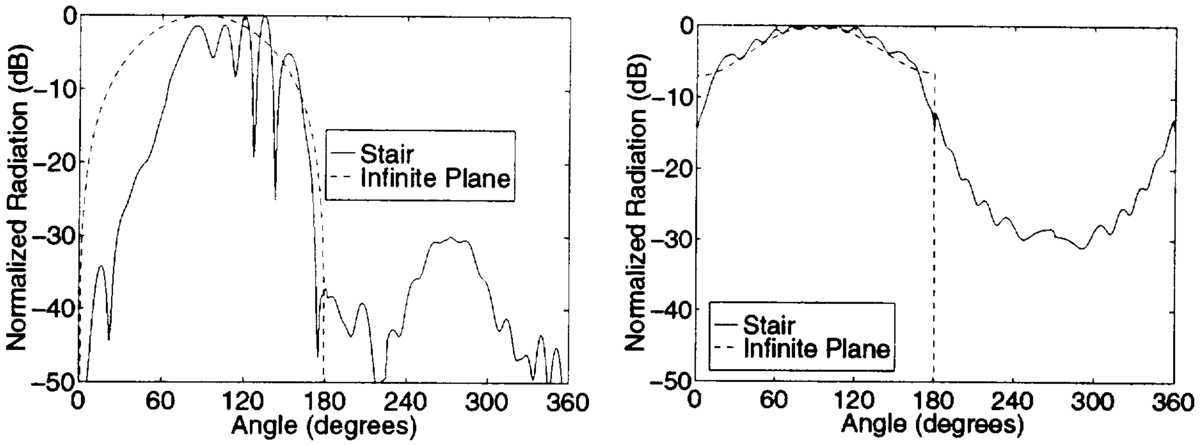

(c) H-plane pattern

(d) E-plane pattern

Figure 4:

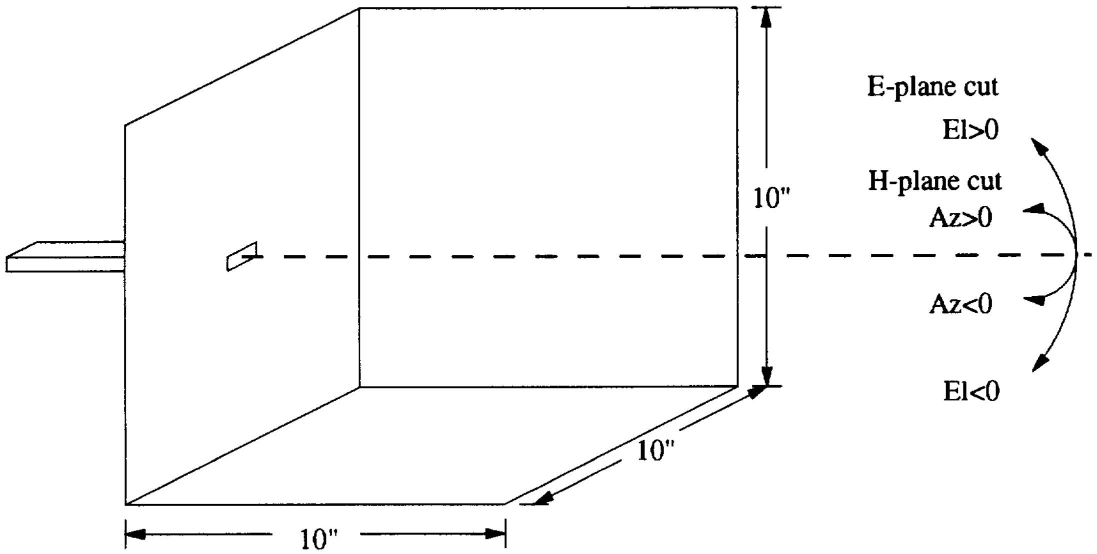

(a) Geometry

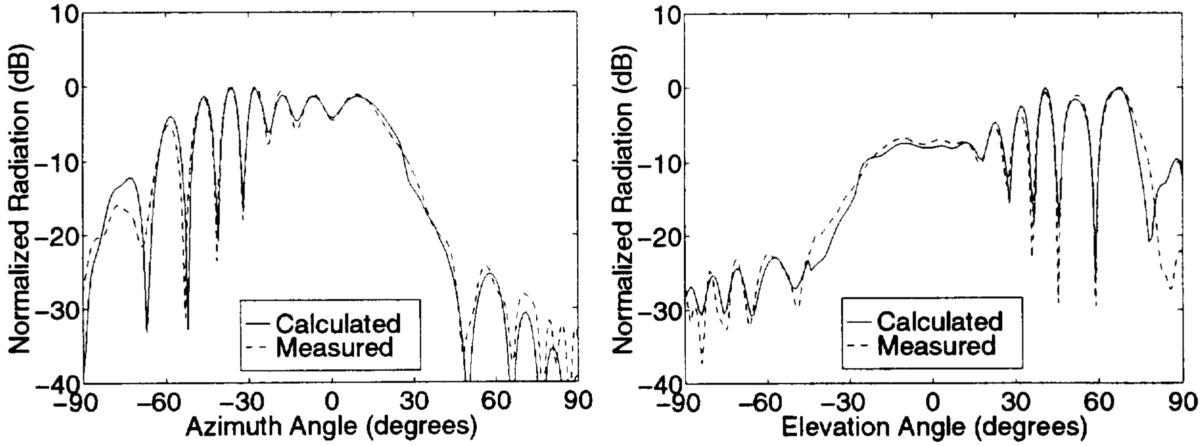

(b) H-plane pattern

(c) E-plane pattern

Figure 5:

APPENDIX 3

SCATTERING FROM A CYLINDRICALLY CONFORMAL SLOTTED-WAVEGUIDE ARRAY ANTENNA

Guo-Xin Fan and Jian-Ming Jin
Electromagnetics Laboratory
Department of Electrical and Computer Engineering
University of Illinois at Urbana-Champaign
Urbana, Illinois 61801-2991

ABSTRACT

A numerical method is developed to investigate electromagnetic scattering by a cylindrically conformal waveguide-fed slot array. The problem is first formulated in terms of integral equations using the equivalence principle. The integral equations are then solved using the method of moments (MoM) in conjunction with global sinusoidal basis functions and Galerkin's testing procedure. The MoM solution requires the evaluation of the generalized admittance matrices involving various dyadic Green's functions. The slow convergence of the series associated with the summation of waveguide modes is accelerated using the Kummer transformation and the slow convergence of the series associated with the summation of the exterior modes is avoided by using the asymptotic solutions with proper treatment for singular integrals. The evaluation of the excitation vector and scattered field is also accelerated using Watson's transformation and asymptotic solutions. Numerical results are presented to illustrate the scattering characteristics of the cylindrically conformal waveguide-fed slot arrays, such as the effects of curvature, slot thickness, and waveguide termination on the radar cross section of the arrays.

I. INTRODUCTION

Slotted-waveguide array antennas are widely used on modern airborne radars because of their large power handling capability, high efficiency, light weight, compact structure, and low side lobes. However, being highly efficient radiating structures, by reciprocity theorem these antennas are also efficient scatterers, which contribute significantly to the overall radar cross section (RCS) of the host vehicle. Usual RCS reduction techniques cannot be applied to these antennas without degrading their performance. Bandpass radomes, made of frequency selective surfaces (FSS), can reflect nearly all the incident energy outside the working frequency band and allow the incident energy within the working frequency band pass through to reach the antennas. However, it is at the working frequency band that the slot arrays have a significantly higher RCS. Therefore, it is necessary to predict the RCS of the slot arrays for applications such as target identification, electromagnetic compatibility, and stealth technology.

Because of a large number of slots and the mutual coupling between the slots through the waveguides and exterior space, a full-wave analysis of slotted waveguide arrays is very difficult. In the past, most work was focused on the radiation analysis of a single slot [1]-[10], one-dimensional arrays and small two-dimensional arrays [11]-[17], all in a planar surface. In particular, Stevenson [1] developed what is now considered the classical theory for a single slot and Oliner [2] presented a variational solution of the problem. Khac and Carson [3] employed the method of moments (MoM) to seek a numerical solution to the slot field using pulse basis functions and point match technique. The efficiency of the MoM solution was improved by Lyon and Sangster [5] and Stern and Elliott [6] by using global and piecewise sinusoidal basis functions and Galerkin's technique. The MoM was also applied to tilted slots [9], dielectric-covered slots [8], [10], edge slots [18], and slots in a sectoral waveguide [19]. Recently, Fan [20] analyzed cylindrically conformal slotted-waveguide array antennas with a curved waveguide as the feeding guide and sectoral guides as the radiating guides. Whereas the literature for the radiation analysis of the slot arrays is abundant, little work was done on the scattering from the planar slot antennas [21]-[23], let alone the curved ones. Josefsson [21] analyzed scattering by a single slot in an infinitely long waveguide and Chen and Jin [23] developed the MoM and finite element method (FEM) solutions for the slots in the waveguides terminated with arbitrary loads. No work was found on the analysis of the scattering characteristics of slotted waveguide arrays on a curved surface. In this paper, we present such an analysis.

The key problem in the analysis of slotted waveguide arrays is to solve for the slot aperture fields. Among various numerical methods, the MoM is most efficient and accurate for this purpose because only a small number of basis functions are needed to represent the aperture fields. However, the major difficulties in the MoM are (i) its formulation requires the dyadic Green's functions for the waveguide, the exterior space, and the slot if it has a finite thickness, and (ii) the evaluation of its matrix involves highly singular integrals and very slowly converging series. In this paper, we address all these problems. To be more specific, we first formulate the integral equations for the problem and apply the MoM with global basis functions and Galerkin's testing procedure. We then describe in detail the evaluation of the MoM matrix involving various dyadic Green's functions. The slow convergence of the series associated with the summation of waveguide modes is accelerated using the Kummer transformation and the slow convergence of the series associated with the summation of the exterior modes is avoided by using the asymptotic solutions developed by Boersma and Lee [24] and Bird [25]. The evaluation of the excitation vector and scattered field is also accelerated using Watson's transformation and asymptotic solutions. Finally, we present some numerical results to illustrate the scattering characteristics of the cylindrically conformal slotted waveguide arrays, such as the effects of curvature, slot thickness, waveguide termination, and frequency on the RCS of the arrays.

II. THEORY

In this section, we describe in detail the formulation of the problem and its solution by the MoM. Particular attention is given to the computation of the elements of the generalized admittance matrices.

A. Integral Equations and MoM Solution

Consider the problem of electromagnetic wave scattering by a waveguide-fed slot array on a cylindrical surface whose radius is ρ_3, as depicted in Fig. 1. The cross section of each waveguide is an annular sector with inner radius ρ_1, outer radius ρ_2, and subtended angle $\Delta\phi$, and the thickness of the curved walls of the waveguides is $t = \rho_3 - \rho_2$. Each waveguide is terminated at $z = z_1$ and z_2 with an arbitrary load. All radiating slots are longitudinal slots cut in the outer wall of the waveguides, having the same width $2w$ and different length and offset with respect to the center-line of the waveguides.

For the ith slot, its inner and outer apertures, S_i^I and S_i^{II}, divide the space into three regions: the waveguide region (region a), the region outside the cylinder (region b), and the slot region (region c), as illustrated in Fig. 2. In accordance with the equivalence principle, the fields in the three regions can be decoupled by covering the apertures S_i^I and S_i^{II} with a perfectly conducting surface and introducing equivalent magnetic currents above and below the perfectly conducting surface. Denoting the equivalent magnetic current below S_i^I as $\mathbf{M}_i^I$ and that below S_i^{II} as $\mathbf{M}_i^{II}$, because of the continuity of the tangential electric fields across the apertures, the equivalent magnetic current above S_i^I is $-\mathbf{M}_i^I$ and that above S_i^{II} is $-\mathbf{M}_i^{II}$. Therefore, the field in region a is due to $\mathbf{M}_i^I$, the field in region b is due to $-\mathbf{M}_i^{II}$ and the incident field, and the field in region c is due to $-\mathbf{M}_i^I$ and $\mathbf{M}_i^{II}$.

By enforcing the continuity of the tangential magnetic fields across S_i^I and S_i^{II}, we obtain the integral equations satisfied by the equivalent magnetic currents, $\mathbf{M}_i^I$ and $\mathbf{M}_i^{II}$, as

$$\sum_j \mathbf{H}^a_{\tau i}(\mathbf{M}_j^I) + \mathbf{H}^c_{\tau i}(\mathbf{M}_i^I) - \mathbf{H}^c_{\tau i}(\mathbf{M}_i^{II}) = 0 \qquad \mathbf{r} \in S_i^I \tag{1}$$

$$\sum_j \mathbf{H}^b_{\tau i}(\mathbf{M}_j^{II}) + \mathbf{H}^c_{\tau i}(\mathbf{M}_i^{II}) - \mathbf{H}^c_{\tau i}(\mathbf{M}_i^I) = \mathbf{H}^{pri}_{\tau i} \qquad \mathbf{r} \in S_i^{II} \tag{2}$$

where the subscript τ denotes the tangential component, the summation in (1) is carried out for all inner apertures in the same waveguide, and the summation in (2) is carried out for all outer apertures. The magnetic field is related to the surface magnetic current by

$$\mathbf{H}^\alpha(\mathbf{r}) = \iint_S \overline{\overline{G}}^\alpha(\mathbf{r}, \mathbf{r}') \cdot \mathbf{M}(\mathbf{r}') dS' \tag{3}$$

where $\alpha = a$ for region a, b for region b, and c for region c, respectively, and $\overline{\overline{G}}^\alpha(\mathbf{r}, \mathbf{r}')$ denotes the magnetic-source magnetic-field dyadic Green's function in the corresponding region. Finally, $\mathbf{H}^{pri}$ is the field due to the incident field in the presence of the conducting cylinder without slots.

To seek a numerical solution of (1) and (2), we first expand each equivalent magnetic current using the global sinusoidal basis functions

$$\mathbf{M}_j^I = \hat{z} M_j^I = \hat{z} \sum_{q=1}^{N_j^I} V_{qj}^I \sin \alpha_{qj} \xi \qquad \mathbf{r} \in S_j^I \tag{4}$$

$$\mathbf{M}_j^{II} = \hat{z} M_j^{II} = \hat{z} \sum_{q=1}^{N_j^{II}} V_{qj}^{II} \sin \alpha_{qj} \xi \qquad \mathbf{r} \in S_j^{II} \tag{5}$$

where $\alpha_{qj} = q\pi / L_j$ with L_j being the length of the jth slot, and choose the testing or weighting functions as

$$\mathbf{W}_{pi}^{I} = \hat{z} W_{pi}^{I} = \hat{z} \sin \alpha_{pi} \xi \qquad \mathbf{r} \in S_i^{I} \tag{6}$$

$$\mathbf{W}_{pi}^{II} = \hat{z} W_{pi}^{II} = \hat{z} \sin \alpha_{pi} \xi \qquad \mathbf{r} \in S_i^{II}. \tag{7}$$

Applying Galerkin's procedure, the integral equations can be converted into the matrix equation given by

$$\begin{bmatrix} [Y_{pq}^{ij}(a) + Y_{pq}^{ij}(c, S_i^{I}; S_j^{I})] & [-Y_{pq}^{ij}(c, S_i^{I}; S_j^{II})] \\ [-Y_{pq}^{ij}(c, S_i^{II}; S_j^{I})] & [Y_{pq}^{ij}(b) + Y_{pq}^{ij}(c, S_i^{II}; S_j^{II})] \end{bmatrix} \begin{Bmatrix} [V_{qj}^{I}] \\ [V_{qj}^{II}] \end{Bmatrix} = \begin{Bmatrix} [0] \\ [I_{pi}] \end{Bmatrix} \tag{8}$$

where $\left[Y_{pq}^{ij}(a)\right]$ and $\left[Y_{pq}^{ij}(b)\right]$ are the generalized admittance matrix for regions a and b, respectively. $\left[Y_{pq}^{ij}\left(c, S_i^{f}; S_j^{s}\right)\right]$ is the generalized admittance matrix for region c, in which S_i^{f} is the aperture on which the field point is located and S_j^{s} is the aperture on which the source point is located. Finally, $[I_{pi}]$ is the generalized excitation vector.

We note that for slots of zero thickness, the edge condition is often employed to represent the transverse distribution of the equivalent magnetic current [6], [10], [14], which makes the evaluation of the matrix elements difficult. For slots of finite thickness as is the case for practical applications, the singularity is much weaker than that for the zero thickness case. As a result, the equivalent magnetic current can be expanded in terms of the global sinusoidal basis functions with a uniform transverse distribution. Such an expansion has been successfully used in the past for the analysis of rectangular waveguide slot radiation problems [5], [8], [9].

In the remainder of this section, we describe the evaluation of the elements of each generalized admittance matrix and excitation vector, necessary for a numerical solution of (8).

B. Generalized Admittance Matrix Elements for Region a

The admittance matrix elements due to the internal coupling in the sectoral waveguide (region a) are given by

$$Y_{pq}^{ij}(a) = \iint\limits_{S_i^{I}} \iint\limits_{S_j^{I}} G_{zz}^{a}(\mathbf{r}, \mathbf{r}') \sin \alpha_{pi} \xi \, \sin \alpha_{qj} \xi' \, dS \, dS' \tag{9}$$

where G_{zz}^{a} is the $\hat{z}\hat{z}$-component of the magnetic-source magnetic-field dyadic Green's function for the sectoral waveguide, which is derived in Appendix A and given by

$$G_{zz}^{a} = j\omega\epsilon \sum_{m=0}^{\infty} B(m,n) \, C_{\varphi} \, C_{\varphi'} \left\{ \delta(z - z') \right.$$

$$
-\frac{\lambda_{mn}^2}{2jh_{mn}\Delta_{mn}}\Big[e^{-jh_{mn}|z-z'|} - R_{mn}^{<}e^{j2h_{mn}z_1}e^{-jh_{mn}(z+z')}
$$

$$
-R_{mn}^{>}e^{-j2h_{mn}z_2}e^{jh_{mn}(z+z')} + R_{mn}^{<}R_{mn}^{>}e^{-jh_{mn}(z_2-z_1)}e^{jh_{mn}|z-z'|}\Big]\Big\} \tag{10}
$$

where

$$
B(m,n) = \frac{2}{1+\delta_{0m}}\frac{B_\nu(\lambda_{mn}\rho)\,B_\nu(\lambda_{mn}\rho')}{k^2 N_{\lambda_{mn}}\Delta\phi}\Bigg|_{\rho=\rho'=\rho_2} \tag{11}
$$

in which

$$
B_\nu(\lambda_{mn}\rho) = J'_\nu(\lambda_{mn}\rho_1)Y_\nu(\lambda_{mn}\rho) - Y'_\nu(\lambda_{mn}\rho_1)J_\nu(\lambda_{mn}\rho) \tag{12}
$$

$$
\begin{aligned}
N_{\lambda_{mn}} &= \int_{\rho_1}^{\rho_2}\rho\Big[B_\nu(\lambda_{mn}\rho)\Big]^2 d\rho \\
&= \frac{1}{2\lambda_{mn}^2}\Big\{(\lambda_{mn}^2\rho^2-\nu^2)\Big[B_\nu(\lambda_{mn}\rho)\Big]^2\Big\}_{\rho_1}^{\rho_2}.
\end{aligned} \tag{13}
$$

Also, in the above, $\nu = m\pi/\Delta\phi$, $C_\varphi = \cos\nu\varphi$, $C_{\varphi'} = \cos\nu\varphi'$, $h_{mn} = \sqrt{k^2-\lambda_{mn}^2}$, λ_{mn} are the roots of $B'_\nu(\lambda_{mn}\rho_2) = 0$, $\Delta_{mn} = 1 - R_{mn}^{<}R_{mn}^{>}e^{-jh_{mn}(z_2-z_1)}$, and $R_{mn}^{<}$ and $R_{mn}^{>}$ are the reflection coefficients for mode $(m,\ n)$ at $z = z_1$ and $z = z_2$, respectively. For shorted terminals $R_{mn} = -1$, and for matched terminals $R_{mn} = 0$.

The integrals in (9) can be evaluated analytically through the transformation of variables, resulting in

$$
\begin{aligned}
Y_{pq}^{ij}(a) &= \int_0^{L_i}\int_{-w}^{w}\int_0^{L_j}\int_{-w}^{w} G_{zz}^{a}(\mathbf{r},\mathbf{r}')\sin\alpha_{pi}\xi\sin\alpha_{qj}\xi'\,d\eta'd\xi'd\eta d\xi \\
&= -j\omega\epsilon\sum_{m=0}^{\infty}\sum_{n=0}^{\infty}B(m,n)I_\varphi^{ij}(m)\left[I_{z0}^{ij}(m,n)+I_{zim}^{ij}(m,n)\right]
\end{aligned} \tag{14}
$$

where $I_\varphi^{ij}(m) = I_\varphi^{i}(m)I_\varphi^{j}(m)$ with

$$
I_\varphi^{i}(0) = 2w \tag{15}
$$

$$
I_\varphi^{i}(m) = \frac{\rho_2}{\nu}\sum_{U=\pm\nu}\operatorname{sgn}(U)\sin\left[\frac{\nu}{\rho_2}\left(\frac{\rho_2\Delta\phi}{2}+\delta_i+U\right)\right] \qquad m\neq 0 \tag{16}
$$

and δ_i denotes the offset of the ith slot from the center of the waveguide. Also,

$$
I_{z0}^{ii}(m,n) = C(m,n)\left[1+(-1)^{p+q}\right]\left[1-(-1)^{p}e^{-jh_{mn}L_i}\right] + \delta_{pq}\frac{(k^2-\alpha_{pi}^2)L_i}{\alpha_{pi}^2-h_{mn}^2} \tag{17}
$$

$$
\begin{aligned}
I_{z0}^{ij}(m,n) &= C(m,n)e^{\mp jh_{mn}[(z_{0i}-z_{0j})-(L_i-L_j)/2]} \\
&\quad\cdot\left[1-(-1)^{p}e^{\mp jh_{mn}L_i}\right]\left[1-(-1)^{q}e^{\pm jh_{mn}L_j}\right] \qquad z_{0i} \gtrless z_{0j}
\end{aligned} \tag{18}
$$

with

$$C(m,n) = \frac{\lambda_{mn}^2}{2jh_{mn}\Delta_{mn}} \frac{\alpha_{pi}}{\alpha_{pi}^2 - h_{mn}^2} \frac{\alpha_{qj}}{\alpha_{qj}^2 - h_{mn}^2} \tag{19}$$

and z_{0i} and z_{0j} denote the center of the ith and jth slots, respectively. Finally, $I_{zim}^{ij}(m,n)$ can be written in three parts as

$$I_{zim}^{ij}(m,n) \;=\; I_{z1}^{ij}(m,n) + I_{z2}^{ij}(m,n) + I_{z3}^{ij}(m,n) \tag{20}$$

with

$$\begin{aligned}
I_{z1}^{ij}(m,n) \;&=\; -C(m,n)R_{mn}^{<}e^{-jh_{mn}[(z_{0i}+z_{0j})-(L_i+L_j)/2-2z_1]} \\
&\quad \cdot\left[1-(-1)^p e^{-jh_{mn}L_i}\right]\left[1-(-1)^q e^{-jh_{mn}L_j}\right] &(21)\\
I_{z2}^{ij}(m,n) \;&=\; -C(m,n)R_{mn}^{>}e^{-jh_{mn}[2z_2-(z_{0i}+z_{0j})+(L_i+L_j)/2]} \\
&\quad \cdot\left[1-(-1)^p e^{jh_{mn}L_i}\right]\left[1-(-1)^q e^{jh_{mn}L_j}\right] &(22)\\
I_{z3}^{ii}(m,n) \;&=\; C(m,n)R_{mn}^{<}R_{mn}^{>}e^{-2jh_{mn}(z_2-z_1)} \\
&\quad \cdot\left[1+(-1)^{p+q}\right]\left[1-(-1)^p e^{jh_{mn}L_i}\right] &(23)\\
I_{z3}^{ij}(m,n) \;&=\; C(m,n)R_{mn}^{<}R_{mn}^{>}e^{-2jh_{mn}(z_2-z_1)}e^{jh_{mn}|(z_{0i}-z_{0j})-(L_i-L_j)/2|} \\
&\quad \cdot\left[1-(-1)^p e^{\mp jh_{mn}L_i}\right]\left[1-(-1)^q e^{\pm jh_{mn}L_j}\right] \qquad z_{0i} \gtrless z_{0j} &(24)
\end{aligned}$$

While the summation in (14) can be evaluated without any difficulty when $i \neq j$, its evaluation when $i = j$ involves a slowly converging series given by

$$S(m) = \sum_{n=0}^{\infty} B(m,n)I_{z0}^{ii} = S_1(m) + S_2(m) \tag{25}$$

where

$$S_1(m) = \sum_{n=0}^{\infty} B(m,n)C(m,n)\left[1+(-1)^{p+q}\right]\left[1-(-1)^p e^{-jh_{mn}L_i}\right] \tag{26}$$

$$S_2(m) = \sum_{n=0}^{\infty} B(m,n)\delta_{pq}\frac{(k^2-\alpha_{pi}^2)L_i}{\alpha_{pi}^2 - h_{mn}^2}. \tag{27}$$

To show this, let us examine the asymptotic behavior of the series when $n \to \infty$. Using the asymptotic expression of the Bessel functions for large arguments, we obtain the approximate solution to the eigenvalue equation $B_\nu'(\lambda_{mn}\rho_2) = 0$ as

$$\lambda_{mn} \sim \frac{n\pi}{\rho_2 - \rho_1} \tag{28}$$

and hence

$$jh_{mn} \;\sim\; \frac{n\pi}{\rho_2 - \rho_1} \tag{29}$$

$$B(m,\infty) \;\sim\; \frac{1}{1+\delta_{0m}} \frac{2}{k^2(\rho_2-\rho_1)\rho_2\phi_0}. \tag{30}$$

Clearly, the asymptotic form of the terms in $S_1(m)$ is proportional to n^{-3} and that in $S_2(m)$ is proportional to n^{-2}. To accelerate the convergence of $S_2(m)$, we apply the Kummer transform [26] to (27), resulting in

$$\begin{aligned} S_2(m) &= \delta_{pq}(k^2 - \alpha_{pi}^2)L_i\left\{\sum_{m=0}^{\infty}\left[\frac{B(m,n)}{\alpha_{pi}^2 - h_{mn}^2} - \left(\frac{\rho_2 - \rho_1}{\pi}\right)^2 \frac{B(m,\infty)}{n^2 + x^2}\right]\right. \\ &\quad \left. + \left(\frac{\rho_2 - \rho_1}{\pi}\right)^2 B(m,\infty)\sum_{m=0}^{\infty}\frac{1}{n^2 + x^2}\right\} \end{aligned} \tag{31}$$

where

$$x^2 = \left(\frac{\rho_2 - \rho_1}{\pi}\right)^2 \left\{\alpha_{pi}^2 - k^2 - \left[\frac{2m\pi}{(\rho_2 - \rho_1)\,\phi_0}\right]^2\right\}. \tag{32}$$

The first summation in (31) converges rapidly and the second summation in (31) can be written in a closed form as

$$\sum_{n=0}^{\infty}\frac{1}{n^2 + x^2} = \begin{cases} \frac{1}{2x}\left[\frac{1}{x} + \pi\coth\pi x\right] & x > 0 \\ \frac{-1}{2|x|}\left[\frac{1}{|x|} + \pi\cot\pi|x|\right] & x < 0 \end{cases} \tag{33}$$

In passing, we note that when ρ_1 and $\rho_2 \to \infty$, the expressions for sectoral waveguides reduce to those for the corresponding rectangular waveguides with the following substitutions

$$\frac{\rho_2}{\nu} = \frac{a}{m\pi} \tag{34}$$

$$\lambda_{mn}^2 = \left(\frac{m\pi}{a}\right)^2 + \left(\frac{n\pi}{b}\right)^2 \tag{35}$$

$$B(m,n) = \frac{2}{1 + \delta_{0m}}\frac{1}{k^2 ab} \tag{36}$$

where $a = \rho_1\Delta\phi$ or $\rho_2\Delta\phi$ and $b = \rho_2 - \rho_1$ are the dimension of the rectangular waveguide.

C. Generalized Admittance Matrix Elements for Region b

The admittance matrix elements due to the external coupling in region b are given by

$$Y_{pq}^{ij}(b) = \iint_{S_i^I}\iint_{S_j^I} G_{zz}^b(\mathbf{r},\mathbf{r}')\sin\alpha_{pi}\xi\,\sin\alpha_{qj}\xi'\,dS\,dS' \tag{37}$$

where G_{zz}^b is the $\hat{z}\hat{z}$-component of the magnetic-source magnetic-field dyadic Green's function for the conducting cylinder. The rigorous expressions of the dyadic Green's function involve infinite series and infinite integrations of Hankel's functions [27], [28]. Although these expressions can be converted into the forms suitable to numerical calculation [28], it is still very time consuming to compute the matrix elements, especially when the cylinder is large. Therefore, it is necessary to seek the fast converging asymptotic solutions. Five different approximate asymptotic solutions have been developed in the past and these are denoted as PINY [29], UI [30], OSU [31], B-L [24], and TSB [25] solutions, and each has its accuracy and range of validity. A comparative study [28] shows that the B-L and TSB solutions offer the best overall accuracy, and these two solutions are complementary to each other. More specifically, the B-L solution is more accurate when the field point is near the source or in the paraxial region while the TSB solution is better when the field point is far from the source and off axis.

The B-L solution [24] is given by

$$\begin{aligned} G^b_{zz} \sim G_0(t)\Big\{ & v(\tilde{\beta})\left[\cos^2\tilde{\theta} + \tilde{q}\,(1-\tilde{q})\,(2-3\cos^2\tilde{\theta})\right] \\ & - \tilde{q}\tilde{\beta}v'(\tilde{\beta})\left[\frac{11}{12}\cos^2\tilde{\theta} + \tilde{q}\left(\frac{11}{6} + \frac{2}{3}\tan^2\tilde{\theta} - \frac{187}{64}\cos^2\tilde{\theta}\right)\right]\Big\} \end{aligned} \tag{38}$$

and the TSB solution [25] is given by

$$\begin{aligned} G^b_{zz} \sim G_0(t)\Big\{ & v(\tilde{\beta})\left[\cos^2\tilde{\theta} + \tilde{q}(1-\tilde{q})(2-3\cos^2\tilde{\theta})\right] - \tilde{q}\Big[v(\tilde{\beta})\left(\frac{31}{72}\sin^2\tilde{\theta} - \frac{5}{24}\right) \\ & + v_1(\tilde{\beta})\left(\frac{11}{60} - \frac{17}{36}\sin^2\tilde{\theta}\right) + v_2(\tilde{\beta})\left(\frac{1}{24}\sin^2\tilde{\theta} + \frac{1}{40}\right) + \frac{j\tilde{\beta}}{5}v_0^{(1)}(\beta)\Big]\Big\} \end{aligned} \tag{39}$$

where $t = \sqrt{(z-z')^2 - (\varphi-\varphi')^2}$, $\tilde{\theta} = \arctan[(z-z')/(\varphi-\varphi')]$, $\tilde{q} = j/kt$, $\tilde{\beta} = (k\cos^4\tilde{\theta}/2R^2)^{1/3}t$, and v, v_1, v_2, and $v_0^{(1)}$ are the surface Fock functions, all defined in [24], [25], and Appendix C.

When $i = j$, G^b_{zz} has a t^{-3} singularity as $t \to 0$, and a regularization is needed to evaluate the integrals in (37). To do this, we first rewrite (38) as [25], [30]

$$G^b_{zz} = G^0_{zz} + \tilde{G}_{zz} \tag{40}$$

where

$$G^0_{zz} = G_0(t)\left[\cos^2\tilde{\theta} + \tilde{q}\,(1-\tilde{q})\,(2-3\cos^2\tilde{\theta})\right] \tag{41}$$

$$\begin{aligned} \tilde{G}_{zz} = G_0(t)\Big\{ & \left[v(\tilde{\beta})-1\right]\left[\cos^2\tilde{\theta} + \tilde{q}\,(1-\tilde{q})\,(2-3\cos^2\tilde{\theta})\right] \\ & - \tilde{q}\tilde{\beta}v'\left(\tilde{\beta}\right)\left[\frac{11}{12}\cos^2\tilde{\theta} + \tilde{q}\left(\frac{11}{6} + \frac{2}{3}\tan^2\tilde{\theta} - \frac{187}{64}\cos^2\tilde{\theta}\right)\right]\Big\}. \end{aligned} \tag{42}$$

It can be shown that G^0_{zz} is the $\hat{z}\hat{z}$-component of the dyadic Green's function for an infinite conducting ground plane, given by

$$G^0_{zz} = \frac{k^2}{j\omega\mu}\left(1 + \frac{1}{k^2}\frac{\partial^2}{\partial z^2}\right)\frac{e^{-jkt}}{2\pi t} \tag{43}$$

whereas $\widetilde{G}_{zz}$ can be considered as the perturbation due to the curvature of the cylinder, with a singularity of $t^{-3/2}$ as $t \to 0$. As a result, the self-admittance matrix element can be written as

$$Y^{ii}_{pq}(b) = Y^{0ii}_{pq}(b) + \widetilde{Y}^{ii}_{pq}(b). \tag{44}$$

Using integration of part and transformation of variables, $Y^{0ii}_{pq}(b)$ can be written as [8]

$$Y^{0ii}_{pq}(b) = \frac{k^2}{j\omega\mu}\frac{1+(-1)^{p+q}}{2\pi k^2}\int_0^{L_i}\int_0^{2w}\frac{e^{-jkt}}{t}F(u,v)\,dv\,du \tag{45}$$

where $t = \sqrt{u^2+v^2}$ and

$$F(u,v) = \begin{cases} \frac{2(2w-v)}{\alpha^2_{pi}-\alpha^2_{qi}}\left[\alpha_{pi}(k^2-\alpha^2_{qi})\sin\alpha_{qi}u - \alpha_{qi}(k^2-\alpha^2_{pi})\sin\alpha_{pi}u\right] \\ \qquad\qquad\qquad\qquad\qquad\qquad\qquad\qquad p \neq q \\ (2w-v)\left[(L_i-u)(k^2-\alpha^2_{pi})\cos\alpha_{pi}u + \frac{1}{\alpha_{pi}}(k^2+\alpha^2_{pi})\sin\alpha_{pi}u\right] \\ \qquad\qquad\qquad\qquad\qquad\qquad\qquad\qquad p = q. \end{cases} \tag{46}$$

The integral in (45) becomes regular when evaluated in the polar coordinates.

To evaluate the perturbation term in (44), we first let $\eta = R\varphi$, $\eta' = R\varphi'$, where $R = \rho_3$, and write it as

$$\widetilde{Y}^{ii}_{pq}(b) = \int_0^{L_i}\int_{-w}^{w}\int_0^{L_i}\int_{-w}^{w}\widetilde{G}_{zz}(\xi-\xi',\eta-\eta')\,\sin\alpha_{pi}\xi\,\sin\alpha_{qi}\xi'\,d\eta'\,d\xi'\,d\eta\,d\xi. \tag{47}$$

Introducing the transformations $u = \xi - \xi'$, $v = \eta - \eta'$, $u' = \xi + \xi' - L_i$, and $v' = \eta + \eta'$, and observing that $\widetilde{G}_{zz}(u,v)$ is an even function of u and v, we obtain

$$\widetilde{Y}^{ii}_{pq}(b) = \left[1+(-1)^{p+q}\right]\int_0^{L_i}\int_0^{w}(2w-v)\widetilde{G}_{zz}(u,v)\widetilde{F}(u)\,dv\,du \tag{48}$$

where

$$\widetilde{F}(u) = \begin{cases} \frac{2}{\alpha^2_{pi}-\alpha^2_{qi}}\left[(-1)^{p+q}\alpha_{pi}\sin\alpha_{qi}u - \alpha_{qi}\sin\alpha_{pi}u\right] & p \neq q \\ (L_i-u)\cos\alpha_{pi}u + \frac{1}{\alpha_{pi}}\sin\alpha_{pi}u & p = q. \end{cases} \tag{49}$$

With another transformation $u = t\cos\theta$, and $v = t\sin\theta$, (48) becomes

$$\widetilde{Y}^{ii}_{pq}(b) = \left[1 + (-1)^{p+q}\right]\left\{ \int_0^{\theta_0}\int_0^{L_i/\cos\theta} + \int_{\theta_0}^{\pi/2}\int_0^{2w/\sin\theta} \right\} \cdot(2w - t\sin\theta)\,\widetilde{G}_{zz}(t,\theta)\,\widetilde{F}(t,\theta)\,t\,d\theta\,dt \tag{50}$$

where $\theta_0 = \tan^{-1}(2w/L_i)$ and $\widetilde{G}_{zz}(t,\theta)$ has the same form as (42). The integrals in (50) become regular by letting $t = r^2$, which can be evaluated by expanding the integrand in terms of the power of r and using Gaussian quadrature. The Fock function can evaluated using its small-argument expansions.

When $i \neq j$, the expression for the admittance matrix elements can be written as

$$Y^{ij}_{pq}(b) = \int_0^{L_i}\int_{-w}^{w}\int_0^{L_j}\int_{-w}^{w} G_{zz}(z - z', R(\varphi - \varphi'))\,\sin\alpha_{pi}\xi\,\sin\alpha_{qi}\xi'\;d\eta'\,d\xi'\,d\eta\,d\xi \tag{51}$$

using the coordinate transformation

$$\begin{aligned} z - z' &= (\xi - \xi') + (z_{0i} - z_{0j}) + (L_i - L_j)/2 \\ R(\varphi - \varphi') &= (\eta - \eta') + R(\varphi_{0i} - \varphi_{0j}) \end{aligned} \tag{52}$$

where φ_{0i} and φ_{0j} are the coordinates of the center of the ith and jth slot, respectively.

In practical slot arrays, the length difference between the slots is small. In this case, we can use the average slot length of the two slots to approximate their length, that is,

$$L_i \approx L_j \approx (L_i + L_j)/2 \equiv L. \tag{53}$$

Using the transformations $u = \xi - \xi'$ and $u' = \xi + \xi' - L$, and the midpoint integration, we obtain

$$Y^{ij}_{pq}(b) = 2w^2\int_0^L \left[G_{zz}(u) + (-1)^{p+q}G_{zz}(-u)\right]\widetilde{F}(u)\,du \tag{54}$$

where $\widetilde{F}(u)$ is given by (49) by replacing L_i with L, and $G_{zz}(u)$ is given by (38) and (39) with the transformations $z - z' = u + (z_{0i} - z_{0j})$ and $R(\varphi - \varphi') = R(\varphi_{0i} - \varphi_{0j})$.

In passing, we note that in this work, the TSB asymptotic solution is used for two distant slots whose centers have the same z-coordinate, whereas the B-L asymptotic solution is employed for all other cases. We also note that the asymptotic solution of the surface fields on a cylinder can be interpreted as the creeping waves propagating from the source to the field point along the surface of cylinder. In general, there are at least two creeping waves. However, for an open cylindrical surface, only the shortest one has to be considered.

D. Generalized Admittance Matrix Elements for Region c

It can be shown (Appendix B) that the magnetic field in the cavity (region c with a sectoral cross-section), formed by the slot with its two apertures covered by a perfectly conducting surface, due to the surface magnetic current $\hat{z}\delta(\rho - \rho')\sin\alpha_{pi}\xi$ is given by

$$H_z(\rho,\rho') = \frac{\beta^2}{j\omega\mu} R(\rho,\rho') \sin\alpha_{pi}\xi \tag{55}$$

where $\beta^2 = |k^2 - \alpha_{pi}^2|$ and

$$R(\rho,\rho') = \begin{cases} C\, B(\rho_2,\rho)\, B(\rho_3,\rho') & \rho < \rho' \\ C\, B(\rho_3,\rho)\, B(\rho_3,\rho') & \rho > \rho' \end{cases} \tag{56}$$

with

$$C = (1/\beta)\left[B(\rho_2,\rho')B'(\rho_3,\rho') - B(\rho_3,\rho')B'(\rho_2,\rho')\right]^{-1} \tag{57}$$

$$B(\rho',\rho) = \begin{cases} J_0'(\beta\rho')Y_0(\beta\rho) - Y_0'(\beta\rho')J_0(\beta\rho) & k > \alpha_{pi} \\ I_0'(\beta\rho')K_0(\beta\rho) - K_0'(\beta\rho')I_0(\beta\rho) & k < \alpha_{pi}. \end{cases} \tag{58}$$

It is easy to see that

$$B'(\rho_2,\rho_2) = B'(\rho_3,\rho_3) = 0 \tag{59}$$

$$B(\rho_2,\, \rho_2) = \frac{1}{\beta\rho_2}, \qquad B(\rho_3,\, \rho_3) = \frac{1}{\beta\rho_3} \tag{60}$$

Using (55), we obtain the expressions for the generalized admittance matrix elements for region c as

$$Y_{pq}^{ij}(c,S_i^I;S_j^I) = \frac{L_i w\beta}{j\omega\mu}\frac{B(\rho_3,\rho_2)}{B'(\rho_3,\rho_2)}\delta_{ij}\delta_{pq} \tag{61}$$

$$Y_{pq}^{ij}(c,S_i^I;S_j^{II}) = \frac{L_i w\beta}{j\omega\mu}\frac{-1}{\beta\rho_2 B'(\rho_2,\rho_3)}\delta_{ij}\delta_{pq} \tag{62}$$

$$Y_{pq}^{ij}(c,S_i^{II};S_j^I) = \frac{L_i w\beta}{j\omega\mu}\frac{1}{\beta\rho_3 B'(\rho_3,\rho_2)}\delta_{ij}\delta_{pq} \tag{63}$$

$$Y_{pq}^{ij}(c,S_i^{II};S_j^{II}) = \frac{L_i w\beta}{j\omega\mu}\frac{-B(\rho_2,\rho_3)}{B'(\rho_2,\rho_3)}\delta_{ij}\delta_{pq}. \tag{64}$$

When ρ_2 and $\rho_3 \to \infty$, the expressions above reduce to those for a rectangular cavity as

$$Y_{pq}^{ij}(c,S_i^I;S_j^I) = Y_{pq}^{ij}(c,S_i^{II};S_j^{II}) = \frac{L_i w\beta}{j\omega\mu}\cot\beta t\, \delta_{ij}\delta_{pq} \tag{65}$$

$$Y_{pq}^{ij}(c,S_i^I;S_j^{II}) = Y_{pq}^{ij}(c,S_i^{II};S_j^I) = \frac{L_i w\beta}{j\omega\mu}\frac{-1}{\sin\beta t}\delta_{ij}\delta_{pq} \tag{66}$$

for $k > \alpha_{pi}$, and

$$Y_{pq}^{ij}(c, S_i^{I}; S_j^{I}) = Y_{pq}^{ij}(c, S_i^{II}; S_j^{II}) \;=\; \frac{L_i w\beta}{j\omega\mu}\coth \beta t\, \delta_{ij}\delta_{pq} \tag{67}$$

$$Y_{pq}^{ij}(c, S_i^{I}; S_j^{II}) = Y_{pq}^{ij}(c, S_i^{II}; S_j^{I}) \;=\; \frac{L_i w\beta}{j\omega\mu}\frac{-1}{\sinh \beta t}\, \delta_{ij}\delta_{pq} \tag{68}$$

for $k < \alpha_{pi}$.

E. Excitation Vector

Consider an incident plane wave of arbitrary polarization and incident angle, whose electric field is given by

$$\mathbf{E}^{inc} = (\hat{\theta}^{inc}\cos\psi + \hat{\varphi}^{inc}\sin\psi)e^{-jk\hat{\mathbf{r}}^{inc}\cdot\mathbf{r}} \tag{69}$$

where ψ is the polarization angle, $(\theta^{inc}, \varphi^{inc})$ denote the incident angles, and $(\hat{\mathbf{r}}^{inc}, \hat{\theta}^{inc}, \hat{\varphi}^{inc})$ are the unit vectors. In the computation of the excitation vector, the primary field, $\mathbf{H}^{pri}$ in (2), is the sum of the incident field and the field scattered by the cylinder in the absence of all the slots. This field is given by

$$H_z^{pri}\Big|_{\rho=\rho_3} = -Y_0 \sin\psi \sin\theta^{inc}\, e^{jkz\cos\theta^{inc}} M(k\rho_3 \sin\theta^{inc}, \varphi - \varphi^{inc}) \tag{70}$$

where

$$M(x,\varphi) = \frac{2}{j\pi x}\sum_{n=0}^{\infty}\frac{2}{1+\delta_{0n}}\frac{j^n \cos n\varphi}{H_n^{(2)'}(x)}. \tag{71}$$

From (70) we obtain the elements of the excitation vector as

$$\begin{aligned} I_{pi} \;&=\; \iint_{S_i^{I}} H_z^{pri}\Big|_{\rho=\rho_3} \sin\alpha_{pi}\xi \; dS \\ &=\; 4Y_0 \frac{\Delta\varphi L_i}{p\pi}\sin\psi\, \sin\theta^{inc}\, e^{jkz_{0i}\cos\theta^{inc}} f_p(\theta^{inc}) \\ &\qquad \cdot\widetilde{M}(k\rho_3 \sin\theta^{inc}, \varphi_{0i} - \varphi^{inc}, \Delta\varphi) \end{aligned} \tag{72}$$

where

$$f_p(\theta) = \left[1 - \left(\frac{kL_i}{p\pi}\cos\theta\right)^2\right]^{-1} \begin{cases} -\cos\left(\frac{kL_i}{2}\cos\theta\right) & p = \text{odd} \\ j\sin\left(\frac{kL_i}{2}\cos\theta\right) & p = \text{even} \end{cases} \tag{73}$$

$$\widetilde{M}(x,\varphi,\Delta\varphi) = \frac{2}{j\pi x}\sum_{n=0}^{\infty}\frac{2}{1+\delta_{0n}}\frac{j^n\cos n\varphi}{H_n^{(2)'}(x)}\,\mathrm{Sam}(n\,\Delta\varphi) \tag{74}$$

in which $\Delta\varphi = w/\rho_3$, and $\mathrm{Sam}(x)$ is a sampling function defined as

$$\mathrm{Sam}(x) = \begin{cases} 1 & x = 0 \\ \sin x/x & x \neq 0. \end{cases} \tag{75}$$

For narrow slots, we can use the midpoint integration to find

$$I_{pi} = 4Y_0 \frac{\Delta\varphi\, L_i}{p\pi} \sin\psi \sin\theta^{inc} e^{jkz_{0i}\cos\theta^{inc}} f_p(\theta^{inc}) M(k\rho_3 \sin\theta^{inc}, \varphi_{0i} - \varphi^{inc}). \tag{76}$$

When x becomes large, $M(x,\varphi)$ for the lit region can be evaluated more efficiently using the expression [27]

$$M(x,\varphi) \cong 2e^{jx\cos\varphi} \tag{77}$$

which can be considered as the geometrical optics approximation. Note that (77) has the same accuracy as Gorianiov' more complicated expression [32]. For the neighborhood of the shadow boundary and the shadow region, $M(x,\varphi)$ can be evaluated using the expression obtained using the Watson transformation and Fock theory [27],

$$\begin{aligned} M(x,\varphi) \sim\ & e^{-jx(\varphi-\frac{\pi}{2})} g\left[\left(\varphi - \frac{\pi}{2}\right)\left(\frac{x}{2}\right)^{1/3}\right] \\ & + e^{-jx(\frac{3\pi}{2}-\varphi)} g\left[\left(\frac{3\pi}{2} - \varphi\right)\left(\frac{x}{2}\right)^{1/3}\right] \end{aligned} \tag{78}$$

where $g(x)$ is the far-zone Fock function, whose definition is given in [27], [33], [34] and Appendix C.

F. Scattered Field and RCS

Once the equivalent magnetic currents on the slot apertures are found, we can compute the scattered field, which can be considered as the radiated field due to the equivalent magnetic currents. Using the Fourier transform and far-field approximation [35], it can be shown that the field radiated by $\mathbf{M}_i^{II}$ is

$$E_\theta = 0 \tag{79}$$

$$E_\varphi = \frac{jkwL_i}{2\pi^2} \frac{e^{-jkr_i}}{r} \sin\theta\, \widetilde{M}\left(k\rho_3 \sin\theta, \varphi_{0i} - \varphi, \Delta\varphi\right) \sum_{p=1}^{N_i^{II}} \frac{V_i^{II}}{p} f_p^*(\theta) \tag{80}$$

where $r_i = r - z_{0i}\cos\theta$. For a narrow slot on a large cylinder, we can again use the approximation described in preceding subsection to simplify the far-field calculation.

The RCS of the slot array is defined as

$$\sigma = \lim_{r \to \infty} 4\pi r^2 \left| \frac{\mathbf{E}^{sca}(\mathbf{r})}{\mathbf{E}^{inc}(\mathbf{r})} \right|^2 \tag{81}$$

where $\mathbf{E}^{sca}$ is the total scattered field from the slot array.

III. NUMERICAL RESULTS

The formulation described above has been implemented in a computer program and a variety of numerical results have been obtained to study the effects of various factors on RCS. Because of limited space, we present only some typical results.

For all the examples considered, the cross-section of sectoral waveguides is given by $\frac{1}{2}(\rho_1 + \rho_2)\Delta\phi = 21$ mm and $\rho_2 - \rho_1 = 10.16$ mm. The distance between the center-lines of the adjacent waveguides is 22 mm, measured on the surface of the cylinder. The adjacent slots on the same waveguide are spaced $\lambda_{g0}/2$ apart in the z direction, where λ_{g0} is the waveguide wavelength at the working frequency. The shorted planes are placed $\lambda_{g0}/4$ away from the first and last slots, respectively. In order to avoid the numerical overflow in the computation of the generalized admittance elements for the shorted waveguides at the working frequency, the position of the shorted planes is displaced by Δz, which can be considered as an acceptable manufacturing tolerance. All other parameters, unless otherwise specified, are given by: $2w = 1.6$ mm, $L_i = 1.6$ mm, $\delta_i = 1.5$ mm, $\Delta t = 0.8$ mm, $\Delta z = 0.01$ mm, $\psi = 90^0$, and the working frequency $f_0 = 9.1$ GHz. The normal at the center of the array is $\theta = 90^0$ and $\phi = 0^0$ in the spherical coordinate system.

The computer program was first validated by comparing its solution to those obtained by MoM and FEM [23] for a single slot on a planar surface. Good agreement was observed between the three solutions.

To demonstrate the effect of the curvature of the host cylinder on the RCS of a conformal slot array, Figs. 3 to 6 show the RCS for $\rho_1 = \infty$, $\rho_1 = 500$ cm, $\rho_1 = 200$ cm, $\rho_1 = 100$ cm, and $\rho_1 = 50$ cm in both E- and H-planes. As can be seen, the cylinder's curvature has a significant effect on the patterns and values of the RCS in the E-plane. When ρ_1 becomes large, the RCS approaches that for a planar array. When ρ_1 decreases, the grating lobes begin to disappear and the maximum RCS decreases. In contrast, the pattern of the RCS in the H-plane remains the same and only the value of the RCS is decreased as ρ_1 decreases.

To further demonstrate the effect of the cylinder's curvature on the RCS, Fig. 7 presents the space distribution of the RCS for $\rho_1 = \infty$, $\rho_1 = 200$ cm, $\rho_1 = 100$ cm, and $\rho_1 = 30$ cm. As can be seen clearly, as ρ_1 decreases the grating lobes in the E-plane is dilated where the pattern in the H-plane remains the same.

To show the effect of the waveguide terminals on the RCS, Fig. 8 gives the RCS of a 8×8 conformal slot array ($\rho_1 = 100$ cm) when the waveguide terminals are matched and shorted. It can be seen that when the plane wave is incident normally on the cylinder ($\theta = 90°$), the RCS is very small for the array with shorted terminals. This is because at the working frequency, the wave entered the waveguide is reflected by the shorted terminals and the reflected wave cancels the incident wave at the slot. Thus, the total electric field or the total equivalent magnetic current is zero at the aperture of the slot. An alternative explanation is that with the shorted terminals, the equivalent impedance looking at the aperture of the slots is zero. Therefore, when the shorted planes are displaced, the equivalent impedance will be changed and so is the RCS. This is clearly demonstrated in Fig. 9.

Figure 10 shows the effect of the slot thickness on the RCS. As can be seen, at the working frequency, the slot thickness has no effect on the RCS when the waveguides are matched and when the waveguides are shorted, it has a significant effect. This effect can also be explained using the concept of the equivalent impedance.

Finally, Fig. 11 shows the frequency responses of a 8×8 array ($\rho_1 = 100$ cm) with matched and shorted terminals, respectively. It is very interesting to note that the RCS of the slot array is almost identical no matter the waveguides are matched or shorted when the frequency is not close to the working frequency. At the working frequency, the RCS is substantially different. This implies that when the frequency of the incident wave is not close to the working frequency of the slot array, the energy entering the waveguides is very trivial and the main contribution to the RCS is the wave scattered by the slots directly. Therefore, in this case the dominant factor is the geometry of the slots, instead of the structures behind the slots. Figure 12 shows the space distribution of the RCS of a 16×16 array ($\rho_1 = 100$ cm) at three different frequencies.

IV. CONCLUSION

In this paper, a method of moments (MoM) solution was developed for electromagnetic scattering by a cylindrically conformal waveguide-fed slot array.

The equivalence principle was first employed to formulate the problem in terms of integral equations. Various dyadic Green's functions required in the formulation were derived and the integral equations were solved using the MoM in conjunction with global sinusoidal basis functions and Galerkin's testing procedure. The MoM solution requires the evaluation of the generalized admittance matrices involving some slowly-converging series. The slow convergence of the series associated with the summation of waveguide modes was accelerated using the Kummer transformation and the slow convergence of the series associated with the summation of the exterior modes was avoided by using the asymptotic solutions with proper treatment for singular integrals. The evaluation of the excitation vector and scattered field was also accelerated using Watson's transformation and asymptotic solutions. Numerical results were presented to illustrate the scattering characteristics of the cylindrically conformal waveguide-fed slot arrays, such as the effects of curvature, slot thickness, and waveguide termination on the radar cross section of the arrays. It was observed that (i) as the curvature of the host cylinder increases, the grating lobes in the E-plane dilate and eventually disappear and the maximum RCS is reduced; (ii) the internal structure of the waveguides such as the waveguide terminals has negligible effect on the RCS when the frequency of the incident wave is not close to the working frequency of the slot array; (iii) at the working frequency the RCS of the slot array with a shorted terminals at normal incidence changes significantly with the position of the shorted terminals; and (iv) at the working frequency the slot thickness has no effect on the RCS of the array with matched terminals whereas for the array with shorted terminals its effect is noticeable. The numerical method developed are useful in applications such as target identification, electromagnetic compatibility, EMP penetration, and stealth technology.

APPENDIX A

GREEN'S FUNCTION FOR SECTORAL WAVEGUIDES

For a sectoral waveguide, the magnetic-source magnetic-filed dyadic Green's function $\overline{\overline{G}}_H^{(m)}(\mathbf{r},\mathbf{r}')$ is related to the magnetic vector potential dyadic Green's function $\overline{\overline{g}}_m(\mathbf{r},\mathbf{r}')$ by

$$\overline{\overline{G}}_H^{(m)} = \frac{k^2}{j\omega\mu}\left(\overline{\overline{I}} + \frac{1}{k^2}\nabla\nabla\right)\cdot\overline{\overline{g}}_m \tag{82}$$

where $\overline{\overline{g}}_m$ satisfies the differential equation

$$(\nabla^2 + k^2)\overline{\overline{g}}_m = -\overline{\overline{I}}\delta\left(\mathbf{r}-\mathbf{r}'\right), \tag{83}$$

and boundary conditions

$$\hat{n} \cdot \overline{\overline{g}}_m \Big|_S = 0, \qquad \hat{n} \times \nabla \times \overline{\overline{g}}_m \Big|_S = 0. \tag{84}$$

In this work, we require only the zz-component, g_{mzz}, which satisfies the scalar wave equation

$$\left[\frac{1}{\rho}\frac{\partial}{\partial \rho}\left(\frac{\partial}{\partial \rho}\right) + \frac{1}{\rho^2}\frac{\partial^2}{\partial \varphi^2} + \frac{\partial^2}{\partial z^2} + k^2\right] g_{mzz} = -\frac{\delta(\rho-\rho')}{\rho}\delta(\varphi-\varphi')\delta(z-z'), \tag{85}$$

and boundary conditions

$$\frac{\partial g_{mzz}}{\partial \rho}\Big|_{\rho=\rho_1,\rho_2} = 0, \qquad \frac{\partial g_{mzz}}{\partial \varphi}\Big|_{\varphi=0,\Delta\phi} = 0. \tag{86}$$

Using the orthogonality relation [20]

$$\int_{\rho_1}^{\rho_2} \rho B_\nu(\lambda_{mn}\rho)\, B_\nu(\lambda_{mn'}\rho)\, d\rho = \delta_{nn'} N_{\lambda_{mn}}, \tag{87}$$

we can show that

$$\frac{\delta(\rho-\rho')}{\rho}\delta(\varphi-\varphi') = \sum_{m=0}^{\infty}\sum_{n=0}^{\infty} \frac{2}{1+\delta_{0m}}\frac{1}{\Delta\phi N_{\lambda_{mn}}} B_\nu(\lambda_{mn}\rho) B_\nu(\lambda_{mn}\rho') C_\varphi C_{\varphi'}. \tag{88}$$

Assuming that

$$g_{mzz} = \sum_{m=0}^{\infty}\sum_{n=0}^{\infty} \frac{2}{1+\delta_{0m}}\frac{1}{\Delta\phi N_{\lambda_{mn}}} B_\nu(\lambda_{mn}\rho)\, B_\nu(\lambda_{mn}\rho') C_\varphi C_{\varphi'} Z_{mn}(z,z') \tag{89}$$

and substituting into (85), we obtain

$$\left(\frac{d^2}{dz^2} + h_{mn}^2\right) Z_{mn}(z,z') = -\delta(z-z'). \tag{90}$$

Enforcing the boundary conditions at $z = z_1$ and z_2, which are specified in terms of the mode reflection coefficients, $R_{mn}^<$ and $R_{mn}^>$, respectively, we obtain

$$\begin{aligned} Z_{mn}(z,z') = \frac{1}{2jh_{mn}\Delta_{mn}} \Big[& e^{-jh_{mn}|z-z'|} - R_{mn}^< e^{j2h_{mn}z_1} e^{-jh_{mn}(z+z')} \\ & - R_{mn}^> e^{-2jh_{mn}z_2} e^{jh_{mn}(z+z')} + R_{mn}^< R_{mn}^> e^{-2jh_{mn}(z_2-z_1)} e^{jh_{mn}|z-z'|}\Big] \end{aligned} \tag{91}$$

The required zz-component $\overline{\overline{G}}_H^{(m)}$ can then be obtained from

$$G_{Hzz}^{(m)} = \frac{k^2}{j\omega\mu}\left(1 + \frac{1}{k^2}\frac{\partial^2}{\partial z^2}\right) g_{mzz} \tag{92}$$

with the aid of the differentiation formula for generalized functions

$$\frac{\partial^2}{\partial z^2} e^{-jh_{mn}|z-z'|} = \frac{\partial^2}{\partial z \partial z'} e^{-jh_{mn}|z-z'|} = 2jh_{mn}\delta(z-z') + h_{mn}^2 e^{-jh_{mn}|z-z'|}. \quad (93)$$

APPENDIX B
FIELD IN THE SLOT-CAVITY

The magnetic field in the slot-cavity, produced by the surface magnetic current $\hat{z}\delta(\rho - \rho') \sin \alpha_{pi}\xi$, is related to the magnetic vector potential by

$$H_z = \frac{k^2}{j\omega\mu}\left(1 + \frac{1}{k^2}\frac{\partial^2}{\partial \xi^2}\right) A_{mz} \quad (94)$$

where A_{mz} satisfies the wave equation

$$(\nabla^2 + k^2)A_{mz} = -\delta(\rho - \rho') \sin \alpha_{pi}\xi, \qquad \mathbf{r} \in V_c \quad (95)$$

and boundary conditions

$$\left.\frac{\partial A_{mz}}{\partial \rho}\right|_{\rho=\rho_2,\rho_3} = 0, \qquad \left.\frac{\partial A_{mz}}{\partial \varphi}\right|_{\varphi=\pm\Delta\varphi} = 0, \qquad A_{mz}\Big|_{\xi=0,L,} = 0. \quad (96)$$

Assuming $A_{mz}(\rho, \varphi, \xi) = R(\rho, \rho') \sin \alpha_{pi}\xi$, we obtain

$$\frac{1}{\rho}\frac{d}{d\rho}\left(\rho \frac{dR}{d\rho}\right) + (k^2 - \alpha_{pi}^2)R = -\delta(\rho - \rho'), \quad (97)$$

$$\left.\frac{dR}{d\rho}\right|_{\rho=\rho_2,\rho_3} = 0. \quad (98)$$

Equation (97) is recognized as the inhomogeneous Bessel's equation of order zero, whose solution is given by (55)-(58).

APPENDIX C
FOCK FUNCTIONS

In this appendix, we give the definition and related formulas of the Fock functions used in this paper.

C.1 The Surface Fock Functions

i) *Definition*: For a complex z and a real x,

$$v_n(x) = \frac{e^{j(n+1/2)\pi/2} x^{n+1/2}}{2\Gamma(n+1/2)} \int_{\Gamma_1} t^n \frac{w_2(t)}{w_2'(t)} e^{-jxt}\, dt, \qquad n = 0, 1, 2 \quad (99)$$

$$
\begin{aligned}
v_0^{(1)}(x) &= \frac{e^{j\pi/4}x^{1/2}}{2\sqrt{\pi}} \int_{\Gamma_1} \left[\frac{w_2(t)}{w_2'(t)}\right]^2 e^{-jxt}\, dt, && (100)\\
v(x) &\equiv v_0(x), && (101)\\
v'(x) &= \left[v(x) - v_1(x)\right]/2x, && (102)
\end{aligned}
$$

where

$$w_2(t) = \frac{1}{\sqrt{\pi}} \int_{\Gamma_2} \exp\left(tz - z^3/3\right)\, dz. \qquad (103)$$

The integration contour Γ_1 (or Γ_2) goes from ∞ to 0 along the line specified by ang $t = -2\pi/3$ (or $\operatorname{ang} z = 2\pi/3$) and from 0 to ∞ along the real axis.

ii) *Small-Argument Asymptotic Expansion*: For $x < 1$,

$$
\begin{aligned}
v_n(x) &= 1 + (-1)^n \sum_{m=1}^{10} b_m(n)(-jx)^{3m/2}, && (104)\\
v_0^{(1)}(x) &= \sqrt{\pi}e^{-j\pi/4}x^{1/2}\left[1 + \sum_{m=1}^{10} c_m(-jx)^{3m/2}\right], && (105)
\end{aligned}
$$

where the coefficients $b_m(0)$, $b_m(1)$, $b_m(2)$, and c_m are given [25].

iii) *Residue Series Asymptotic Expansion*: For $x > 1$,

$$
\begin{aligned}
v_n(x) &= \frac{\pi e^{j(n-1/2)\pi/2}x^{n+1/2}}{2\Gamma(n+1/2)} \sum_{m=1}^{20} (t_m')^{n-1} e^{-xt_m'}, && (106)\\
v_0^{(1)}(x) &= \sqrt{\pi}e^{j3\pi/4}x^{1/2} \sum_{m=1}^{20} (1 + jxt_m') \frac{e^{-xt_m'}}{{t_m'}^3}, && (107)
\end{aligned}
$$

where $t_m' = |\alpha_m'|\exp(-j\pi/3)$, and $-\alpha_m'$ are the zeros of derivative of Airy's function, $\mathrm{Ai}'(x)$.

C.2 The Far-Zone Fock Functions

i) *Definition*:

$$g(x) = \frac{1}{\sqrt{\pi}} \int_{\Gamma_1} \frac{1}{w_2'(t)} e^{-jxt}\, dt. \qquad (108)$$

ii) *Formulas*:

$$
\begin{aligned}
g(x) &= 2e^{-jx^3/3} && (x < -3)\\
&= \sum_{m=1}^{10} A_m e^{s_m x} && (-3 \le x \le -0.5)\\
&= 1.39937 + \sum_{m=1}^{6} \frac{d_m}{m!}(\kappa x)^m && (-0.5 < x \le 0.5)
\end{aligned}
$$

$$\begin{aligned} &= \sum_{m=1}^{20} \frac{e^{\alpha'_m \kappa x}}{\alpha'_m \mathrm{Ai}(-\alpha'_m)} && (0.5 < x \leq 4.0) \\ &= 1.835 e^{-(0.8823-j0.5094)x - jx^3/3} && (x > 4.0) \qquad (109) \end{aligned}$$

where $\kappa = \exp(-j5\pi/6)$, d_m, A_m and s_m are given in Table I.

Table 1

m	d_m	A_m	s_m
1	0.7473831	−0.3467540381D−13 −j0.2020905526D−12	−0.8253328597D+01 j0.1219314385D+02
2	−0.6862081	−0.1469465991D−08 −j0.2834631597D−08	−0.6157249604D+01 j0.9659289583D+01
3	−2.9495325	−0.3540987938D+00 j0.1274055399D+00	−0.4741573876D+00 j0.2711864904D+01
4	−3.4827075	0.2544176553D−05 −j0.1407419787D−05	−0.4474126917D+01 j0.7632294399D+01
5	8.9378967	−0.2312340815D−03 j0.4465889350D−03	−0.3001183618D+01 j0.5858670248D+01
6	56.1946214	0.1332955205D−01 −j0.2046671398D−01	−0.1673939722D+01 j0.4236757852D+01
7		0.1180944801D+01 j0.1164437839D+01	0.5728149621D+00 j0.1234148084D+01
8		0.7689249066D+00 −j0.1285238403D+01	0.1413116779D+01 −j0.3362910894D+00
9		−0.2105540865D+00 j0.1312640573D−01	0.2125953705D+01 −j0.2263304268D+01
10		0.1622892013D−02 −j0.1090163259D−02	0.3117637911D+01 −j0.5238642524D+01

References

[1] A. F. Stevenson, "The theory of slots in rectangular waveguides," *J. Appl. Phys.*, vol. 19, pp. 24-38, Jan. 1948.

[2] A. A. Oliner, "The impedance properties of narrow radiating slots in the broad face of rectangular waveguide," *IRE Trans. Antennas Propagat.*, vol. 5, pp. 4-20, Jan. 1957.

[3] T. Vu Khac and C. T. Carson, "Impedance properties of a longitudinal slot antenna in the broad face of rectangular waveguide," *IEEE Trans. Antennas Propagat.*, vol. 21, pp. 708-710, Sept. 1973.

[4] H. Y. Yee, "Impedance of a narrow longitudinal shunt slot in a slotted waveguide array," *IEEE Trans. Antennas Propagat.*, vol. 22, pp. 589-592, July 1974.

[5] R. W. Lyon and A. J. Sangster, "Efficient moment method analysis of radiating slots in thick-walled rectangular waveguide," *IEE Proc., Pt. H*, vol. 128, pp. 197-205, Aug. 1981.

[6] G. J. Stern and R. S. Elliott, "Resonant length of longitudinal slots and validity of circuit representation: Theory and experiment," *IEEE Trans. Antennas Propagat.*, vol. 33, pp. 1264-1271, Nov. 1985.

[7] L. G. Josefsson, "Analysis of a longitudinal slot in rectangular waveguide," *IEEE Trans. Antennas Propagat.*, vol. 35, pp. 1351-1357, Dec. 1987.

[8] K. Xia and Q.-J. Yang, "Study on characteristics of dielectric-covered waveguide slots," *Chinese J. Appl. Sci.*, vol. 7, no. 2, pp. 115-123, 1989.

[9] S. R. Rengarajan, "Compound radiating slots in a broad wall of a rectangular waveguide," *IEEE Trans. Antennas Propagat.*, vol. 37, pp. 1116-1123, Sept. 1989.

[10] P. B. Katehi, "Dielectric-covered waveguide longitudinal slots with finite wall thickness," *IEEE Trans. Antennas Propagat.*, vol. 38, pp. 1039-1045, July 1990.

[11] R. S. Elliott, "An improved design procedure for small array of shunt slots," *IEEE Trans. Antennas Propagat.*, vol. 31, pp. 48-53, Jan. 1983.

[12] A. J. Sangster and A. H. I. McCormick, "Theoretical design/synthesis of slotted waveguide arrays," *IEE Proc., Pt. H*, vol. 136, pp. 39-46, Feb. 1989.

[13] J. Zheng and Q.-J. Yang, "Dielectric-covered conformal slot array antenna on a large conducting cylinder," *Acta Electronica Sinica*, vol. 18, no. 1, pp. 57-63, 1990.

[14] J. J. Gulick and R. S. Elliott, "The design of linear and planar array of waveguide-fed longitudinal slots," *Electromagnetics*, vol. 10, pp. 327-347, Oct.-Dec. 1990.

[15] H. Y. Yee, "The design of large waveguide arrays of shunt slots," *IEEE Trans. Antennas Propagat.*, vol. 40, pp. 775-781, July 1992.

[16] S. R. Rengarajan and A. G. Derneryd, "Application of compound coupling slots in the design of shaped beam antenna patterns for array application," *IEEE Trans. Antennas Propagat.*, vol. 41, pp. 59-65, Jan. 1993.

[17] Q.-J. Yang and X. Tian, "Computer-aided-design of planar slot antennas," *Chinese J. Radio Sci.*, vol. 9, no. 1, pp. 1-11, 1994.

[18] K. Xia and Q.-J. Yang, "Study on the inclined slots in the narrow wall of a rectangular waveguide," *Acta Electronica Sinica*, vol. 20, no. 2, pp. 45-52, 1992.

[19] S. -W. Lue, Y. Zhang and S. -M. Cao, "The equivalent parameters for the radiating slot on a sectoral waveguide," *IEEE Trans. Antennas Propagat.*, vol. 42, pp. 1577-1581, Nov. 1994.

[20] G.-X. Fan, "Cylindrically conformal slotted-waveguide array antenna," Ph.D. dissertation, Tsinghua University, Beijing, China, Apr. 1995.

[21] L. G. Josefsson, "Slot coupling and scattering," *1990 IEEE Antennas Propagat. Int. Symp.*, pp. 942-945, Dallas, TX, June 1990.

[22] L. C. Trintinalia and H. Ling, "Electromagnetic scattering from 3-D arbitrary coated cavities via a connection scheme using triangular patches," *J. Electromag. Waves Appl.*, vol. 8, pp. 1411-1423, Nov. 1994.

[23] J. Chen and J.-M. Jin, "Electromagnetic scattering from slot antennas on waveguides with arbitrary terminations," *Microwave Opt. Tech. Lett.*, vol. 10, no. 5, pp. 286-291, Dec. 1995.

[24] J. Boersma and S. W. Lee, "Surface field due to a magnetic dipole on a cylinder: Asymptotic expansions of exact solution," Univ. of Illinois at Urbana-Champaign, Electromagnetics Lab. Rep. 78-17, 1978.

[25] T. S. Bird, "Accurate asymptotic solution for the surface field due to aperture in a conducting cylinder," *IEEE Trans. Antennas Propagat.*, vol. 33, pp. 1108-1117, Oct. 1985.

[26] M. Abramowitz and I. A. Stegun, *Handbook of Mathematical Functions.* New York: Dover Publications, 1965, ch. 3.

[27] J. R. Wait, *Electromagnetic Radiation from Cylindrical Structure.* New York: Pergamon, 1959.

[28] T. S. Bird, "Comparison of asymptotic solution for the surface field excited by a magnetic dipole on a cylinder, "*IEEE Trans. Antennas Propagat.*, vol. 32, pp. 1237-1244, Nov. 1984.

[29] Z. W. Chang, L. B. Felsen and A. Hessel, "Surface ray methods for mutual coupling in conformal arrays on cylinder and conical surface," Polytech Inst. New York, Final Rep., 1976 (prepared under Contract N00123-76-C-0236).

[30] S. W. Lee and S. Safavi-Naini, "Approximate asymptotic solution of surface field due to a magnetic dipole on a cylinder," *IEEE Trans. Antennas Propagat.*, vol. 26, pp. 593-597, July 1978.

[31] P. H. Pathak and N. Wang, "Ray analysis of mutual coupling between antennas on a convex surface," *IEEE Trans. Antennas Propagat.*, vol. 29, pp. 911-922, Nov. 1981.

[32] A. S. Goriainov, "An asymptotic solution of the problem of diffraction of a plane electromagnetic wave by a conducting cylinder," *Radio Eng. Electron.*, vol. 3, pp. 23-29, May 1958. (English translation. of *Radiotekh. i Elektron.*, vol. 3, pp. 603-614, 1958.)

[33] N. A. Logan, "General research in diffraction theory," vols. 1 and 2, LMSD-288087, LMSD-288088, Dec. 1959.

[34] V. A. Fock, *Electromagnetic Diffraction and Propagation Problems.* New York: Pergamon, 1965.

[35] R. F. Harrington, *Time-Harmonic Electromagnetic Fields.* New York: McGraw-Hill, 1961, pp. 245-250.

FIGURE CAPTIONS

Figure 1. Conformal slotted-waveguide array.

Figure 2. Division of three regions and surface magnetic currents.

Figure 3. The effect of the cylinder's curvature on the RCS in the E-plane for a 16 × 16 slot array with matched terminals at $f = 9.1$ GHz. (a)–·– planar, —— $\rho_1 = 500$ cm, (b) $\rho_1 = 200$ cm, (c) $\rho_1 = 100$ cm, (d) $\rho_1 = 50$ cm.

Figure 4. The effect of the cylinder's curvature on the RCS in the H-plane for a 16 × 16 slot array with matched terminals at $f = 9.1$ GHz. (a)–·– planar, —— $\rho_1 = 500$ cm, (b) $\rho_1 = 200$ cm, (c) $\rho_1 = 100$ cm, (d) $\rho_1 = 50$ cm.

Figure 5. The effect of the cylinder's curvature on the RCS in the E-plane for a 16 × 16 slot array with shorted terminals at $f = 9.1$ GHz. (a)–·– planar, —— $\rho_1 = 500$ cm, (b) $\rho_1 = 200$ cm, (c) $\rho_1 = 100$ cm, (d) $\rho_1 = 50$ cm.

Figure 6. The effect of the cylinder's curvature on the RCS in the H-plane for a 16 × 16 slot array with shorted terminals at $f = 9.1$ GHz. (a)–·– planar, —— $\rho_1 = 500$ cm, (b) $\rho_1 = 200$ cm, (c) $\rho_1 = 100$ cm, (d) $\rho_1 = 50$ cm.

Figure 7. RCS (dBsw) of a 16 × 16 slot array with shorted terminals at $f = 9.1$ GHz. (a) planar; (b) $\rho_1 = 200$ cm; (c) $\rho_1 = 100$ cm; (d) $\rho_1 = 30$ cm.

Figure 8. The effect of the terminals on the RCS of a 8 × 8 conformal slot array ($\rho_1 = 100$ cm). ··· matched terminals, —— shorted terminals. (a) E-plane pattern; (b) H-plane pattern.

Figure 9. The effect of the position of the shorted plane on the RCS of a 8 × 8 conformal slot array ($\rho_1 = 100$ cm). —— $\Delta z = 0.001$cm, ··· $\Delta z = 0.1$cm, –·– $\Delta z = 1$cm. (a) E-plane pattern; (b) H-plane pattern.

Figure 10. The effect of the slot thickness on the RCS of a 8 × 8 conformal slot array ($\rho_1 = 100$ cm) in the E-plane. —— $\Delta t = 1$ mm, ··· $\Delta t = 0.4$ mm, –·– $\Delta t = 0.1$ mm. (a) matched terminals; (b) shorted terminals.

Figure 11. RCS of a 8 × 8 conformal slot array ($\rho_1 = 50$ cm) as a function of frequency. (a) $\theta^{inc} = 90^0$, $\varphi^{inc} = 0^0$; (b) $\theta^{inc} = 90^0$, $\varphi^{inc} = 45^0$.

Figure 12. RCS (dBsw) of a 16 × 16 conformal slot array ($\rho_1 = 100$ cm) at three frequencies. (a) $f = 8$ GHz; (b) $f = 9.1$ GHz; (c) $f = 12$ GHz.

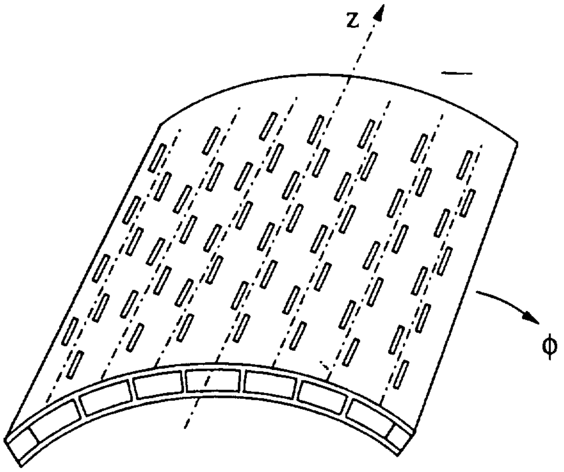

Fig. 1

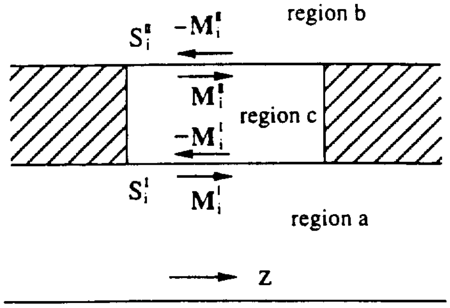

Fig. 2

Figure 1: Conformal slotted-waveguide array.

Figure 2: Division of three regions and surface magnetic currents.

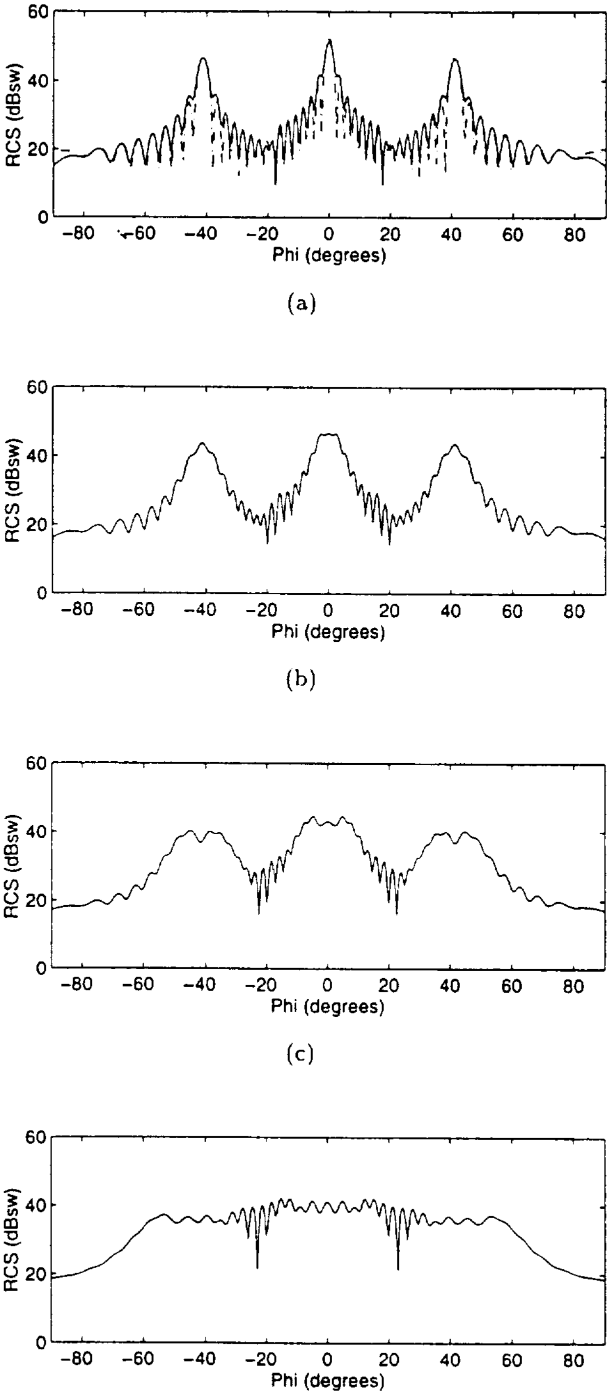

(a)

(b)

(c)

(d)

Figure 3: The effect of the cylinder's curvature on the RCS in the E-plane for a 16 × 16 slot array with matched terminals at $f = 9.1$ GHz. (a)$- \cdot -$ planar, —— $\rho_1 = 500$ cm, (b) $\rho_1 = 200$ cm, (c) $\rho_1 = 100$ cm, (d) $\rho_1 = 50$ cm.

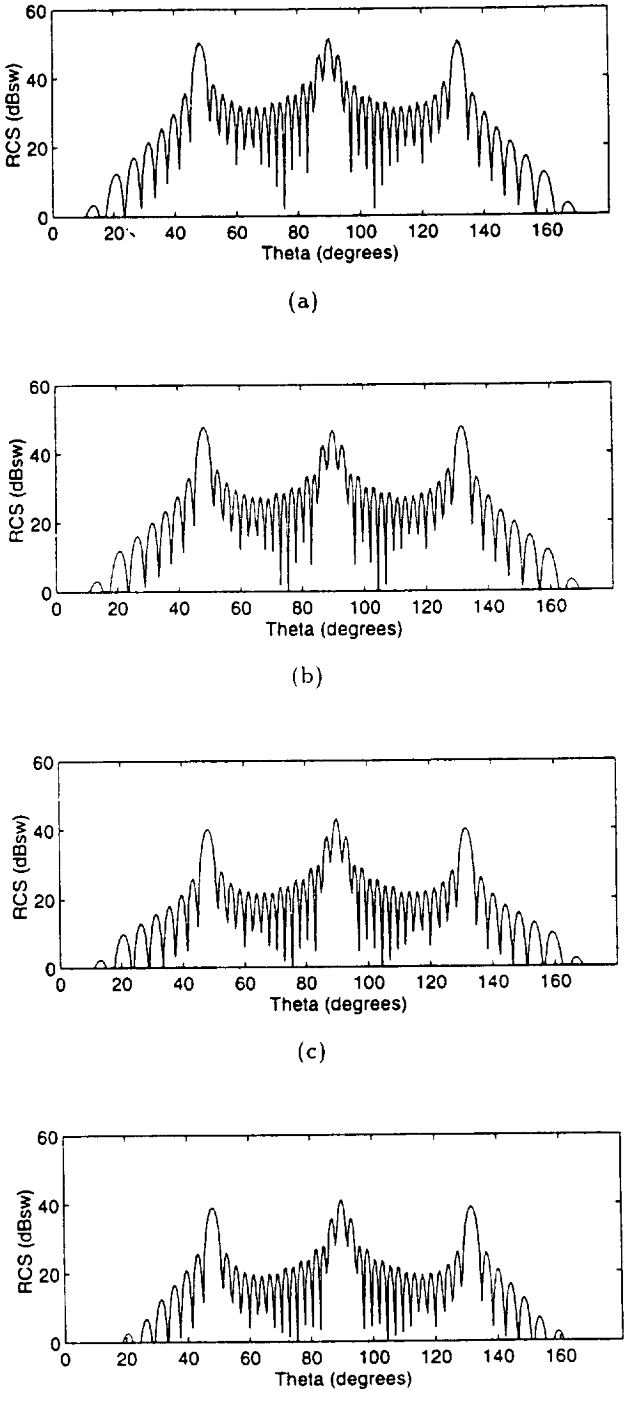

(a)

(b)

(c)

(d)

Figure 4: The effect of the cylinder's curvature on the RCS in the H-plane for a 16 × 16 slot array with matched terminals at $f = 9.1$ GHz. (a)—·— planar, —— $\rho_1 = 500$ cm, (b) $\rho_1 = 200$ cm, (c) $\rho_1 = 100$ cm, (d) $\rho_1 = 50$ cm.

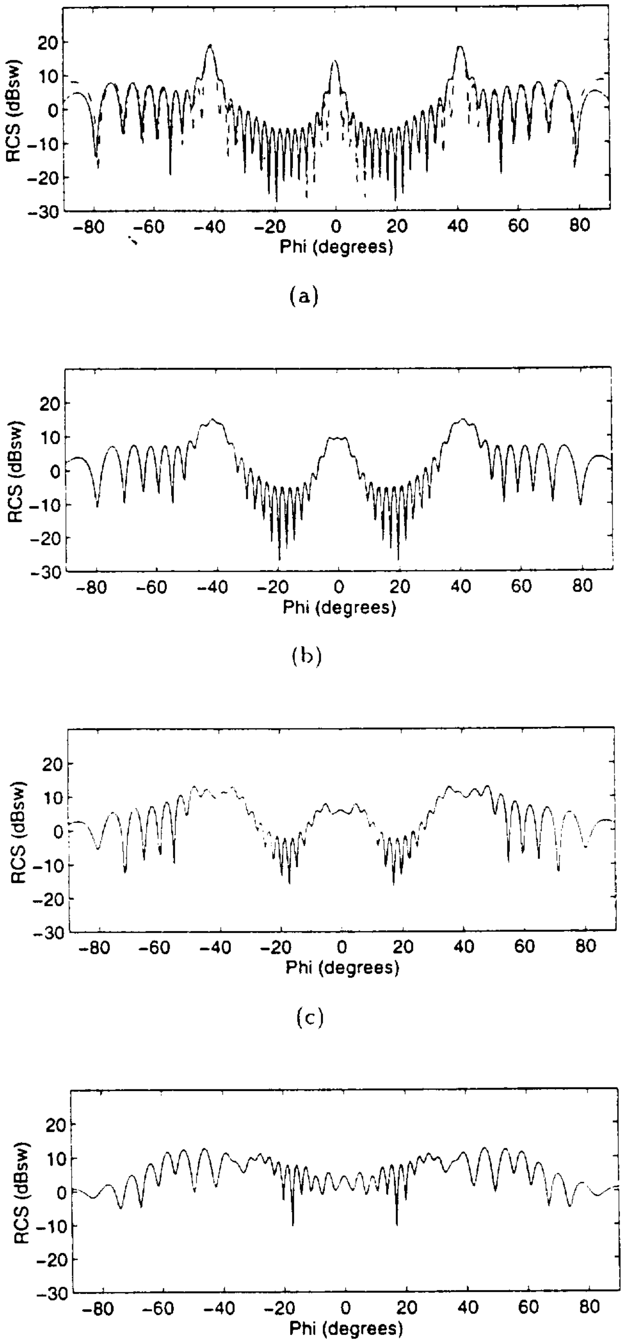

(a)

(b)

(c)

(d)

Figure 5: The effect of the cylinder's curvature on the RCS in the E-plane for a 16 × 16 slot array with shorted terminals at $f = 9.1$ GHz. (a)$- \cdot -$ planar, —— $\rho_1 = 500$ cm, (b) $\rho_1 = 200$ cm, (c) $\rho_1 = 100$ cm, (d) $\rho_1 = 50$ cm.

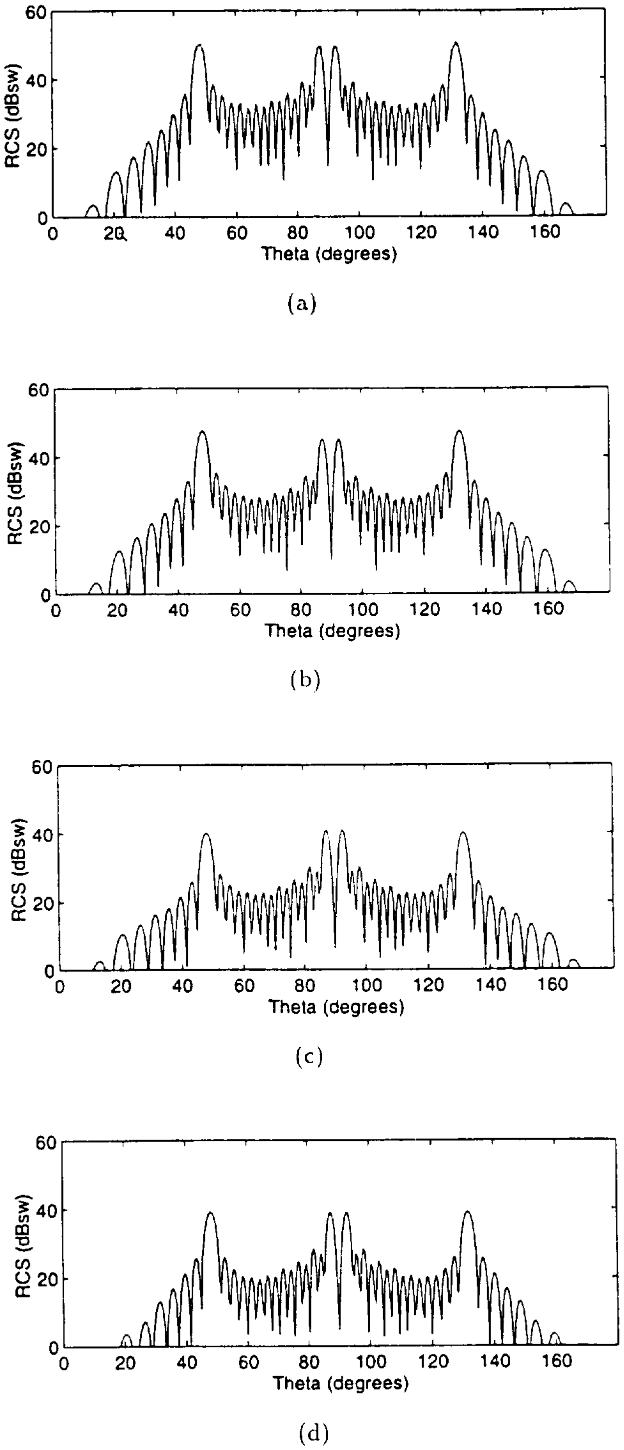

(a)

(b)

(c)

(d)

Figure 6: The effect of the cylinder's curvature on the RCS in the H-plane for a 16 × 16 slot array with shorted terminals at $f = 9.1$ GHz. (a)—·— planar, —— $\rho_1 = 500$ cm, (b) $\rho_1 = 200$ cm, (c) $\rho_1 = 100$ cm, (d) $\rho_1 = 50$ cm.

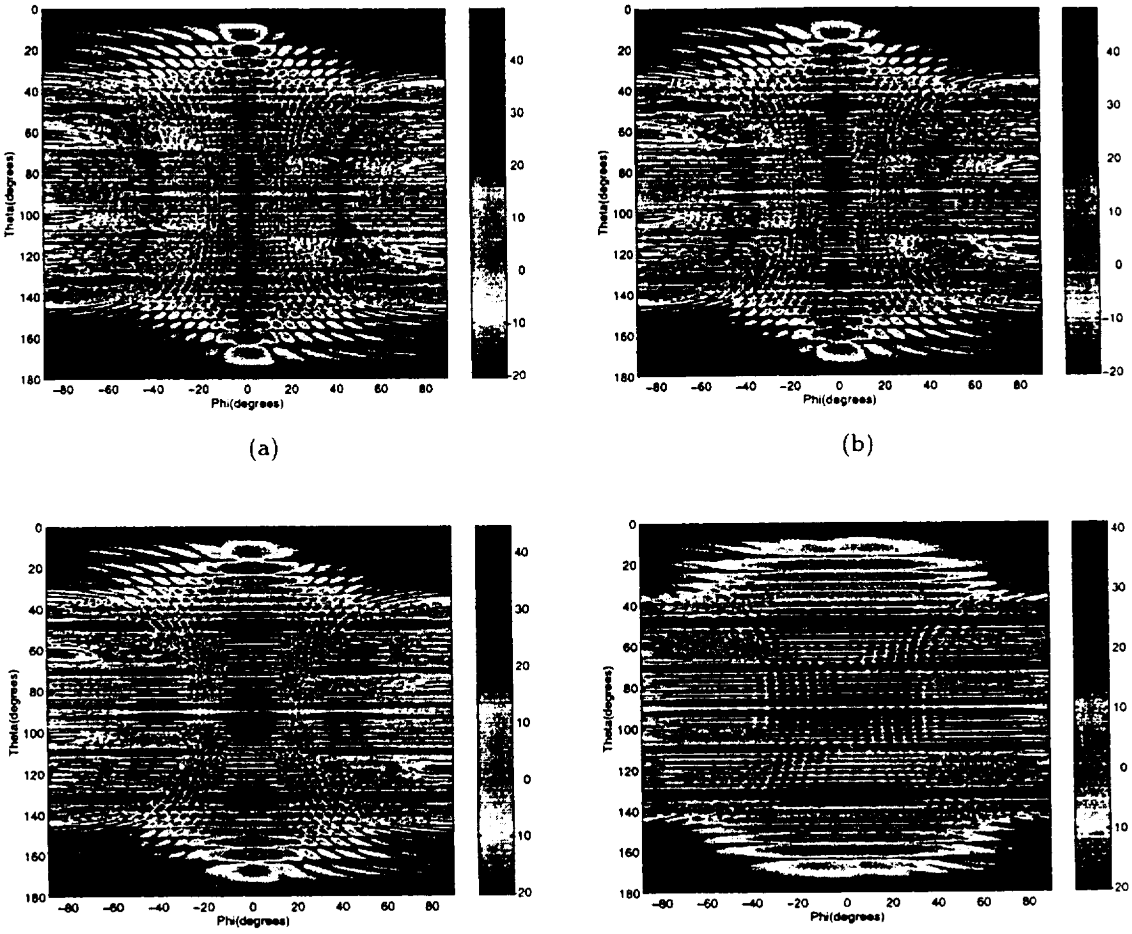

(a)

(b)

(c)

(d)

Figure 7: RCS (dBsw) of a 16 × 16 slot array with shorted terminals at $f = 9.1$ GHz. (a) planar; (b) $\rho_1 = 200$ cm; (c) $\rho_1 = 100$ cm; (d) $\rho_1 = 30$ cm.

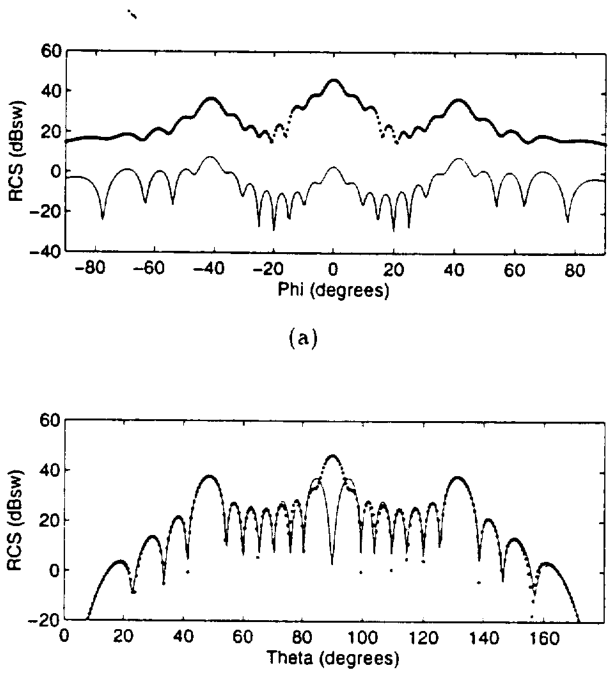

(a)

(b)

Figure 8: The effect of the terminals on the RCS of a 8 × 8 conformal slot array (ρ_1 = 100 cm). · · · matched terminals, —— shorted terminals. (a) E-plane pattern; (b) H-plane pattern.

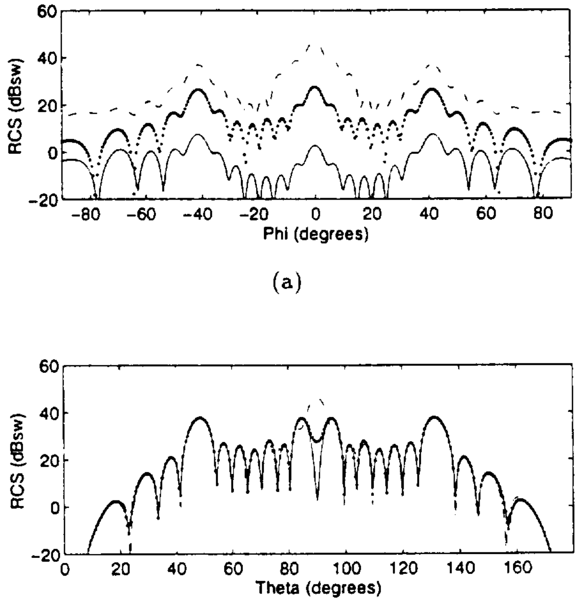

(a)

(b)

Figure 9: The effect of the position of the shorted plane on the RCS of a 8 × 8 conformal slot array ($\rho_1 = 100$ cm). —— $\Delta z = 0.001$cm, · · · $\Delta z = 0.1$cm, —·— $\Delta z = 1$cm. (a) E-plane pattern; (b) H-plane pattern.

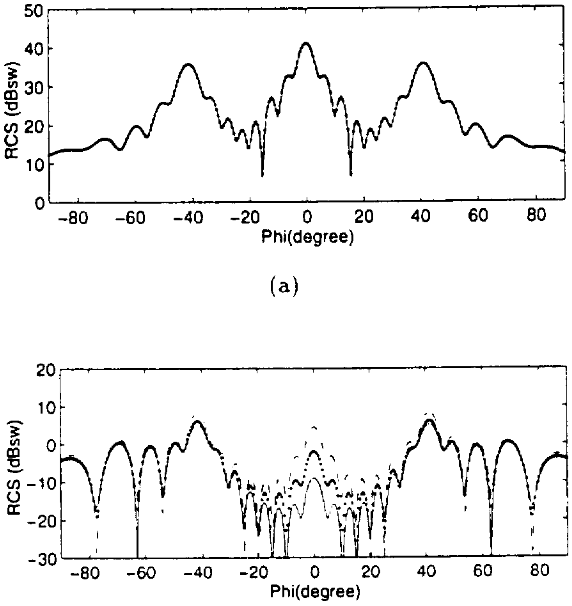

(a)

(b)

Figure 10: The effect of the slot thickness on the RCS of a 8×8 conformal slot array ($\rho_1 = 100$ cm) in the E-plane. —— $\Delta t = 1$ mm, $\cdots$ $\Delta t = 0.4$ mm, $- \cdot -$ $\Delta t = 0.1$ mm. (a) matched terminals; (b) shorted terminals.

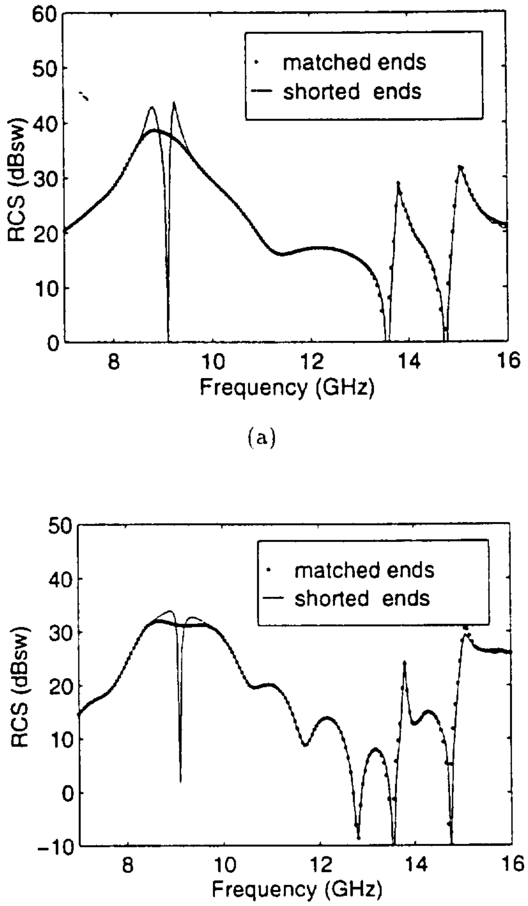

(a)

(b)

Figure 11: RCS of a 8 × 8 conformal slot array (ρ_1 = 50 cm) as a function of frequency. (a) $\theta^{inc} = 90^0$, $\varphi^{inc} = 0^0$; (b) $\theta^{inc} = 90^0$, $\varphi^{inc} = 45^0$.

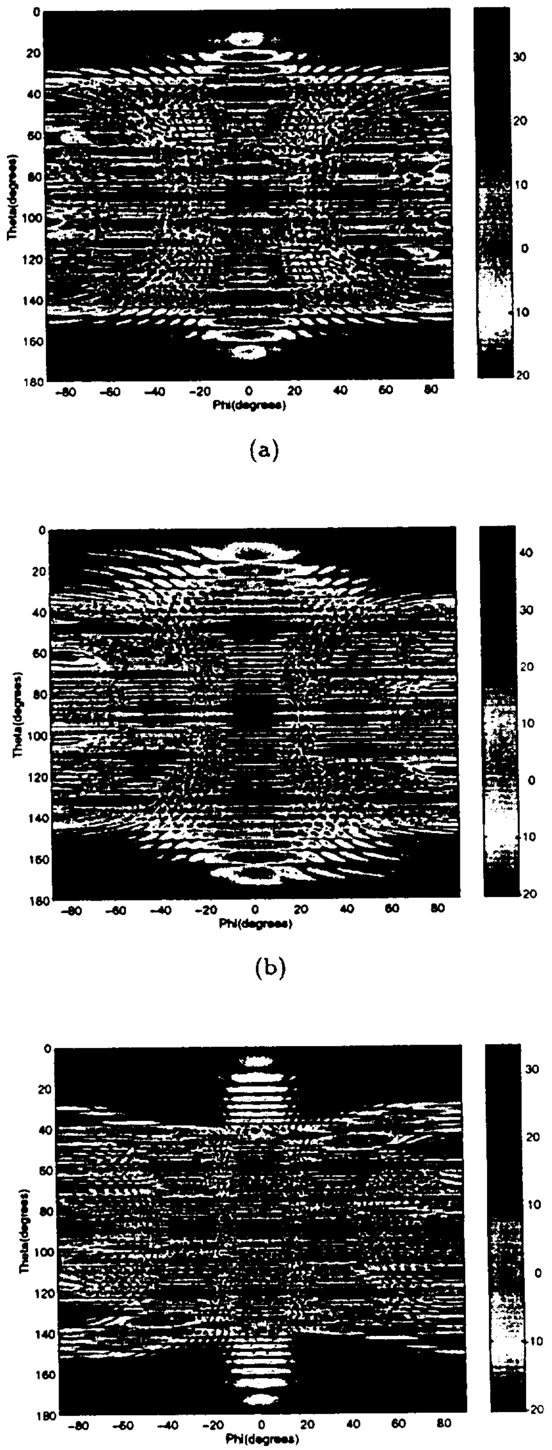

(a)

(b)

(c)

Figure 12: RCS (dBsw) of a 16 × 16 conformal slot array ($\rho_1 = 100$ cm) at three frequencies. (a) $f = 8$ GHz; (b) $f = 9.1$ GHz; (c) $f = 12$ GHz.

APPENDIX 4

SCATTERING FROM A LARGE PLANAR SLOTTED WAVEGUIDE ARRAY ANTENNA

Guo-Xin Fan and Jian-Ming Jin
Electromagnetics Laboratory
Department of Electrical and Computer Engineering
University of Illinois at Urbana-Champaign
Urbana, Illinois 61801-2991

ABSTRACT

The problem of scattering from a large planar slotted waveguide array antenna is investigated. The structural scattering and slot scattering are solved independently through the application of the equivalence principle. The former is calculated by a high-frequency method, such as the physical optics (PO) and the shooting and bouncing ray (SBR) method combined with edge diffraction. The latter is solved using the method of moments (MoM) in conjunction with global sinusoidal basis functions and Galerkin's testing technique. Special attention is paid to the evaluation of the admittance matrix elements, which involve the internal and external mutual coupling. Numerical results are presented to demonstrate the effects of a variety of factors on the radar cross section (RCS) of a slot array, and these include the number of basis functions in the MoM solution, the external mutual coupling between the slots, the waveguide terminations, and the host object. Also given are the RCS space distribution and the time responses of slot arrays to illustrate their unique scattering characteristics. The RCS of a complicated real slot array is given finally to demonstrate the capability of the numerical method as well as the distinct features of its RCS pattern.

I. INTRODUCTION

Large planar slotted waveguide array antennas are the most common antennas used on modern airborne radars. Because of their unique structures, their radar signature has a number of very unique characteristics. The study of these characteristics is important for applications such as target identification, electromagnetic compatibility, and stealth technology. Recently, we presented a method of moments (MoM) solution to scattering from a cylindrically conformal slotted waveguide array antenna [1]. The formulation is complicated because of the complex nature of the problem. Although the method can also be applied to planar slotted waveguide array antennas by treating these antennas as the limiting case of a cylindrically conformal array antenna with its radius approaching infinity, the solution is unnecessarily complicated and time consuming. Because of the practical importance of planar slot arrays, in this paper we present a specific MoM solution to this problem based on much simplified formulas, with an emphasis on the analysis of large arrays.

The scattering from a slotted waveguide array antenna consists of two parts: the slot scattering and the structural scattering. The former is contributed by the slots, and the latter is contributed by the surface of the antenna and the host object. In practical applications, slot arrays are usually placed in the region where only the direct incident field reaches. Because of this, the slot scattered field and the structural scattered field can be solved separately through the application of the equivalence principle. In this paper, we employ a high-frequency method, such as the physical optics (PO) and the shooting and bouncing ray (SBR) method combined with edge diffraction, to take into account the structural scattering and the MoM to characterize the slot scattering.

The paper is organized as follows. Section II presents the formulation for the analysis of planar slot arrays, and the emphasis is given to the calculation of all kinds of the generalized admittance matrix elements. Section III gives several typical numerical examples to illustrate the scattering properties of planar slot arrays, such as the effect of the aperture modes and external mutual coupling, the RCS space and probability distribution, the effect of the host object or platform, and the time response of a slot array. A complicated real slot array is considered finally to demonstrate the capability of the numerical method as well as the distinct features of its RCS pattern.

II. THEORY

Consider the planar slotted waveguide array antenna depicted in Fig. 1. The waveguides have a width a and height b, and their upper walls have a thickness t. Each waveguide may have a different length and may be divided into several sections. Each section is terminated with an arbitrary load. All the radiating slots are longitudinal and have the same width $2w$; however, they may have a different length and a different offset with respect to the center-line of the waveguides.

In accordance with the equivalence principle, the field outside the antenna can be decoupled from those inside the antenna by covering the slots

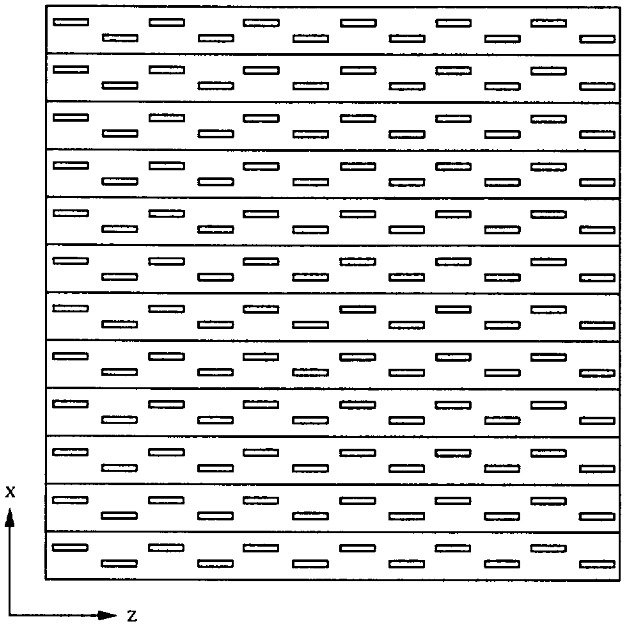

Figure 1: A planar slotted waveguide array antenna.

with a perfect conductor and introducing an equivalent magnetic current over the apertures of the slots. Therefore, the total scattered field can be decomposed into two parts. One is the field scattered by the surface of the antenna with all the slots covered by a perfect conductor and this is often referred to the structural scattered field (or structural mode), denoted as $\mathbf{E}^{stru}$. The other part is the field radiated by the equivalent magnetic currents and this is often referred to as the slot scattered field (or antenna mode), denoted as $\mathbf{E}^{slot}$. The total scattered field can then be written as

$$\mathbf{E}^{sca}(\mathbf{r}) = \mathbf{E}^{stru}(\mathbf{r}) + \mathbf{E}^{slot}(\mathbf{r}). \tag{1}$$

When the surface of the antenna is illuminated only by the incident wave and when there is no multiple reflection between the antenna and its host object, the structural scattered field and the slot scattered field can be solved for separately. Since there are many efficient high-frequency methods available to calculate the structural scattered field, we focus on the solution of the slot scattered field.

A. Integral Equations and MoM Solution

Consider the ith slot. Its lower and upper apertures, denoted as S_i^I and S_i^{II} respectively, divide the space into three regions: the waveguide region (denoted as region a), the external region (denoted as region b), and the slot region (denoted as region c) since the slot has a finite thickness. By imposing the continuity of the tangential magnetic fields on S_i^I and S_i^{II}, we obtain the integral equations satisfied by the equivalent magnetic currents, $\mathbf{M}_i^I$ and $\mathbf{M}_i^{II}$, as

$$\sum_j \mathbf{H}^a_{\tau i}(\mathbf{M}_j^I) + \mathbf{H}^c_{\tau i}(\mathbf{M}_i^I) - \mathbf{H}^c_{\tau i}(\mathbf{M}_i^{II}) = 0 \qquad \mathbf{r} \in S_i^I \tag{2}$$

$$\sum_j \mathbf{H}^b_{\tau i}(\mathbf{M}_j^{II}) + \mathbf{H}^c_{\tau i}(\mathbf{M}_i^{II}) - \mathbf{H}^c_{\tau i}(\mathbf{M}_i^I) = \mathbf{H}^{pri}_{\tau i} \qquad \mathbf{r} \in S_i^{II} \tag{3}$$

where $\mathbf{M}_i^I$ denotes the equivalent magnetic current on S_i^I and $\mathbf{M}_i^{II}$ denotes the equivalent magnetic current on S_i^{II}, $\mathbf{H}^\alpha$ denotes the magnetic field in region α, $\mathbf{H}^{pri}$ denotes the primary field which is the sum of the incident field and the field scattered by the antenna without the slots, and finally, the subscript τ denotes the tangential component of the associated field. Note that the summation in (2) is carried out for all inner apertures in the same waveguide, and the summation in (3) is carried out for all outer apertures.

For narrow slots, we can choose the global sinusoidal basis functions to expand each equivalent magnetic current

$$\mathbf{M}_j^{I,II} = \hat{z} M_j^{I,II} = \hat{z} \sum_{q=1}^{N_j^{I,II}} V_{qj}^{I,II} \sin \alpha_{qj} \xi \qquad \mathbf{r} \in S_j^{I,II} \tag{4}$$

where $\alpha_{qj} = q\pi / L_j$ with L_j being the length of the jth slot, $N_j^{I,II}$ denotes the number of basis functions, and ξ varies from 0 at the one end of the slot to L_j at the other end. By employing Galerkin's technique, the integral equations can be converted into the matrix equation given by

$$\begin{bmatrix} \left[Y_{pq}^{ij}(a) + Y_{pq}^{ij}(c, S_i^I; S_j^I) \right] & \left[-Y_{pq}^{ij}(c, S_i^I; S_j^{II}) \right] \\ \left[-Y_{pq}^{ij}(c, S_i^{II}; S_j^I) \right] & \left[Y_{pq}^{ij}(b) + Y_{pq}^{ij}(c, S_i^{II}; S_j^{II}) \right] \end{bmatrix} \begin{Bmatrix} \left[V_{qj}^I \right] \\ \left[V_{qj}^{II} \right] \end{Bmatrix} = \begin{Bmatrix} [0] \\ [I_{pi}] \end{Bmatrix}. \tag{5}$$

In the equation above, the generalized admittance matrix elements and excitation vector elements have the same physical meaning as those of the conformal slot array [1].

We note that for slots of zero thickness, the edge condition is often employed to represent the transverse variation of the equivalent magnetic current [2]-[4], which makes the evaluation of the matrix elements difficult. For slots of finite thickness as is the case for practical applications, the singularity is much weaker than for the zero thickness case. As a result, the equivalent magnetic current can be expanded in terms of the global sinusoidal basis functions with a uniform transverse distribution. Such an expansion has been successfully used in the past for the analysis of rectangular waveguide slot radiation problems [5]-[8].

B. Generalized Admittance Matrix Elements for Region a

The admittance matrix elements due to the internal coupling in the rectangular waveguide (region a) are given by

$$Y_{pq}^{ij}(a) = \iint\limits_{S_i^I}\iint\limits_{S_j^I} G_{zz}^{a}(\mathbf{r},\mathbf{r}') \sin\alpha_{pi}\xi \, \sin\alpha_{qj}\xi' \, dS \, dS' \tag{6}$$

where G_{zz}^{a} is the $\hat{z}\hat{z}$-component of the magnetic-source magnetic-field dyadic Green's function for the rectangular waveguide, which is given by

$$\begin{aligned} G_{zz}^{a} = j\omega\epsilon \sum_{m=0}^{\infty}\sum_{n=0}^{\infty} B(m,n)\, C_x C_{x'} C_y C_{y'} \Big\{ \delta(z-z') \\ - \frac{\lambda_{mn}^2}{2jh_{mn}\Delta_{mn}} \Big[e^{-jh_{mn}|z-z'|} - R_{mn}^{<} e^{j2h_{mn}z_1} e^{-jh_{mn}(z+z')} \\ - R_{mn}^{>} e^{-j2h_{mn}z_2} e^{jh_{mn}(z+z')} + (1-\Delta_{mn}) e^{jh_{mn}|z-z'|} \Big] \Big\}. \end{aligned} \tag{7}$$

In this expression,

$$B(m,n) = \frac{2}{1+\delta_{0m}} \frac{2}{1+\delta_{0n}} \frac{1}{k^2 ab} \tag{8}$$

and $C_x = \cos\nu x$, $C_{x'} = \cos\nu x'$, $C_y = \cos\mu y$, $C_{y'} = \cos\mu y'$, $\nu = m\pi/a$, $\mu = n\pi/b$, $\lambda_{mn}^2 = \nu^2 + \mu^2$, $h_{mn} = \sqrt{k^2 - \lambda_{mn}^2}$, $\Delta_{mn} = 1 - R_{mn}^{<} R_{mn}^{>} e^{-jh_{mn}(z_2 - z_1)}$, and $R_{mn}^{<}$ and $R_{mn}^{>}$ are the reflection coefficients for mode $(m,\ n)$ at the two ends of the waveguide, located at $z = z_1$ and $z = z_2$, respectively.

The integrals in (6) can be evaluated analytically through the change of variables, resulting in

$$\begin{aligned} Y_{pq}^{ij}(a) &= \int_0^{L_i}\int_{-w}^{w}\int_0^{L_j}\int_{-w}^{w} G_{zz}^{a}(\mathbf{r},\mathbf{r}') \sin\alpha_{pi}\xi \sin\alpha_{qj}\xi' d\eta' d\xi' d\eta d\xi \\ &= -j\omega\epsilon \sum_{m=0}^{\infty}\sum_{n=0}^{\infty} B(m,n) I_x^{ij}(m) \left[I_{z0}^{ij}(m,n) + I_{zim}^{ij}(m,n) \right] \end{aligned} \tag{9}$$

where

$$I_x^{ij}(m) = [2w\,\mathrm{sinc}(\nu w)]^2 \cos\left[\nu\left(\frac{a}{2}+\delta_i\right)\right] \cos\left[\nu\left(\frac{a}{2}+\delta_j\right)\right] \tag{10}$$

$$I_{z0}^{ii}(m,n) = C(m,n)\left[1+(-1)^{p+q}\right]\left[1-(-1)^p e^{-jh_{mn}L_i}\right] + \delta_{pq}\frac{(k^2-\alpha_{pi}^2)L_i}{\alpha_{pi}^2 - h_{mn}^2} \tag{11}$$

$$\begin{aligned} I_{z0}^{ij}(m,n) &= C(m,n) e^{\mp jh_{mn}[(z_{0i}-z_{0j})-(L_i-L_j)/2]} \\ &\cdot \left[1-(-1)^p e^{\mp jh_{mn}L_i}\right]\left[1-(-1)^q e^{\pm jh_{mn}L_j}\right] \qquad z_{0i} \gtrless z_{0j} \end{aligned} \tag{12}$$

with

$$C(m,n) = \frac{\lambda_{mn}^2}{2jh_{mn}\Delta_{mn}} \frac{\alpha_{pi}}{\alpha_{pi}^2 - h_{mn}^2} \frac{\alpha_{qj}}{\alpha_{qj}^2 - h_{mn}^2} \tag{13}$$

in which δ_i denotes the offset of the ith slot from the center of the waveguide, and z_{0i} and z_{0j} denote the center of the ith and jth slots, respectively. Finally, $I_{zim}^{ij}(m,n)$ are the same as those in [1].

For the mutual coupling between different slots (that is, when $i \neq j$), the summation of the double series in (9) can be evaluated directly without any difficulty due to the fast evanescence of higher-order waveguide modes. For the self coupling element (that is, when $i = j$), its evaluation involves a slowly converging series, given by

$$\sum_{n=0}^{\infty} B(m,n)\delta_{pq}\frac{(k^2-\alpha_{pi}^2)L_i}{\alpha_{pi}^2 - h_{mn}^2} = \delta_{pq}L_i\frac{k^2-\alpha_{pi}^2}{k^2ab}\left(\frac{b}{\pi}\right)^2 \sum_{n=0}^{\infty}\frac{2}{1+\delta_{0n}}\frac{1}{n^2+x^2} \tag{14}$$

where $x^2 = (b/\pi)^2(\alpha_{pi}^2 - k^2 + \nu^2)$. However, this term can be evaluated analytically in a closed form since

$$\sum_{n=0}^{\infty}\frac{2}{1+\delta_{0n}}\frac{1}{n^2+x^2} = \frac{\pi}{x}\coth \pi x. \tag{15}$$

C. Generalized Admittance Matrix Elements for Region b

The admittance matrix elements due to the external coupling in region b are given by

$$Y_{pq}^{ij}(b) = \iint\limits_{S_i^{II}} \iint\limits_{S_j^{II}} G_{zz}^{b}(\mathbf{r},\mathbf{r}') \sin \alpha_{pi}\xi \, \sin \alpha_{qj}\xi' \, dS \, dS' \tag{16}$$

where G_{zz}^b is the $\hat{z}\hat{z}$-component of the magnetic-source magnetic-field dyadic Green's function for the outer space. As usual, when the surface of the antenna is large enough and the interference from the surrounding objects can be ignored, G_{zz}^b can be approximated by the corresponding Green's function G_{zz}^0 for an infinite conducting ground plane,

$$G_{zz}^b \approx G_{zz}^0 = \frac{k^2}{j\omega\mu}\left(1 + \frac{1}{k^2}\frac{\partial^2}{\partial z^2}\right)\frac{e^{-jkt}}{2\pi t} \tag{17}$$

where $t = \sqrt{(x-x')^2 + (z-z')^2}$.

When the source point and the field point are in the same aperture (that is, when $i = j$), G_{zz}^b has a t^{-3} singularity as $t \to 0$, and a regularization is needed to evaluate the integrals. However, this singularity can be reduced to the order of t^{-1} using integration by parts. As a result, $Y_{pq}^{ii}(b)$ can be written as

$$Y_{pq}^{ii}(b) = \frac{k^2}{j\omega\mu} \frac{1+(-1)^{p+q}}{2\pi k^2} \left\{ \int_0^{\theta_0} \int_0^{L_i/\cos\theta} + \int_{\theta_0}^{\pi/2} \int_0^{2w/\sin\theta} \right\} \times F(t\sin\theta, t\cos\theta)\, e^{-jkt}\, dt\, d\theta \tag{18}$$

where $\theta_0 = \tan^{-1}(2w/L_i)$ and

$$F(u,v) = \begin{cases} \dfrac{2(2w-v)}{\alpha_{pi}^2 - \alpha_{qi}^2} \left[\alpha_{pi}(k^2 - \alpha_{qi}^2) \sin\alpha_{qi}u - \alpha_{qi}(k^2 - \alpha_{pi}^2) \sin\alpha_{pi}u\right] \\ \qquad\qquad\qquad\qquad\qquad\qquad\qquad\qquad p \neq q \\ (2w-v)\left[(L_i - u)(k^2 - \alpha_{pi}^2)\cos\alpha_{pi}u + \frac{1}{\alpha_{pi}}(k^2 + \alpha_{pi}^2)\sin\alpha_{pi}u\right] \\ \qquad\qquad\qquad\qquad\qquad\qquad\qquad\qquad p = q. \end{cases} \tag{19}$$

In arriving at (18), we have applied a series of variable transformations [7].

When $i \neq j$, the expression for the mutual admittance matrix elements can be written as

$$Y_{pq}^{ij}(b) = \int_0^{L_i} \int_{-w}^{w} \int_0^{L_j} \int_{-w}^{w} G_{zz}(x-x', z-z')\ \sin\alpha_{pi}\xi\ \sin\alpha_{qi}\xi'\ d\eta'\, d\xi'\, d\eta\, d\xi \tag{20}$$

with

$$\begin{aligned} z - z' &= (\xi - \xi') + (z_{0i} - z_{0j}) + (L_i - L_j)/2 \\ x - x' &= (\eta - \eta') + (x_{0i} - x_{0j}) \end{aligned} \tag{21}$$

where x_{0i} and x_{0j} are the coordinates of the center of the ith and jth slots, respectively. For large practical slot arrays, the length difference between the slots is small. Using the average slot length of the two slots to approximate their lengths [7], [8], that is,

$$L_i \approx L_j \approx (L_i + L_j)/2 \equiv L, \tag{22}$$

and introducing the transformations $u = \xi - \xi'$ and $u' = \xi + \xi' - L$, with the aid of the midpoint integration, we have

$$Y_{pq}^{ij}(b) = 2w^2 \int_0^L \left[G_0(u) + (-1)^{p+q} G_0(-u)\right] \widetilde{F}(u)\, du \tag{23}$$

where

$$G_0(u) = \frac{k^2}{j\omega\mu} \frac{e^{-jk\sqrt{(x_{0i}-x_{0j})^2 + (u+z_{0i}-z_{0j})^2}}}{2\pi\sqrt{(x_{0i}-x_{0j})^2 + (u+z_{0i}-z_{0j})^2}} \tag{24}$$

and

$$\widetilde{F}(u) = \begin{cases} \dfrac{2}{\alpha_{pi}^2 - \alpha_{qi}^2}\left[(-1)^{p+q}\alpha_{pi}\sin\alpha_{qi}u - \alpha_{qi}\sin\alpha_{pi}u\right] & p \neq q \\ (L_i - u)\cos\alpha_{pi}u + \dfrac{1}{\alpha_{pi}}\sin\alpha_{pi}u & p = q. \end{cases} \tag{25}$$

D. Generalized Admittance Matrix Elements for Region c

The procedure similar to that in [1] can be employed to obtain the expressions for the generalized admittance matrix elements for region c. The magnetic field in the cavity formed by the slot with its two apertures covered by a perfectly conducting sheet, produced by the surface magnetic current $\hat{z}\delta(y-y')\sin\alpha_{pi}\xi$, is related to the magnetic vector potential by

$$H_z = \frac{k^2}{j\omega\mu}\left(1+\frac{1}{k^2}\frac{\partial^2}{\partial\xi^2}\right)A_{mz} \tag{26}$$

where A_{mz} satisfies the wave equation

$$(\nabla^2+k^2)A_{mz} = -\delta(y-y')\,\sin\alpha_{pi}\xi, \qquad \mathbf{r}\in V_c \tag{27}$$

and the boundary conditions

$$\left.\frac{\partial A_{mz}}{\partial x}\right|_{x=\pm w} = 0, \qquad \left.\frac{\partial A_{mz}}{\partial y}\right|_{y=0,t} = 0, \qquad \left.A_{mz}\right|_{\xi=0,L_i} = 0. \tag{28}$$

Assuming $A_{mz}(x,y,\xi) = Y(y,y')\sin\alpha_{pi}\xi$, we have

$$\frac{d^2Y}{dy^2}+\beta^2 Y = -\delta(y-y'), \tag{29}$$

$$\left.\frac{dY}{dy}\right|_{y=0,t} = 0. \tag{30}$$

where $\beta=\sqrt{k^2-\alpha_{pi}^2}$ for $k>\alpha_{pi}$, and $\beta = j\sqrt{\alpha_{pi}^2-k^2}$ for $k<\alpha_{pi}$. The solution of (29) and (30) is

$$Y(y,y') = -\cos\beta y_< \,\cos\beta(t-y_>)\,/\,\beta\sin\beta t \tag{31}$$

where $y_< = \min(y,y')$, $y_> = \max(y,y')$. Evaluating the inner product between the aperture magnetic fields and the testing functions, we finally obtain

$$Y^{ij}_{pq}(c,S^I_i;S^I_j) = Y^{ij}_{pq}(c,S^{II}_i;S^{II}_j) = -\frac{L_i w\beta}{j\omega\mu}\cot\beta t\,\delta_{ij}\delta_{pq} \tag{32}$$

$$Y^{ij}_{pq}(c,S^I_i;S^{II}_j) = Y^{ij}_{pq}(c,S^{II}_i;S^I_j) = -\frac{L_i w\beta}{j\omega\mu}\csc\beta t\,\delta_{ij}\delta_{pq}. \tag{33}$$

E. Excitation Vector

For an incident plane wave of arbitrary polarization and incident angle, whose electric field is given by

$$\mathbf{E}^{inc} = (\hat{\theta}^{inc}\cos\psi+\hat{\phi}^{inc}\sin\psi)e^{-j\,\mathbf{k}^{inc}\cdot\mathbf{r}} \tag{34}$$

where ψ is the polarization angle and $(\theta^{inc}, \phi^{inc})$ denote the incident angles, we obtain the elements of the excitation vector as

$$I_{pi} = \frac{4wY_0\alpha_{pi}}{\alpha_{pi}^2 - k_z^2}\left[(-1)^p e^{jk_zL_i} - 1\right] \sin\psi \sin\theta^{inc} \operatorname{sinc}(k_x w) \\ \times e^{j[k_x(x_{0i}+\delta_i)+k_y y_0 + k_z(z_{0i}-L_i/2)]} \tag{35}$$

where y_0 denotes the y coordinate of the upper apertures of the slots. Note that for scattering calculation, the spherical coordinate system is defined such that the normal at the center of the array is $\theta = 90^0$ and $\phi = 0^0$, which is obviously different from the rectangular coordinates used for the waveguides.

F. Scattered Field and RCS

Once the equivalent magnetic currents on the slot apertures are found, we can compute the scattered field by slots, which is the radiated field due to the equivalent magnetic currents. Meanwhile, for a large array, we can employ a high-frequency method, such as PO or SBR, to calculate the structural scattered field. The total scattered field is the sum of these two fields.

The RCS of the slot array antenna is defined as

$$\sigma = \lim_{r\to\infty} 4\pi r^2 \left| \frac{\mathbf{E}^{sca}(\mathbf{r})}{\mathbf{E}^{inc}(\mathbf{r})} \right|^2 = \lim_{r\to\infty} 4\pi r^2 \left| \frac{\mathbf{E}^{slot}(\mathbf{r}) + \mathbf{E}^{stru}(\mathbf{r})}{\mathbf{E}^{inc}(\mathbf{r})} \right|^2 . \tag{36}$$

Another parameter of practical importance is the RCS probability of a slot array antenna over a space solid angle Ω_0, which can be defined as

$$P(\sigma \geq \sigma_0) = \frac{1}{\Omega_0} \iint\limits_{\Omega_0} U\left[\sigma(\theta, \phi) - \sigma_0\right] \sin\theta \, d\theta \, d\phi \tag{37}$$

where σ_0 is a given value of RCS, and $U(x)$ is the unit step function.

III. NUMERICAL RESULTS

For all the examples considered except for those mentioned otherwise, the cross-section of waveguides is given by $a = 21$ mm and $b = 5.0$ mm. The distance between the center-lines of the adjacent waveguides is 22 mm. The adjacent slots on the same waveguide are spaced $\lambda_{g0}/2$ apart in the z direction, where λ_{g0} is the waveguide wavelength at the working frequency. The shorted planes are placed $\lambda_{g0}/4$ away from the first and last slots, respectively. All other parameters, unless otherwise specified, are given by: $2w = 1.6$ mm, $L_i = 16$ mm, $\delta_i = 1.5$ mm, $t = 0.8$ mm, $\psi = 90^0$, and the working frequency $f_0 = 9.1$ GHz.

To verify the theory above and the computer program, comparisons are made between its solution and those obtained by MoM and FEM [9] for a single slot and four slots on a single waveguide. Good agreement is obtained between the three solutions. In addition, the validation is also confirmed by comparisons between the results of a planar slot array and those of a conformal slot array on a very large cylinder as shown in [1].

We first study the effect of the number of basis functions or aperture modes in (4) on the calculation of RCS. The choice of this number depends on several factors, such as the slot offset, the height of waveguide, and frequency. In large practical slot arrays, the slot offset is usually small. Numerical results show that within a finite bandwidth near the working frequency, only three modes are needed for a good accuracy. In many cases, especially at a frequency near or below the working frequency, a single-mode approximation can yield an acceptable accuracy. Figures 2 and 3 show the effect of the number of modes on the RCS of a slot array (excluding the structural scattered field) at three frequencies. The use of a minimum number of modes makes it possible to analyze very large slot arrays.

Next, we study the effect of the mutual coupling through the exterior space (region b). Unlike the internal mutual coupling that only exists between the slots in the same waveguide, the external mutual coupling exists between all the slots. Although the fourfold integral in (16) has been reduced to a single integral in (23) for the computation of the external mutual coupling, it is still very time consuming to calculate all these matrix elements when the slot array is very large. One possible solution is to ignore the mutual coupling when the two slots are far apart. Figure 4 shows the effect of the external mutual coupling on the RCS patterns (excluding the structural scattered field). Three curves are plotted in the figure: one with all the mutual coupling, another with no mutual coupling at all, and the third one with the coupling with the surrounding 9×5 slots (9 waveguides each containing 5 slots). It is apparent that by including the mutual coupling between the adjacent slots, one can obtain a sufficient accuracy.

The effects of the structural and slot scattered fields are illustrated in Fig. 5, which shows the RCS pattern of a circular slot array consisting of 32 waveguides with 32 slots in the central waveguide of the array (hereafter referred to as 32×32 circular slot array). The radius of the antennas is 16 in. The pattern of the antenna without the slots (that is, the structural scattered field) is also given for comparison. It can be seen that the structural scattering forms a strong peak in the normal direction of the plate. The major effect of the slot scattered field is the grating lobes.

Figure 6 gives the space distribution of the RCS of the 32×32 circular slot array, including both the structural and slot scattered fields. The main RCS peaks away from the normal direction are due to the slot scattering.

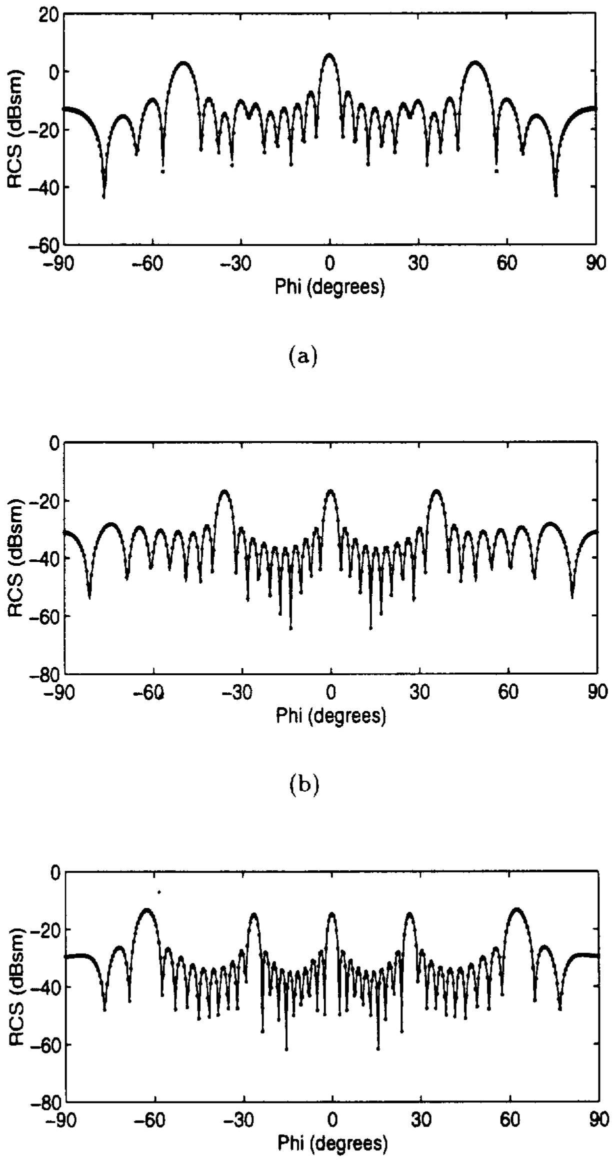

(a)

(b)

(c)

Figure 2: The effect of the number of aperture modes on the RCS in the E-plane for an 8 × 8 slot array with shorted terminals. —— 7 modes; – – 5 modes; –·– 3 modes; ··· 1 mode. (a) $f = 8$ GHz; (b) $f = 9.1$ GHz; (c) $f = 12$ GHz.

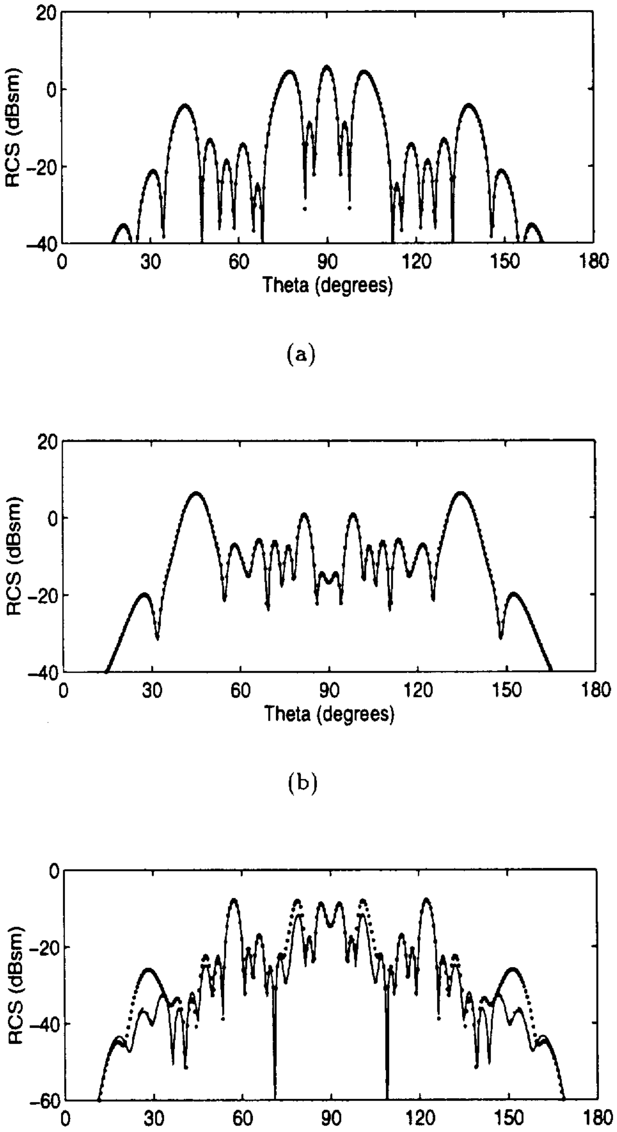

(a)

(b)

(c)

Figure 3: The effect of the number of aperture modes on the RCS in the H-plane for an 8×8 slot array with shorted terminals. —— 7 modes; – – 5 modes; –·– 3 modes; ··· 1 mode. (a) $f = 8$ GHz; (b) $f = 9.1$ GHz; (c) $f = 12$ GHz.

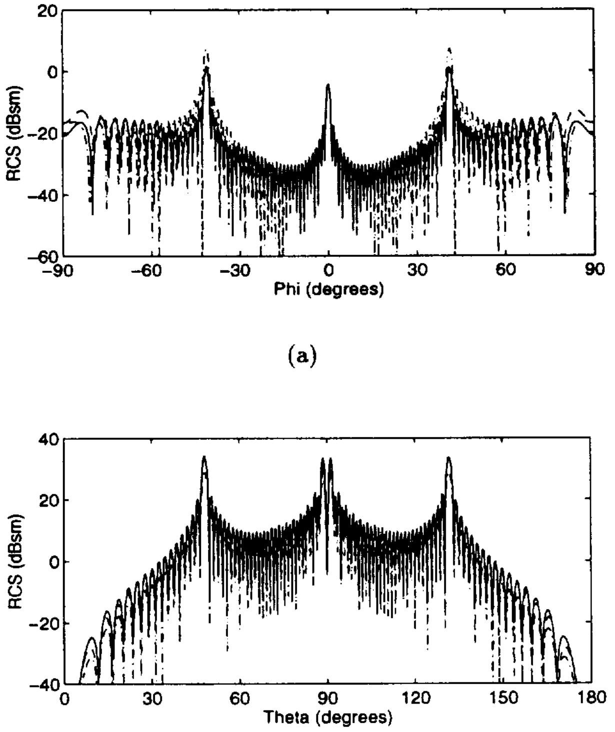

(a)

(b)

Figure 4: The effect of the external coupling on the RCS for a 32 × 32 rectangular slot array with shorted terminals at $f = 9.1$ GHz. —— all slots; – – 9 × 5 slots; –·– no external coupling. (a) E-plane; (b) H-plane.

From the data in Fig. 6, we can calculate the RCS probability using (37) and the result is shown in Fig. 7. The space solid angle Ω_0 in (37) is specified by a cone half-angle, denoted as θ_0, where $\theta_0 = 0$ in the direction normal to the surface of the antenna.

To demonstrate the effect of a slot array antenna on the RCS of the host object, we place the 32 × 32 circular slot array antenna in the nose of an airplane. The radome covering the antenna is ignored because it is largely transparent at the working frequency. The airplane is in the normally flying position (horizontal) and the RCS of the entire object is given in Fig. 8. The structural scattered field is calculated using the high-frequency code XPATCH [10], which is based on the SBR method, and for the calculation, the airplane is assumed to be a perfect conductor. We note that although the size of the slot array is small compared with that of the airplane, its

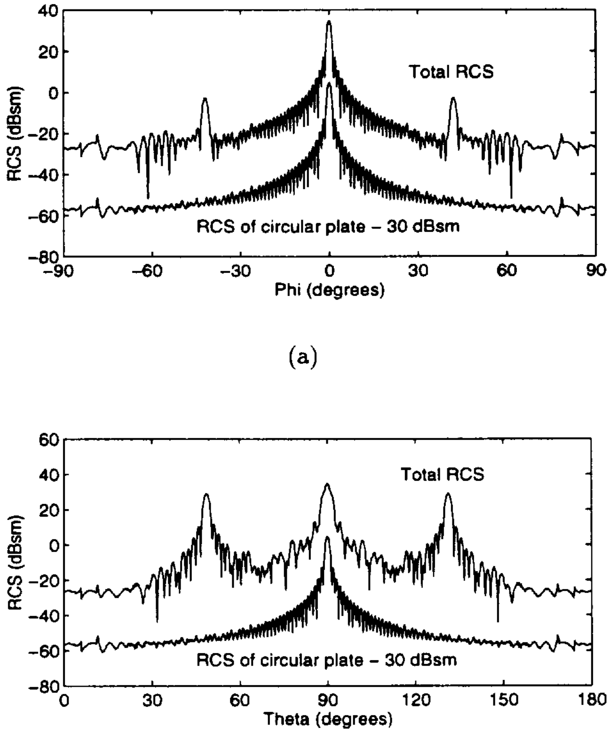

(a)

(b)

Figure 5: RCS of a 32 × 32 circular slot array with matched terminals at $f = 9.1$ GHz. (a) E-plane; (b) H-plane.

scattering dominates in some angles corresponding to those of the grating lobes.

The time response of a slot array is studied using a slot array of 8 identical waveguides with 2 slots on each waveguide as depicted in Fig. 9. The time response, shown in Figs. 10 and 11, is obtained by using the inverse fast Fourier transform (FFT) of the frequency response over a bandwidth from 8 to 12 GHz. In the example shown in Fig. 10, the waveguide terminals are matched and the two different intervals between the slots are used, $d =$ 100 and $d =$ 200 cm, respectively. The first two peaks correspond to the scattering directly from the two rows of the slots, respectively, and their intervals in time are $2d\cos\theta^{inc}/c = 3.3$ and 6.6 ns, as expected. The third peak comes from the first interaction between the slots: the wave enters the waveguide from the first (and second) slot and comes out from the second (and first) slot. In the example of Fig. 11, the one end of the waveguides

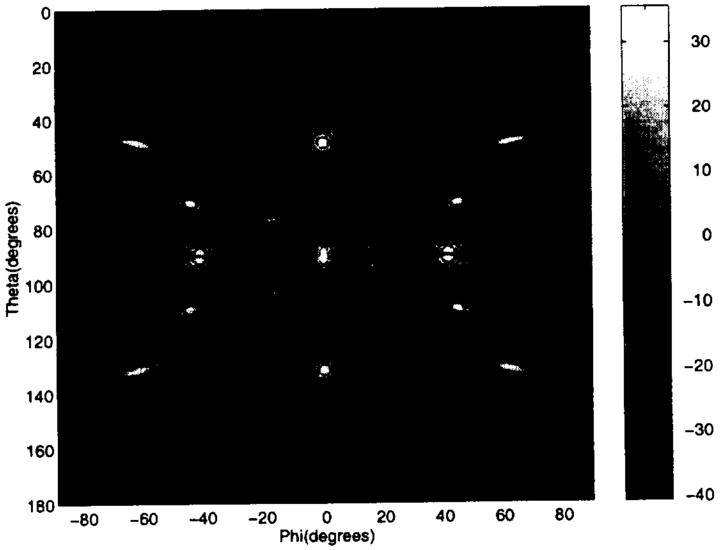

Figure 6: The RCS (dBsm) space distribution of a 32 × 32 circular slot array with shorted terminals at $f = 9.1$ GHz.

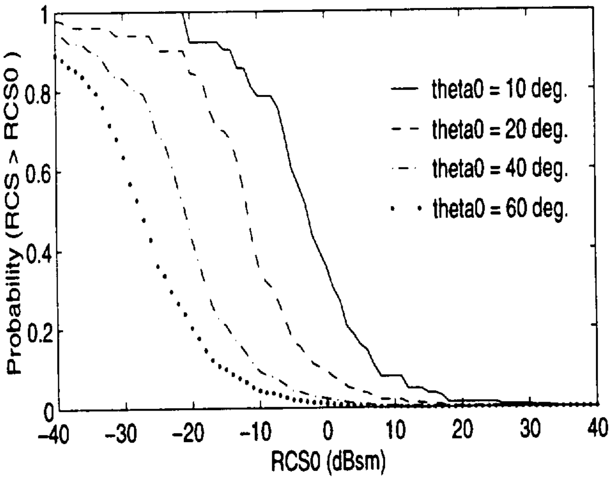

Figure 7: The RCS probability distribution of a 32 × 32 circular slot array with shorted terminals at $f = 9.1$ GHz.

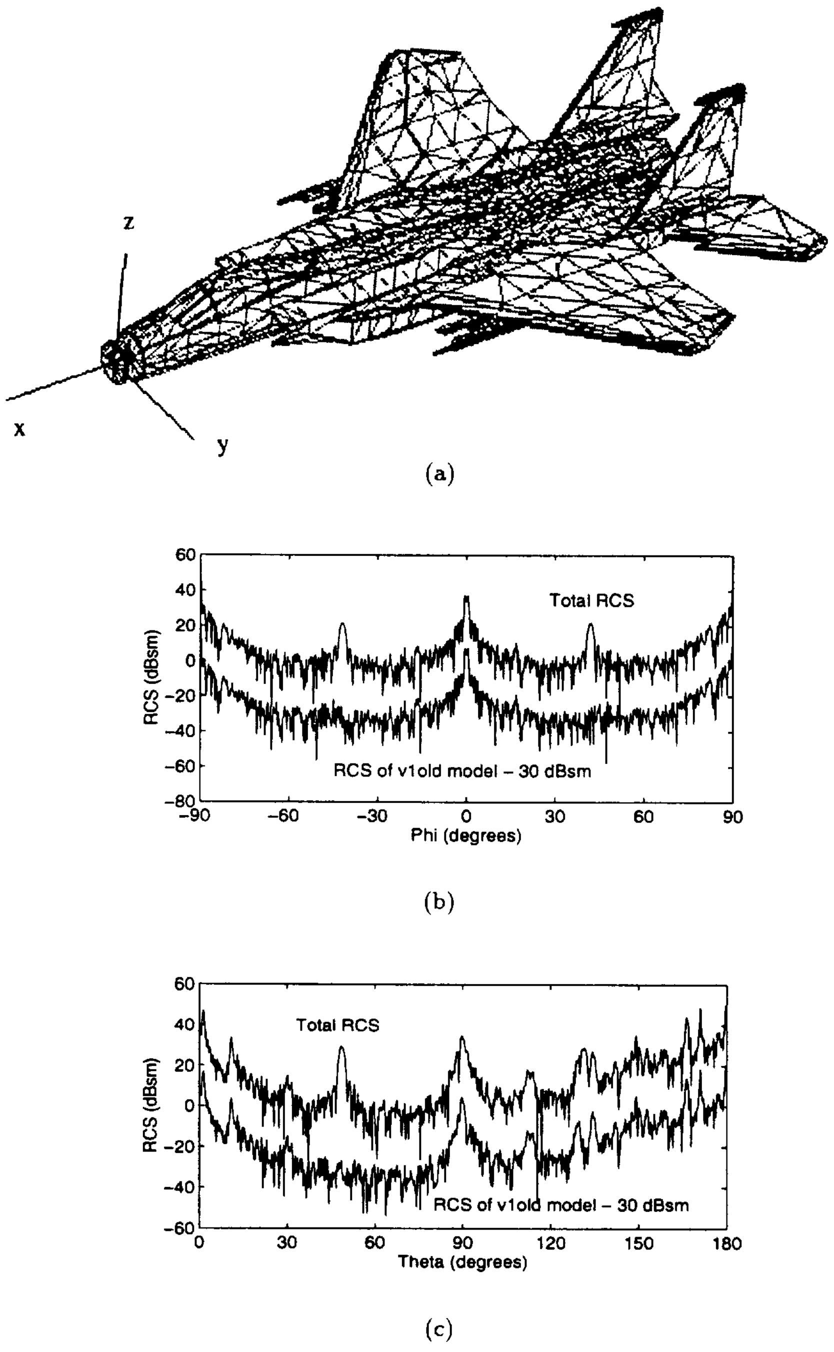

Figure 8: RCS of a v1old airplane model with a 32 × 32 circular slot array with matched terminals at $f = 9.1$ GHz. (a) v1old model; (b) E-plane; (c) H-plane.

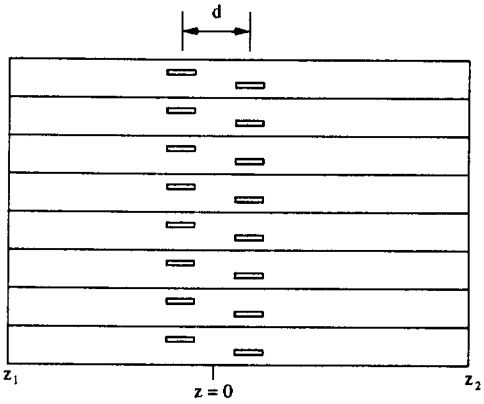

Figure 9: An 8 × 2 slot array.

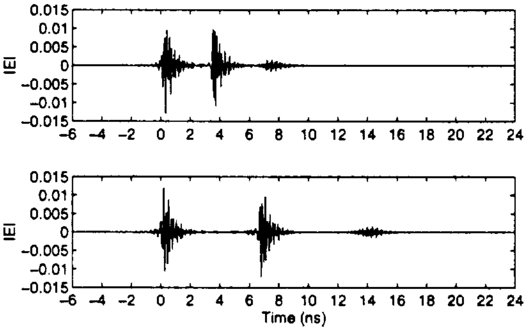

Figure 10: The time response of a 8 × 2 slot array with matched terminals exited by an incident wave with $\theta^{inc} = 60^o$, $\phi^{inc} = 0^o$. (a) $d = 100$ cm; (b) $d = 200$ cm.

is matched and the other end is shorted at three different positions. The second response is due to the field entered the waveguide through the slots, reflected by the shorted terminal, and re-radiated from the slots. It is clearly seen that the time delay of the second response is proportional to the length of the waveguides.

In the last example, we consider a real slot array antenna constructed in our laboratory. The configuration of one quarter of this antenna is shown in Fig. 12. Each waveguide is divided into several short sections, each containing only four slots except for those next to the edge of the antenna. The entire antenna consists of 40 waveguides with 42 slots in the central waveguide of the array (hereafter referred to as 40 × 42 circular slot array). Other parameters are: $a = 21.3$ mm, $b = 5$ mm, $2w = 3.3$ mm, $L_i = 16.2$ mm,

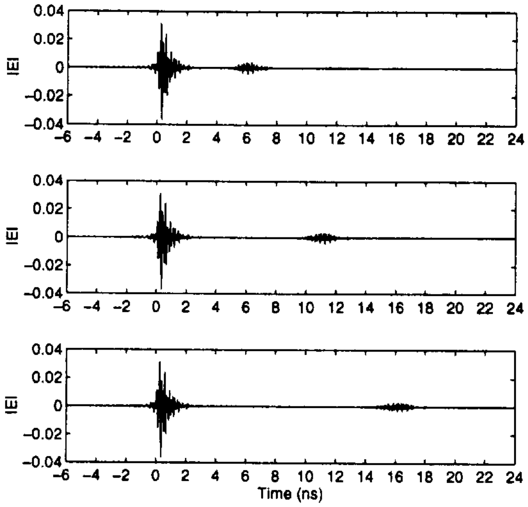

Figure 11: The time response of a 8 × 2 slot array with $d = \lambda_{g0}/2$ and a shorted terminal at z_1 and a matched terminal at z_2 exited by an incident wave with $\theta^{inc} = 90^o$, $\phi^{inc} = 0^o$. (a) $z_1 = 50$ cm; (b) $z_1 = 100$ cm; (c) $z_1 = 150$ cm.

$\delta_i = 2$ mm, $t = 0.5$ mm, and the working frequency $f_0 = 9.9$ GHz. The calculated RCS patterns are given in Fig. 13, which include the structural scattered field. As can be seen, the RCS pattern in the H-plane is substantially different from that when the waveguides are not divided into several sections [see Fig. 5(b)], whereas the pattern in the E-plane remains similar. There are several additional grating lobes in the H-plane, which are caused by an array whose elements are the short sections. Finally, Fig. 14 shows the RCS when this antenna is placed in the nose of the airplane depicted in Fig. 8(a).

IV. CONCLUSION

This paper investigates the problem of scattering from a large planar slotted waveguide array antenna. The total scattering consists of two parts, namely the structural scattering and slot scattering, and these two parts are solved independently through the application of the equivalence principle. The former is calculated by a high-frequency method, such as the PO and SBR method. The latter is solved using the MoM in conjunction with global sinusoidal basis functions and Galerkin's testing technique. Special attention is paid to the evaluation of the admittance matrix elements, which involve the internal and external mutual coupling. Numerical results are presented to demonstrate the effects of a variety of factors on the RCS of a slot array,

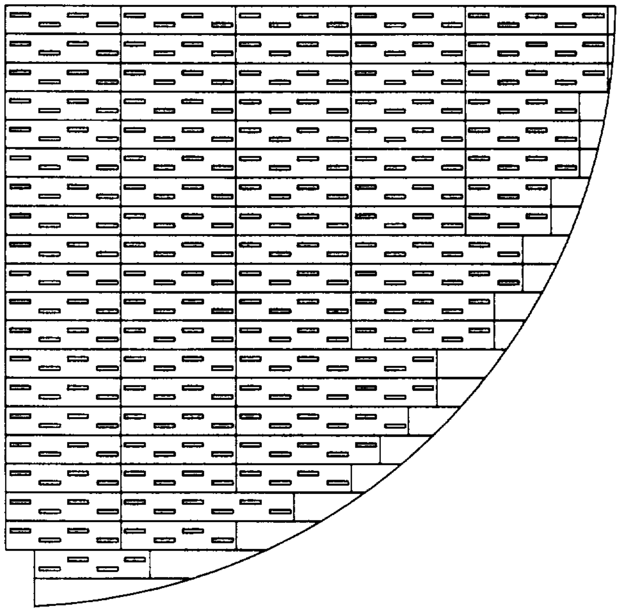

Figure 12: An 40 × 42 circular slotted-waveguide array.

and these factors include the number of basis functions in the MoM solution, the external mutual coupling between the slots, the waveguide terminations, and the host object. Also given are the RCS space distribution and probability curves and the time responses of slot arrays to illustrate their unique scattering characteristics. The RCS of a complicated real slot array is given finally to demonstrate the capability of the numerical method as well as the distinct features of its RCS pattern. The numerical method developed are useful in applications such as target identification, electromagnetic compatibility, EMP penetration, and stealth technology.

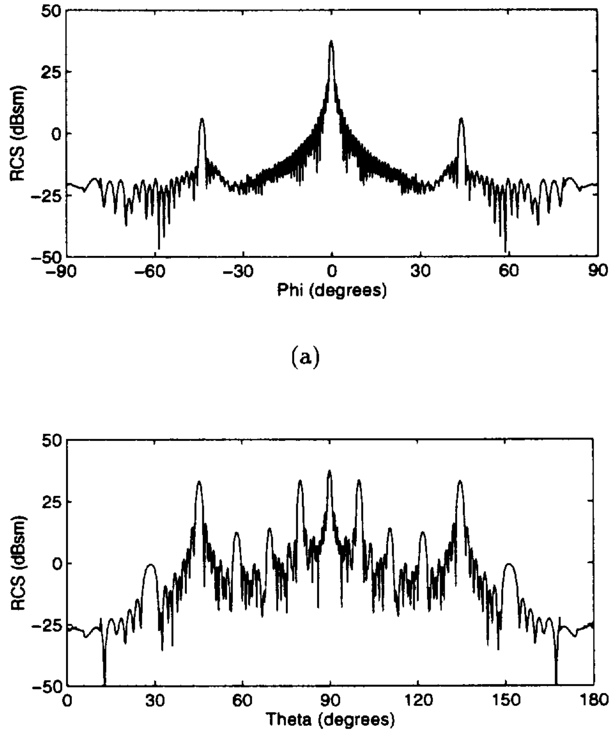

(a)

(b)

Figure 13: RCS of a 40 × 42 circular slot array with shorted terminals at $f = 9.9$ GHz. (a) E-plane; (b) H-plane.

References

[1] G.-X. Fan and J.-M. Jin, "Scattering from a cylindrically conformal slotted waveguide array antenna," *IEEE Trans. Antennas Propagat.*, vol. 45, pp. 1150-1159, July 1997.

[2] G. J. Stern and R. S. Elliott, "Resonant length of longitudinal slots and validity of circuit representation: Theory and experiment," *IEEE Trans. Antennas Propagat.*, vol. 33, pp. 1264-1271, Nov. 1985.

[3] P. B. Katehi, "Dielectric-covered waveguide longitudinal slots with finite wall thickness," *IEEE Trans. Antennas Propagat.*, vol. 38, pp. 1039-1045, July 1990.

[4] J. J. Gulick and R. S. Elliott, "The design of linear and planar array of waveguide-fed longitudinal slots," *Electromagnetics*, vol. 10, pp. 327-347, Oct.-Dec. 1990.

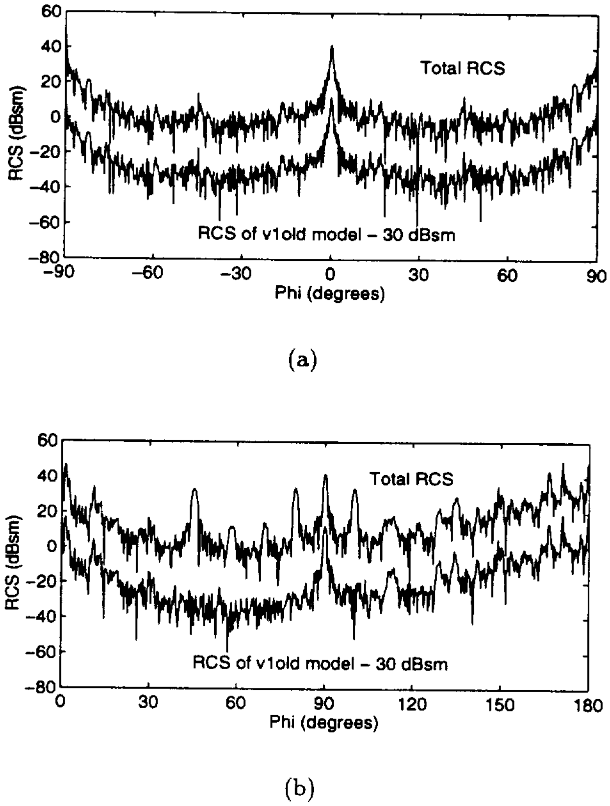

Figure 14: RCS of a v1old airplane model with the 42×42 circular slot array at $f = 9.9$ GHz. (a) E-plane; (b) H-plane.

[5] R. W. Lyon and A. J. Sangster, "Efficient moment method analysis of radiating slots in thick-walled rectangular waveguide," *IEE Proc.*, Pt. H, vol. 128, pp. 197-205, Aug. 1981.

[6] S. R. Rengarajan, "Compound radiating slots in a broad wall of a rectangular waveguide," *IEEE Trans. Antennas Propagat.*, vol. 37, pp. 1116-1123, Sept. 1989.

[7] K. Xia and Q.-J. Yang, "Study on characteristics of dielectric-covered waveguide slots," *Chinese J. Appl. Sci.*, vol. 7, no. 2, pp. 115-123, 1989.

[8] Q.-J. Yang and X. Tian, "Computer-aided-design of planar slot antennas," *Chinese J. Radio Sci.*, vol. 9, no. 1, pp. 1-11, 1994.

[9] J. Chen and J.-M. Jin, "Electromagnetic scattering from slot antennas on waveguides with arbitrary terminations," *Microwave Opt. Tech. Lett.*, vol. 10, no. 5, pp. 286-291, Dec. 1995.

[10] D. J. Andersh, M. Hazlett, S. W. Lee, D. D. Reeves, D. P. Sullivan, and Y. Chu, "XPATCH: A high-frequency electromagnetic-scattering prediction code and environment for complex three-dimensional objects," *IEEE Antennas Propagat. Magazine*, vol. 36, pp. 65-69, Feb. 1994.